AEROSOL FORMATION AND GROWTH IN COAL-FIRED POWER-PLANT PLUMES: LINKING PLUME-SCALE PROCESSES TO GLOBAL AEROSOLS AND CLIMATE

by

Robin Gerald Stevens

Submitted in partial fulfillment of the
requirements for the degree of
Doctor of Philosophy

at

Dalhousie University
Halifax, Nova Scotia
September 2014

© Copyright by Robin Gerald Stevens, 2014

Table of Contents

List of Tables

List of Figures

Abstract

New-particle formation in the plumes of coal-fired power plants and other anthropogenic sulphur sources may be an important source of particles in the atmosphere. These particles may grow to sizes where they can act as cloud condensation nuclei (CCN), and thereby increase cloud reflectivity and lifetime, resulting in a cooling of surface temperatures. It has been unclear how best to reproduce this plume-scale new-particle formation in global and regional aerosol models with grid-box lengths that are tens of kilometres and larger. The predictive power of these models has thus been limited by the resultant uncertainties in aerosol size distributions.

We have implemented online TwO-Moment Aerosol Sectional (TOMAS) microphysics into the System for Atmospheric Modelling (SAM), a Large-Eddy Simulation / Cloud-Resolving Model (LES/CRM). This model is evaluated against aircraft observations of new-particle formation in two different power-plant plumes and reproduces the major features of the observations. We show how the downwind plume aerosols can be greatly modified by both meteorological and background aerosol conditions.

Based on the results of the SAM-TOMAS model, we develop the Predicting Particles Produced in Power-Plant Plumes (P6) parameterization: a computationally-efficient, but physically-based, parameterization that predicts the characteristics of aerosol formed within sulphur-rich plumes based on large-scale mean meteorological parameters, emissions directly from the source, and mean background pollutant concentrations.

Finally, we implement the P6 parameterization in the GEOS-Chem-TOMAS global chemical-transport model in order to evaluate the contribution of coal-fired power plants globally to particle number and CCN concentrations. Globally, use of the P6 parameterization resulted in predicted CCN concentrations smaller than or similar to previous sub-grid sulphate schemes depending on the model configuration. We find that the sub-grid scale new-particle formation predicted by P6 is most sensitive to uncertainties in the model-predicted aerosol condensation sink. For constant SO_2 emissions, fewer new particles are formed in more polluted regions. This spatial heterogeneity in new-particle formation cannot be resolved by previous treatments of sub-grid sulphate but is captured by P6.

List of Abbreviations and Symbols Used

A	activation parameter
ACEnet	Atlantic Computational Excellence Network
$bgNO_x$	background NO_x concentration
$bgSO_2$	background SO_2 concentration
BLH	boundary-layer height
BRAVO	Big Bend Regional Aerosol and Visibility Study
CAC	Criteria Air Contaminants
CCN	cloud condensation nuclei
CCN(0.2%)	cloud condensation nuclei at 0.2% supersaturation
CDNC	cloud droplet number concentration
CL	chemiluminescence
CRM	cloud resolving model
CS	condensation sink
d	distance from pollution source
D_{m}	number median diameter
D_{mass}	mass median diameter
DMPS	Differential Mobility Particle Sizer
$DSWRF$	downward shortwave radiative flux
EDGAR	Emissions Database for Global Atmospheric Research
EMEP	Cooperative Programme for Monitoring and Evaluation of the Long-Range Transmission of Air Pollutants in Europe
E_{NOx}	emissions of NO_x
EPRI	Electric Power Research Institue
E_{SO2}	emissions of SO_2
f_{new}	fraction of H_2SO_4 that forms new particles
f_{ox}	fraction of emitted SO_2 oxidized to form H_2SO_4
GFEDv3	Global Fire Emissions Database version 3
H_2O	water
H_2SO_4	sulphuric acid

HONO	nitrous acid
J	nucleation rate
LES	large eddy simulation
LMB	Log-mean bias
m	slope of a log-linear regression
MEGAN	Model of Emissions of Gases and Aerosols from Nature
M_{H2SO4}	molar mass of H_2SO_4
M_{m}	mean mass per particle
M_{SO2}	molar mass of SO_2
NARR/OAR/ESRL PSD	North American Regional Reanalysis / Outstanding Accomplishments in Research / Earth System Research Laboratory Physical Sciences Division
NCEP	National Center for Environmental Prediction
NEI05	Environmental Protection Agency 2005 National Emissions Inventory
NH_3	ammonia
NH_4	ammonium
N_{new}	number of newly formed particles per mass of SO_2 emitted
NO	nitric oxide
NO_2	nitrogen dioxide
NOAA	National Oceanic and Atmospheric Administration
NO_{x}	nitrogen oxides (NO + NO_2 = NO_{x})
$NO_{\mathrm{x,eff}}$	effective NO_{x} concentration, see Eq. 3.1
NSERC	Natural Sciences and Engineering Research Council of Canada
NX	number concentration of particles larger than X nm
OH	hydroxyl radical
OH_{eff}	effective OH concentration, see Eq. 3.2-3.6
PM10	particulate mass smaller than 10 μm
R	correlation coefficient
rms	root-mean-square

S_0	solar constant at the top of the atmosphere = 1370 W m^{-2}
SAM	System for Atmospheric Modelling
SMPS	Scanning Mobility Particle Sizer
SO_2	sulphur dioxide
$SO_{2,\mathrm{eff}}$	effective SO_2 concentration, see Eq. 3.9
SO_3	sulphur trioxide
sza	solar zenith angle
T	assumed transmittance of the clear atmosphere = 0.76
TOMAS	TwO Moment Aerosol Sectional microphysics
UV	ultraviolet
v_g	mean boundary-layer wind speed
VOC	volatile organic compound
σ_g	geometric standard deviation

Acknowledgements

The list of those who have provided intellectual or moral support over the time it takes to complete a thesis cannot be confined to a single page. So please, do not think for a moment that any kindness by those I have neglected to mention was not appreciated.

Computational resources used for these studies were provided by ACEnet. This research was funded by NSERC and EPRI. We would like to thank Marat Khairoutdinov of the School of Marine and Atmospheric Sciences, Stony Brook University, for access to and help with SAM. NCEP NARR data was provided by the NOAA/OAR/ESRL PSD, Boulder, Colorado, USA, from their Web site at http://www.esrl.noaa.gov/psd/. I would also like to explicitly acknowledge the assistance and collaboration of all co-authors on the projects that comprise this thesis. A special thanks goes out to Dr. Chuck Brock, for providing and helping to interpret the observations used in Chapter 2 of this thesis.

My deepest thanks go to my supervisor, Dr. Jeff Pierce, for the mentorship, guidance, trust and friendship he has shown me over the years. I cannot imagine a better possible advisor. I'd also like to thank my committee members Dr. Glen Lesins, Dr. Ian Folkins and Dr. Randall Martin for their advice and helpful comments.

Thanks goes out as well to my office mates, the members of both the Pierce and Randall groups, for being sounding boards, founts of knowledge, technical support, and welcome distractions.

I'd like to thank my friends and family for their support, and for every time that they have listened to me talk about research. Most of all, I'd like to thank my wife, Charmaine. Because she's awesome. If I project any semblance of confidence or serenity, it is due to her unending love and encouragement.

Chapter 1

Introduction

1.1 Motivation

It has been established that aerosol particles, liquids or solids suspended in air, have a cooling effect on climate through the direct and indirect aerosol effects. The direct effect of aerosols on climate is the scattering of incoming solar radiation by the aerosol particles (Ångström, 1929). Sufficiently large aerosol particles (diameters larger than ∼30-100 nm) may act also cloud condensation nuclei (CCN), sites upon which water vapour can condense under atmospheric supersaturations to form stable cloud droplets. An increase in CCN concentrations tends to increase cloud droplet number concentrations (CDNC), and for constant liquid water content, an increase in CDNC results in smaller cloud droplets which more efficiently reflect solar radiation back to space (Twomey, 1974). In addition, the smaller cloud droplets are less efficient at producing precipitation, so clouds with higher CDNC tend to have longer lifetimes (Albrecht, 1989). These increases in cloud reflectivity and lifetime are termed the aerosol indirect effects on climate. The uncertainties in these aerosol effects on climate continue to be the largest contributor to uncertainties in the total anthropogenic forcing on climate (Boucher et al., 2013).

It is well-known that both the direct (Charlson et al., 1992) and indirect (Albrecht, 1989; Dusek et al., 2006; Twomey, 1974) effects strongly depend on the size of the particles involved. The size distribution of particles also determines, in part, the effects on human health of the particles. High aerosol concentrations cause human health problems, including respiratory and cardiovascular diseases, intensification of asthma, a reduction in physical abilities and an increase in mortality rates (Arya, 1999; Dockery et al., 1993; Peng et al., 2005; Stieb et al., 2002), and ultrafine particles (with diameters less than 0.1 μm in diameter) may have stronger effects than larger particles (Peters et al., 1997). In order to correctly predict the effects of aerosols

on both human health and climate, it is therefore necessary to accurately determine both the number and size of aerosol particles in the ambient atmosphere.

One of the largest anthropogenic sources of these aerosol particles are sulphur-rich emissions plumes (Dentener et al., 2006), such as those emitted by coal-fired power plants. Unfortunately, as we will discuss in the following sections, the plume-scale chemistry and physics that lead to new-particle formation are difficult to represent in the regional and global aerosol models used to study aerosol impacts on health and climate. Concentrations of gases and aerosols that affect new-particle formation and growth rates in non-linear ways are not homogeneous within these plumes, let alone across the typical scales of regional or global chemical-transport model grid boxes.

Regional and global models with online chemistry and physics have therefore made crude assumptions about the sub-grid processes within power-plant plumes that do not depend on the nature of the source or the ambient conditions. As we will discuss further in Sect. 1.3, these assumptions have been shown to have large effects on global aerosol number concentrations and CCN concentrations. In order to reduce the uncertainties due to the particles formed within plumes at sub-grid scale, and to thus reduce uncertainties in global aerosol size distributions used for health and climate studies, it is necessary to study the processes governing new-particle formation and growth within sulphur-rich plumes.

1.2 In-Plume Processes Affecting New-Particle Formation and Growth

Coal-fired power plants are major emitters of sulphur dioxide (SO_2) (Hegg et al., 1985; Hegg and Hobbs, 1980; Whitby, 1978). Concentrations of SO_2 in the plumes of these power plants are generally much higher than in a typical planetary boundary layer. When SO_2 is oxidized by the hydroxyl radical (OH) in the gas phase, it forms sulphuric acid (H_2SO_4), a low-volatility vapour. H_2SO_4 will condense onto pre-existing particles, and if its concentration is high enough, it will cluster with itself and other condensible gases to form new particles (i.e. aerosol nucleation) (Kulmala and Kerminen, 2008). Through new-particle formation in their plumes, coal-fired power plants and other anthropogenic sulphur sources have been shown to have a significant effect

on particle concentrations globally, particularly in the Northern Hemisphere (Adams and Seinfeld, 2003; Luo and Yu, 2011; Spracklen et al., 2005; Wang and Penner, 2009).

Several factors determine particle formation and growth rates in coal-fired power plant plumes. These include solar radiation and NO_x concentrations (through their influence on OH concentrations), and the pre-existing condensation and coagulation sinks (roughly proportional to aerosol surface area). Further complicating predictions of the formation and growth rates are that many of these factors vary spatially in the plume. Concentrations of OH in the plume control the SO_2 gas-phase oxidation rate and hence influence H_2SO_4 concentrations. These OH concentrations depend strongly on NO_x (nitric oxide (NO) + nitrogen dioxide (NO_2)) concentrations and sunlight (Olson et al., 2006), with increases in OH concentrations for increases in sunlight, but possible increases or decreases in OH concentrations for increasing NO_x, depending on ambient NO_x and volatile organic compound (VOC) concentrations. The primary loss mechanism for H_2SO_4 in the boundary layer is condensation onto existing aerosol particles (Eisele and Tanner, 1993), and so concentrations of H_2SO_4 also depend strongly on the aerosol condensation sink (approximately proportional to aerosol surface area). The variation in NO_x concentrations and the heterogeneity of the condensation sink within a given plume causes H_2SO_4 concentrations to vary dramatically within the plume. Nucleation and growth rates are strong functions of H_2SO_4 concentrations, and thus will vary spatially across the plume. Finally, the newly formed particles may be lost by coagulation with larger particles; as the size distribution evolves spatially in the plume, so will these coagulational losses. Currently, global- and regional-scale models typically have resolutions of hundreds and tens of kilometres or more, respectively, and are thus unable to accurately resolve the formation and growth of aerosols within these plumes using grid-box averages for chemical concentrations, aerosol concentrations, and meteorological values.

Additionally, recent pollution-control technologies installed on power plants reduce SO_2 and NO_x emissions. A reduction in SO_2 alone would result in a reduction of particles formed in power-plant plumes. However, as mentioned in the previous paragraph, concentrations of OH are sensitive to NO_x concentrations, which will vary

across a given plume. NO_x controls may either increase or decrease OH concentrations in the plume (depending on the environmental conditions) (Lonsdale et al., 2012). Thus, in many conditions a reduction in NO_x may lead to an increase in the formation rate of H_2SO_4 and perhaps an increase in particle formation and growth.

The sulphate particles that form in these plumes have previously been referred to as 'primary sulphate' in the literature. However, this source of particles should not be confused with a direct emission of ash or other particles from the stacks of power-plants, which is currently uncommon in North America and Europe due to the adoption of efficient pollution controls. As these particles form in the plumes of high-sulphur sources at scales smaller than the typical grid resolution of regional and global models, we adopt the term sub-grid sulphate to describe this source of sulphate mass.

1.3 Previous Studies of Sub-Grid Sulphate

As stated in the previous section, regional and global models with online aerosol chemistry and physics currently have grid box resolutions too coarse to resolve new-particle formation and growth within sulphur-rich plumes. They have thus made crude assumptions about sub-grid new-particle formation and growth within power-plant plumes that do not depend on the nature of the source or the ambient conditions. These models typically assume that some fraction of all anthropogenic SO_2 emissions are oxidized to form sulphate at the sub-grid scale. This sub-grid sulphate is added to the model via a fixed, pre-assumed size distribution for all anthropogenic sulphate sources under all atmospheric conditions. For example, the study of Makkonen et al. (2009) used the assumption recommended by the AeroCom emissions inventory Dentener et al. (2006) that specifies that all aerosol formation in anthropogenic SO_2 source plumes results in new particles having a single accumulation lognormal mode with median diameter 1 μm and a standard deviation of 2.0. Other studies (Adams and Seinfeld, 2002, 2003; Pierce and Adams, 2006, 2009; Pierce et al., 2007; Spracklen et al., 2005; Wang and Penner, 2009) have assumed the aerosol formed in sub-grid plumes to have a bi-modal lognormal distribution: they emit a fraction of the particles as a nucleation mode with number mean diameter 10 nm and standard

deviation 1.6, and they emit the rest as an Aitken mode with geometric number mean diameter 70 nm standard deviation 2.0. The fraction of sulphate mass emitted into the nucleation mode is also set as 5% or 15% depending on the study. Yu and Luo (2009) use yet another assumption. They emit 5% of the sulphate mass into the nucleation mode described above, and condense the remaining mass onto the existing accumulation mode particles. As some of the sulphate formed in the plume must condense onto the pre-existing particles that have been entrained into the plume, this approach is, in this way, more realistic than the other assumptions.

While the studies listed above differ in the amount and size of sub-grid sulphate particles, they all assume that these values are constant regardless of the meteorological and chemical characteristics of the emissions plumes. However, several studies have shown that the particle formation in plumes is strongly sensitive to environmental conditions. Yu (2010b) showed that differences in temperature and hydroxyl concentrations cause the size and number of aerosol particles to vary seasonally and diurnally. Lonsdale et al. (2012) showed that the number of particles formed within sulphur-rich plumes is strongly dependent on the emission rates of both SO_2 and NO_x from the source. As we show in Chapter 2, the amount and size of sub-grid sulphate strongly depends on sunlight and the pre-existing aerosol condensation sink. However, there had been no means of representing these dependencies of plume-scale particle formation in global and regional models.

Many studies have tested the sensitivity of CCN concentrations to these assumptions. First we describe the results of studies that emitted sub-grid sulphate according to the 10 and 70 nm bi-modal lognormal distribution described above. Adams and Seinfeld (2003) and Spracklen et al. (2005) found that if the fraction of anthropogenic SO_2 emitted as sub-grid sulphate was changed from 0% to 3%, cloud condensation nuclei concentrations at a supersaturation of 0.2%, hereafter denoted as CCN(0.2%), in polluted areas would double. This was believed to be an upper limit for this effect, as both models included only sulphate and sea-salt aerosol. However, the study of Wang and Penner (2009) which included organic matter, black carbon, and dust, varied the fraction of SO_2 emitted as sub-grid sulphate over a smaller range (0% to 2%),

and also found that CCN(0.2%) would more than double over polluted areas. They also found that CCN(0.2%) would increase by 23% to 53% averaged over the global boundary layer and the first aerosol indirect effect radiative forcing would increase by 11% to 31% (depending on the nucleation scheme used for regional-scale nucleation in the boundary layer). The study of Luo and Yu (2011) tested sensitivities to the sub-grid sulphate assumptions used by Yu and Luo (2009). They found that varying the fraction of sulphur effectively emitted as particles from 0% to 5% would increase CCN(0.2%) concentrations globally by 11% in the boundary layer. Additionally, they found that varying the fraction of sulphate emitted into the nucleation mode from 5% to 15% would increase CCN(0.2%) by as much as 18% over source regions.

Lee et al. (2013) recently quantified the uncertainty in CCN concentrations that was due to 28 different uncertain inputs in the GLOMAP global aerosol model. Based on the results of Stevens et al. (2012) (Chapter 2 of this thesis), the range of possible values used in Lee et al. (2013) for the diameter of sub-grid sulphate particles was reduced to a smaller range than the full range of sub-grid sulphate assumptions used before, which led to a reduced uncertainty range in CCN concentrations due to uncertainties in sub-grid sulphate compared to the range of estimates described in the previous paragraph. Even with the reduced ranges, they found the uncertainties in sub-grid sulphate production to be just as important as the uncertainties in SO_2 emission rates, and had the largest contribution of the 28 inputs to the uncertainty in CCN concentrations over polluted North America and Europe. The global uncertainty in sub-grid sulphate particle size ranked as the twelfth largest contributor to the relative uncertainties in CCN concentrations of the 28 inputs tested, with a global-mean relative uncertainty range (from -2 to +2 standard deviations in CCN concentrations) of about 16%. These large uncertainties in CCN prediction due to sub-grid sulphate formation highlight the need for improved representation of plume-scale particle formation in global and regional models.

1.4 Outline of the Thesis

The thesis contains three connected studies. First, to better understand the number and size of particles that should be effectively emitted from anthropogenic sources

in regional and global models, we explored the evolution of the number and size of sulphate aerosol particles inside coal-fired power-plant plumes using a 3-D fluid-dynamics model of plume chemistry and physics: the System for Atmospheric Modelling (Khairoutdinov and Randall, 2003) with TwO Moment Aerosol Sectional (Adams and Seinfeld, 2002) microphysics (SAM-TOMAS). This model uses a sub-km resolution to resolve the variation of chemistry and physics within the plumes. We test the ability of the model to predict the median diameter and number of particles nucleated within the plumes of two different power plants under different meteorological conditions. We test the sensitivity of the model output to different possible ambient meteorological conditions and background aerosol conditions and show that the resultant size distribution of sulphate aerosol is strongly dependent on these conditions. This work comprises Chapter 2 of the thesis.

In order to to capture the variability that exists in the amount and size of aerosol formed within sulphur-rich plumes, we develop in Chapter 3 the Predicting Particle Production in Power-Plant Plumes (P6) parameterization: a computationally efficient (the increase in running time for a 3-D aerosol model would be negligible because the parameterization consists only of several arithmetic equations), but physically based, parameterization that predicts the characteristics of aerosol formed within sulphur-rich plumes based on parameters commonly available in global- and regional-scale models. This parameterization is based on the results of the SAM-TOMAS model characterized and tested against observations in Chapter 2. Given large-scale mean meteorological parameters ((1) wind speed, v_g [m s^{-1}], (2) boundary-layer height, BLH [m], and (3) downward shortwave radiative flux, $DSWRF$ [W m^{-2}]), (4) emissions of SO_2, E_{SO2} [kg s^{-1}], and (5) NO_x, E_{NOx} [kg N s^{-1}], from the source; (6) mean background condensation sink, CS [s^{-1}]; (7) mean background SO_2, $bgSO_2$ [ppb], and (8) NO_x, $bgNO_x$ [ppb], concentrations; and (9) the desired distance from the source, d [m]; the P6 parameterization predicts (1) the fraction of the emitted SO_2 that is oxidized to form H_2SO_4, f_{ox}; (2) the fraction of that H_2SO_4 that forms new particles instead of condensing onto pre-existing particles, f_{new}; (3) the mean mass per particle of the newly formed particles, M_m [kg]; and (4) the number of newly formed particles per mass of SO_2 emitted, N_{new} [# (kg SO_2)$^{-1}$].

In Chapter 4, we implement the P6 sub-grid sulphate parameterization into a global chemical-transport model with online aerosol microphysics. We test the sensitivities of predicted N3, N10, N40, N80 concentrations to assumptions about sub-grid sulphate. As the output of the P6 parameterization is expected to be sensitive to pre-existing aerosol due to sub-grid coagulation, we investigate the sensitivity of predictions to the global amount of secondary organic aerosol and grid-resolved nucleation scheme. We also investigate the sensitivity of N80 enhancement to sub-grid sulphate to greater emissions of SO_2 and NO_x to better understand the effects of pollution controls on CCN concentrations.

Chapter 2

Nucleation and Growth of Sulphate Aerosol in Coal-Fired Power Plant Plumes: Sensitivity to Background Aerosol and Meteorology

Stevens, R. G., Pierce, J. R., Brock, C. A., Reed, M. K., Crawford, J. H., Holloway, J. S., Ryerson, T. B., Huey, L. G. and Nowak, J. B.: Nucleation and growth of sulphate aerosol in coal-fired power plant plumes: sensitivity to background aerosol and meteorology, Atmos. Chem. Phys., 12(1), 189-206, doi:10.5194/acp-12-189-2012, 2012.

2.1 Introduction

To better understand the number and size of particles that should be effectively emitted from anthropogenic sources in regional and global models, we explore the evolution of the number and size of sulphate aerosol particles inside coal-fired power-plant plumes using a 3-D fluid-dynamics model of plume chemistry and physics: the System for Atmospheric Modelling (Khairoutdinov and Randall, 2003) with TwO Moment Aerosol Sectional (Adams and Seinfeld, 2002) microphysics (SAM-TOMAS). This model uses a sub-km resolution to resolve the variation of chemistry and physics within the plumes. We test the ability of the model to predict the median diameter and number of particles nucleated within the plumes of two different power plants under different meteorological conditions. We test the sensitivity of the model output to different possible ambient meteorological conditions and background aerosol conditions and show that the resultant size distribution of sulphate aerosol is strongly dependent on these conditions.

The goal of this paper is to test the ability of the SAM-TOMAS model to predict new-particle formation and growth in anthropogenic sulphur plumes, determine the

number and size of particles formed, and test the sensitivity of the predicted particles to various parameters. Section 2.2 presents a description of the SAM-TOMAS model. In Sect. 2.3 we describe the case studies used to evaluate the model, present the results of these evaluations, and assess the performance of the model. Section 2.4 explores the sensitivity of our modelled results to the nucleation parameterization used, to the background aerosol, and to high and low VOC conditions. Our discussion and conclusions are presented in Sect. 2.5.

2.2 Description of Model

In order to study nucleation and growth in anthropogenic sulphur plumes, we have developed a model that incorporates TwO Moment Aerosol Sectional (TOMAS) (Adams and Seinfeld, 2002) microphysics into the System for Atmospheric Modelling (SAM) (Khairoutdinov and Randall, 2003), a Large-Eddy Simulation / Cloud-Resolving Model (LES/CRM). (An LES model is a fluid dynamics model in which motion at the scales larger than the model grid and smaller than the model domain is resolved, but sub-grid scales are parameterized. A CRM is a model capable of resolving an ensemble of clouds at time scales longer than the life cycle of an individual cloud.) SAM is a flexible fluid dynamics model with a domain that can span tens or hundreds of kilometres, and the individual grid cells can have dimensions between tens of metres to several kilometres. A full description is available in Khairoutdinov and Randall (2003).

The TOMAS microphysics algorithm simulates the aerosol size distribution using fifteen size bins spanning dry diameters of 3 nm to 10 μm. In each size bin, TOMAS tracks the number of particles as well as sulphate, ammonium, and water mass. No organic aerosols are included in the model at this time under the assumption that sulphate aerosol formation will be the primary aerosol formation mechanism in the plume; however, we will discuss the uncertainties in this assumption later. TOMAS explicitly calculates coagulation, condensation and nucleation (Adams and Seinfeld, 2002; Pierce and Adams, 2009). Aerosol growth and coagulational loss below 3 nm is approximated by the parameterization of Kerminen and Kulmala (2002). This

scheme predicts the instantaneous formation for 3 nm particles based on the nucleation rates (of clusters with diameters closer to 1 nm), local growth rates and condensation sinks. Because the growth rates and condensation sinks within the plume may change on timescales faster than the growth time from 1 to 3 nm, the Kerminen and Kulmala (2002) scheme introduces additional uncertainties to our simulations. However, these uncertainties are generally much smaller than the relative uncertainties between the nucleation schemes themselves. Several nucleation schemes are tested and are described in the following paragraph. We simulate gaseous SO_2, NO_x, ammonia (NH_3) and H_2SO_4. We do not explicitly simulate volatile organic compounds (VOCs); however, we test the sensitivity of our results to the effect of high and low VOC concentrations on OH concentrations (described below). We assume that there are no primary particles emitted directly from the stack, which is consistent with the airborne measurements we use for model evaluation.

We have implemented several different nucleation schemes for use in the model: (1) the classical binary homogeneous nucleation scheme described by Vehkamäki et al. (2002), (2) the ternary H_2O-H_2SO_4-NH_3 nucleation schemes described by Merikanto et al. (2007) and (3) Napari et al. (2002) scaled by a factor of 10^{-4} (Westervelt et al., 2013), (4) activation-type nucleation as described by Kulmala et al. (2006), and (5) the ion-mediated nucleation scheme of Yu (2010a). The resulting size distributions predicted by the Merikanto and scaled Napari schemes did not differ significantly, so we only present the results of the Merikanto scheme in this work. In activation-type nucleation, the rate varies as a linear function of the sulphuric acid concentration, according to the following equation (Kulmala et al., 2006):

$$J = A \cdot [H_2SO_4] \tag{2.1}$$

Where J is the nucleation rate, and A is an activation parameter. Unless we specify otherwise (e.g. during the sensitivity analysis), we use A=10^{-7} s^{-1} (Sihto et al., 2006).

We use a parameterization to estimate the concentration of OH in each model grid box based on the concentration of NO_x in ppbv and the downward shortwave radiative flux ($DSWRF$) in W m^{-2}. While the NO_x concentration is used to predict the concentration of OH, we do not currently have a chemical sink for NO_x in the model,

which will lead to an over-prediction of NO_x later in the plume. The parameterization is an empirical fit to the results of many simulations from the detailed time-dependent photochemical box model described by Olson et al. (2006). These simulations span conditions observed below 1 km over the eastern United States as sampled from the NASA DC-8 during the Intercontinental Chemical Transport Experiment-North America (INTEX-A) field campaign (Singh et al., 2006).

One process not accounted for in the OH parameterization is the effect of the presence of large amounts of highly reactive VOCs on OH production. The additional peroxy radicals from isoprene oxidation induce a shift in the peak OH production to a higher NO_x level. To understand the potential effect of high VOC concentrations in our study, a second parameterization, referred to as the high-VOC case, was developed based on an isoprene mixing ratio of 1.5 ppbv (the 95th percentile value observed during INTEX-A). We refer to the original parameterization as the low-VOC case. The two parameterizations are outlined in detail in appendix A.

Dry deposition is not included in the simulations presented here. We tested the sensitivity of the modelled aerosol size distributions to dry deposition by implementing a simple dry deposition scheme. However, even for high deposition velocities, dry deposition had a trivial influence on the size and concentration of particles for the spatial scales we are simulating.

The model meteorology is driven by nudging and boundary conditions from assimilated meteorology from the National Center for Environmental Prediction (NCEP) North American Regional Reanalysis (NARR) data (Mesinger et al., 2006). The reanalysis data were provided by the National Oceanic and Atmospheric Administration (NOAA) / Outstanding Accomplishments in Research (OAR) / Earth System Research Laboratory (ESRL) Physical Sciences Division (PSD), Boulder, Colorado, USA, from their website at `http://www.esrl.noaa.gov/psd/`. NCEP NARR three-hourly assimilation data used in our studies included surface pressure, zonal and meridional wind speed profiles, potential temperature profile, water vapour mixing ratio profile, downward shortwave radiative flux (for OH calculation), surface sensible

heat flux, surface latent heat flux, and surface momentum fluxes. The modelled vertical profiles of temperature, water vapour mixing ratio and horizontal wind speed are nudged to the assimilation profiles on a one-hour time scale. The surface fluxes are prescribed as model boundary conditions. The model turbulent motions (on spatial scales both larger than and smaller than grid box sizes) are freely predicted by SAM and not provided by the NCEP NARR data set.

We obtained the emissions of SO_2 and NO_x from each power plant from Clean Air Markets emissions inventory (United States Environmental Protection Agency, 2012). Background concentrations of SO_2 and NO_x, as well as the background size distribution of aerosol, were determined from the in-flight measurements either upwind of the power plant or outside of the power-plant plume. In the Parish case (the power plant cases are described in the next paragraph), background values of NH_3 were also measured. No measurements of NH_3 were available for the Conesville case.

In order to determine the accuracy of our model, we have evaluated the model with airborne data obtained in the plumes of two coal-fired power plants: the W. A. Parish power generation facility near Houston, TX, obtained during the Texas Air Quality Study (TexAQS) 2006 field campaign (Parrish et al., 2009), and the Conesville power generation facility near Conesville, OH during the International Consortium for Atmospheric Research on Transport and Transformation (ICARTT) campaign (Brown et al., 2007). The observations were taken on board the NOAA WP-3D aircraft. These measured species and the instrumentation used are summarized in Table 2.1.

The model grid contains 128 grid-boxes in the downwind direction, 60 in the cross-wind direction, and 50 in the vertical direction. We ran the model using 400 m by 400 m horizontal resolution, and 800 m by 800 m horizontal resolution (we will compare the results of the two resolutions). The vertical resolution was always 40 m. Thus the total domain dimensions were 51.2 km x 24 km x 2 km for the 400x400x40m grid-box cases, and 102.4 km x 48 km x 2 km for the 800x800x40m grid-box cases.

Table 2.1: Measurements and instrumentation for each investigated power plant.

	Parish	Conesville
NO	O_3-induced CL[1]	O_3-induced CL
NO_2	UV[2] photolysis-CL	UV photolysis-CL
SO_2	Pulsed UV fluorescence	Pulsed UV fluorescence
NH_3	Protonated acetone dimer CIMS[3]	Not available
H_2SO_4	NO_3^- CIMS	NO_3^- CIMS
Aerosol number, size and volume distributions	White and laser light scattering and five CPC[4]s in parallel behind a low turbulence inlet	Laser light scattering and five CPCs in parallel behind a low turbulence inlet

[1]CL - chemiluminescence, [2]UV - ultraviolet,
[3]CIMS - chemical ionization mass spectrometry, [4]CPC - condensation particle counter

2.3 Case Studies

2.3.1 Parish

The Parish power generation facility is located ∼40 km southwest of downtown Houston, Texas. The area further south and west of the facility is used for farmland. Five units of the Parish power generation facility were active on September 27th, 2006. One of these units had wet lime flue gas desulphurization SO_2 controls. Four of the units (including the unit with desulphurization) controlled NO_x through selective catalytic reduction, and the remaining unit used overfire air for NO_x controls. Particulate matter was controlled for all units through the use of baghouse filters.

Atmospheric conditions were sunny and clear. The boundary layer was initially stable, becoming unstable between 18:00 GMT and 21:00 GMT (12:00 and 15:00 local time), with a depth of 500 m growing to 1000 m. The wind was blowing from the south at ∼5 m/s. The aerosol background was typical of a remote continental region, with three lognormal modes: a small nucleation mode with concentration 1.2 cm^{-3}, median diameter 3.3 nm, and geometric standard deviation 1.3; a wide Aitken mode with concentration 770 cm^{-3}, median diameter 89 nm, and geometric standard deviation 2.8; and an accumulation mode with concentration 640 cm^{-3}, median diameter 120 nm, and geometric standard deviation 1.3.

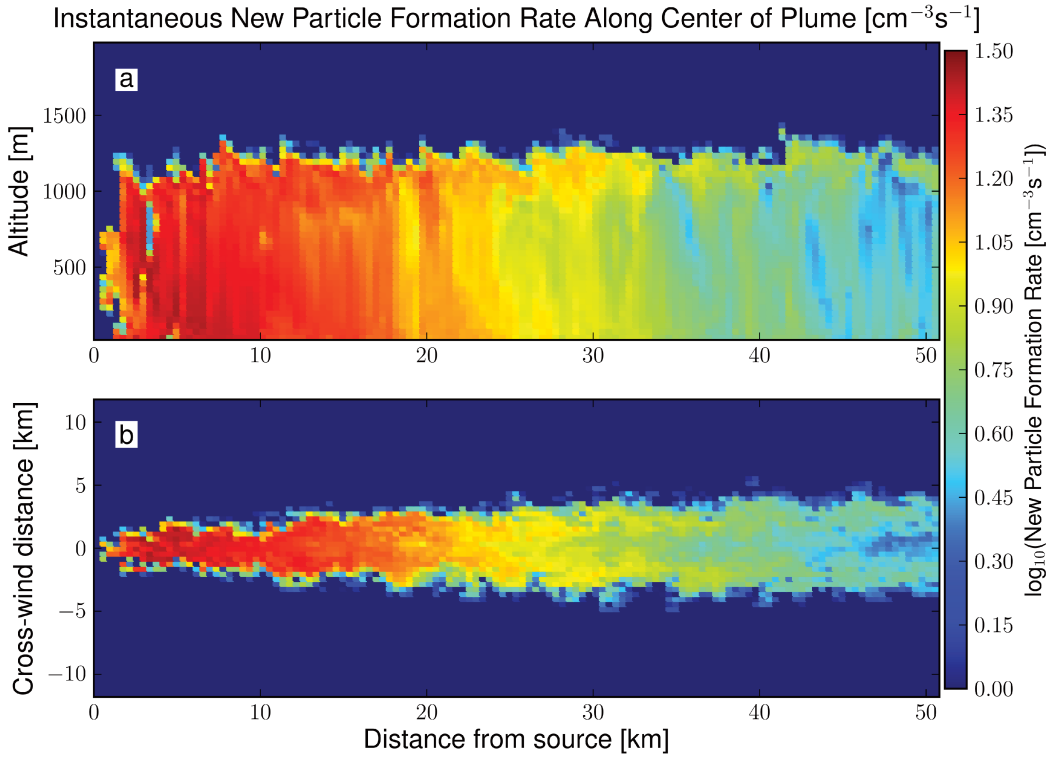

Figure 2.1: Instantaneous snapshot of new-particle formation rates of the modelled Parish plume (a) along the cross-wind center and (b) at an altitude of 460 m. Model resolution is 400x400x40m.

We show the predicted instantaneous nucleation rates as a function of height and distance from the source along the center of the plume in Fig. 2.1a, and as a function of cross-wind distance and distance from the source at an altitude of 460 m in Fig. 2.1b. This figure can be considered a 'snapshot' of the nucleation rates within the modelled plume at a single point in time. (All other figures in this work present the concentrations of aerosol or gas species time-averaged over a period of ∼2.2 hours.) In the first 1-2 kilometres, nucleation is suppressed because OH concentrations are very low due to high NO_x concentrations. As the initial high NO_x concentrations become diluted, nucleation rates reach a maximum around 5 km from the source. Nucleation rates decrease further downwind of the source as the condensation sink increases and SO_2 concentrations decrease (primarily due to dilution), but are elevated where the polluted boundary-layer air mixes with the clean air of the free troposphere due to the reduced condensation sink in this region. In general, we see enhanced nucleation

where high concentrations of H_2SO_4 formed within the plume and the lower condensation sink and NO_x outside of the plume coincide due to turbulent mixing. These turbulent eddies create regions within the plume with especially high and low concentrations of NO_x and SO_2 that alter the nucleation rate within the plume. This in turn causes the contribution of nucleation to the condensation sink to be inhomogeneous within the plume. As seen in Fig. 2.1, these turbulent mixing effects can cause the nucleation rate to vary by a factor of two within the plume, even at the same distance from the source. These inhomogeneous regions of enhanced nucleation, evident at the downwind plume edges, cannot be resolved using a model that assumes a predefined Gaussian plume, which has motivated the choice of an LES/CRM model that represents turbulent motion for this study.

Figure 2.2 compares observed and modelled gas and particle concentrations for an aircraft transect through the plume ∼36 km from the power plant. Panel (a) shows the measured and modelled gas concentrations as the aircraft flew across the plume, and panels (b) and (c) show the observed and modelled size distributions, respectively. We see that the width of the modelled plume agrees with the width of the observed plume, but the predicted concentration of NO_x is too large at the center of the plume by ∼4 ppb. Our predicted concentrations of H_2SO_4 and SO_2 agree with the observed concentrations, within their respective variabilities. We note that there is a peak in the observed NO_x concentrations ∼2 km from the plume center, and that this peak coincides with the location of a major multilane highway, the Sam Houston Tollway. We therefore believe that this peak is due to vehicle emissions, which are not explicitly simulated within the model. The model slightly under-predicts the peak diameter of the aerosol size distribution as ∼30 nm, compared to the observed peak diameter of ∼50 nm. The number concentration of aerosol at the peak within the plume is very close to the observed value, but the number concentration of particles smaller than 100 nm outside of the plume is under-predicted. We do not explicitly simulate any other sources of particles or gases within the model domain aside from the power plant, and this may explain the discrepancy outside of the plume.

We show the observed and modelled trace-gas concentrations with distance from

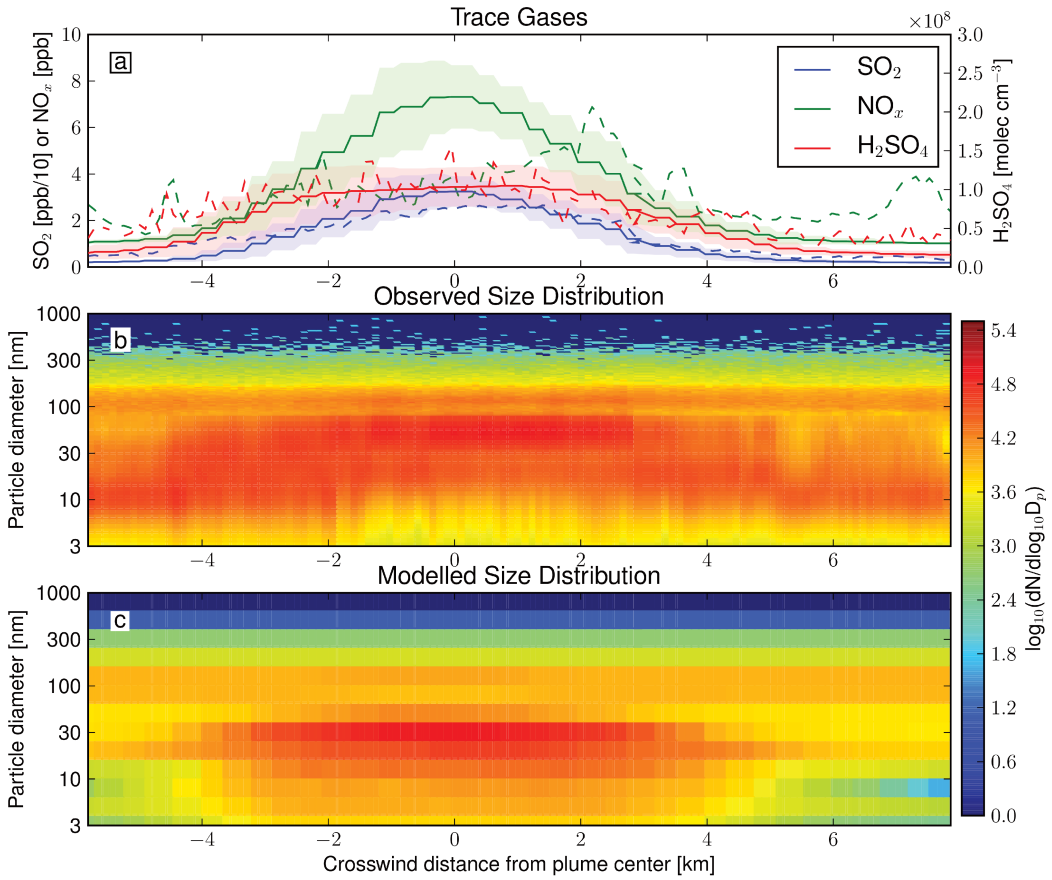

Figure 2.2: Trace gas and aerosol concentrations along the second transect north of Parish, about 36 km from the power-plant. X-axes show flight track through crosswind slice of plume. Model resolution is 400x400x40m. (a) Trace gas concentrations. Observed concentrations as dashed lines, model results as solid lines. Shaded area indicates one standard deviation of the model results, due to turbulent fluctuations. (b) Observed aerosol number size distribution. (c) Modelled aerosol number size distribution.

the power plant, averaged over the plume cross section, in Fig. 2.3a. We consider a point along a transect to be within the plume if the concentration of SO_2 at that point is greater than 33% of the maximum concentration of SO_2 found along that transect, after subtracting out the background concentration. NO_x measurements were unavailable inside the plume for the fourth transect, so no observed value for NO_x is plotted for this transect. The results from the model using 800x800x40m resolution are shown as a solid line, and the 400x400x40m resolution results are shown as a dashed line. We note that the 800x800x40m mixing ratios of NO_x and SO_2 are $\sim$1 ppbv and $\sim$5 ppbv lower than the 400x400x40m mixing ratios, respectively, but

the H_2SO_4 concentrations are quite similar between the two cases. Differences in these values between the two resolutions are similar when applied to the Conesville case (not shown). When the SO_2 and NO_x are initially emitted into the model domain, they are immediately diluted to be uniformly mixed within a single grid-box. Concentrations of SO_2 and NO_x are consequently slightly lower in the 800x800x40m than in the 400x400x40m resolution model. These variations in the concentrations of gaseous species due to altering the model resolution between 400x400x40m and 800x800x40m are similar in magnitude to variations due to across-plume turbulence, and it does not appear that the accuracy of the model will be greatly improved by using resolutions finer than 800x800x40m. In the following discussion, we will consider the results of the 800x800x40m resolution model, as this allows for comparison with the observations further than 50 km from the source.

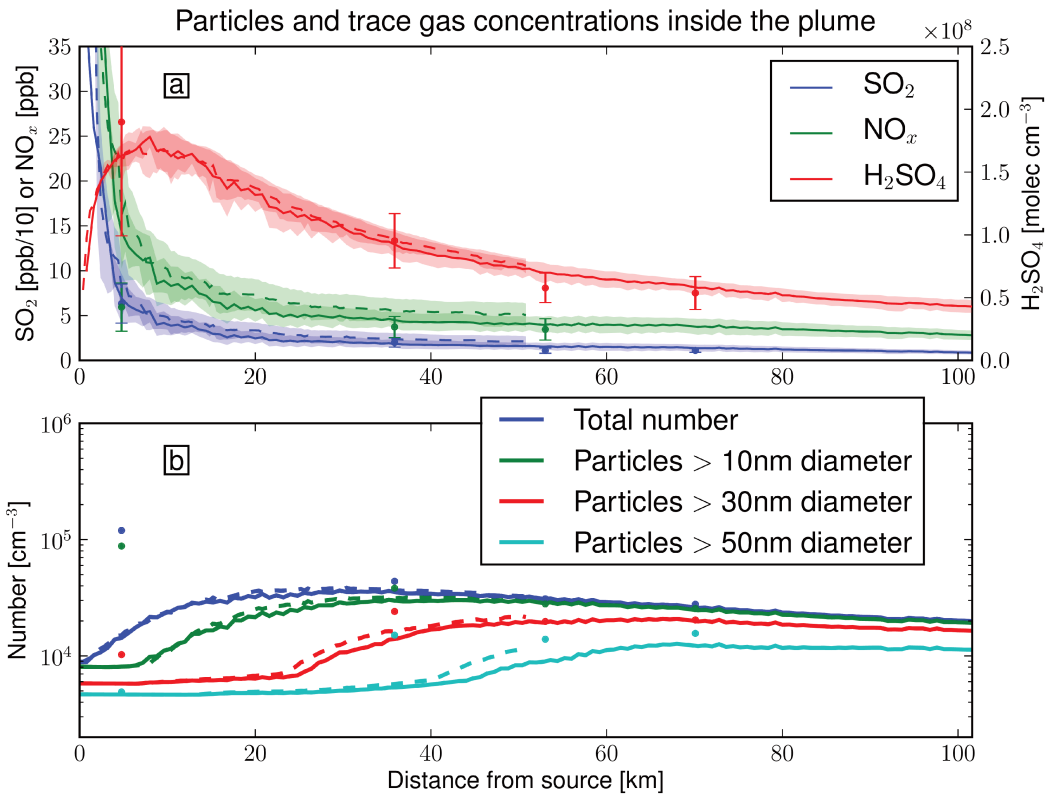

Figure 2.3: (a) Trace gases and (b) particle number vs. distance downwind from the Parish power-plant, averaged over the plume. Dots are aircraft observations; lines are model results. Shaded area and error bars indicate one standard deviation in concentration across plume width. Solid lines indicate 800x800x40m model resolution; dashed lines indicate 400x400x40m model resolution.

At the first transect, ∼5.4 km downwind from the power plant, we overestimate the concentrations of NO_x by ∼10 ppb, but we accurately predict the concentrations of SO_2 and H_2SO_4. At the remaining transects, ∼36, ∼54, ∼71, and ∼94 km from the source, the predicted concentrations of NO_x are within 1 ppb of the observed values, and we continue to accurately predict SO_2 and H_2SO_4.

We show the observed and modelled number concentrations with distance from the power plant in Fig. 2.3b. The particles in the 400x400x40m resolution simulation grow slightly faster than those in 800x800x40m resolution simulation, but we note that the disagreement between the results for each model resolution is less than a factor of 1.5 for any given size range at all downwind distances. We will show in Sect. 2.4 that the uncertainties in aerosol concentrations due to the choice of nucleation parameterization or due to uncertainties in the effects of VOCs upon OH concentrations are comparable or larger in magnitude, and thus we feel that the accuracy of the model results will not be improved by the choice of a finer model resolution until the level of scientific understanding of these processes has advanced. At the first transect, ∼5.4 km from the source, the nucleated aerosol particles have not yet grown beyond 50 nm in either the model or the observations, and so the numbers of particles with diameters larger than 50 nm predicted by the model and observed differ by less than 5%. However, the observed particles have grown larger than 30 nm, while the modelled particles have only grown to ∼10 nm. The total number of nucleated particles is also almost an order of magnitude smaller in the model than in the observations. At ∼35 km downwind of the source the model under-predicts the number of particles in each size range. The model under-predicts the number of particles with diameters larger than 50 nm because the newly formed particles in the model have only grown to a diameter of ∼30 nm, whereas some of the observed particles have already grown larger than 50 nm. The model under-estimates concentrations of particles smaller than 50 nm in diameter by less than a factor of 2. The modelled concentrations of particles smaller than 50 nm are within 10% of the observed concentrations at the remaining transects, and the modelled concentrations of particles larger than 50 nm in diameter are 36% and 22% lower than the observed values at the third and fourth transects, respectively. These results show that for the Parish case, the SAM-TOMAS

model does a decent job of predicting the particle size distributions for distances from the source that are relevant for effective emissions in regional and global models.

The discrepancies between the model results and the observations for the first two transects may be explained by nucleation occurring very close to or within the power plant stack. Due to the high NO_x concentrations near the stack, the predicted OH concentrations are low in this region and SO_2 oxidation is initially predicted to be slow; thus the model does not predict a high initial nucleation rate. We suggest two possible ways by which sufficiently high concentrations of H_2SO_4 for nucleation and particle growth may be forming within or close to the stack: First, there may be formation of sulphur trioxide (SO_3) in the power plant, which would quickly form H_2SO_4 in the stack (the nucleation might be occurring in the stack or shortly thereafter) (Mueller and Imhoff, 1994; Srivastava et al., 2004; Cichanowicz, 2007; Zaveri et al., 2010). Secondly, nitrous acid (HONO) that is emitted from the stack would be a source of OH near the stack, and thus increase the oxidation of SO_2 to form H_2SO_4 in the region of our predicted OH minima (Kleffmann, 2007). While direct emission of HONO would provide a brief burst of OH, evidence for sustained HONO production through heterogeneous chemistry has also been observed in polluted environments such as Houston, TX (Olaguer et al., 2009) and Mexico City (Li et al., 2010; Volkamer et al., 2010). Although this chemistry is not well understood and is often related to organic aerosols, it could be relevant to power-plant plumes where high surface area is available to drive HONO formation providing additional OH and accelerating SO_2 oxidation.

A useful value for global and regional models is the number of particles formed per mass of SO_2 emitted. These values may be used as sub-grid nucleation or effective primary sulphate emissions in these models. We approximate this value in the model by subtracting the original background concentrations from the particle number concentration, and then we divide this by the background-corrected SO_2 mass concentrations and integrate across the plume. These values are shown as a function of downwind distance in Fig. 2.4. At distances greater than 60 km downwind of the source, the values stabilize near an additional $2{\cdot}10^{17}$ total particles per kg SO_2, of

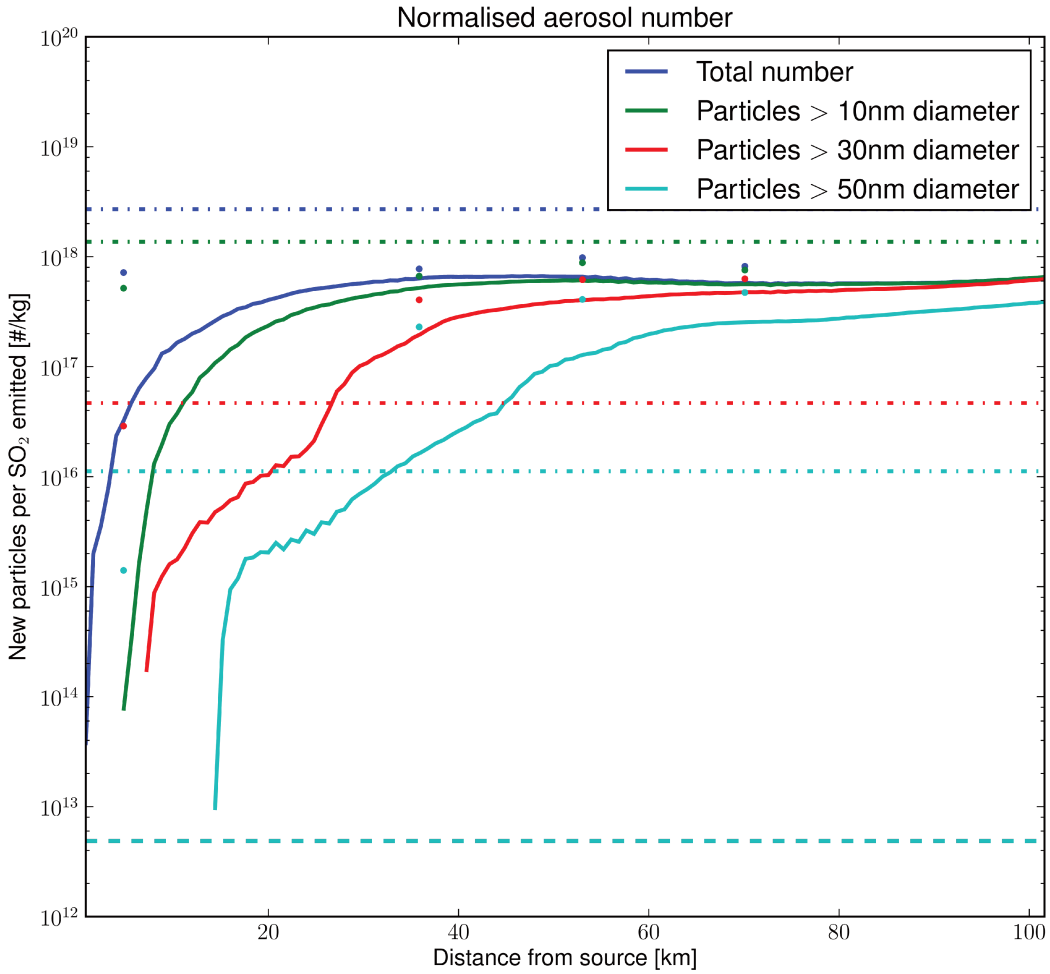

Figure 2.4: Additional predicted particles per kg SO_2 versus distance from the Parish power plant, summed over the plume. Model resolution is 800x800x40m. Dots indicate aircraft observations, solid lines indicate model results, dashed lines indicate the values used by Dentener et al. (2006), and dashed-dotted lines indicate the values used by Adams and Seinfeld (2003). Coloring indicates size range of particles. Essentially all particles in the Dentener et al. (2006) distribution are larger than 50 nm, so all dashed lines overlap one another.

which half are larger than 50 nm. Nearly all of the particles have grown larger than 30 nm.

For comparison, we also plot number of particles per kg SO_2 that would result from the primary sulphate size distributions used in the AeroCom data set (Dentener et al., 2006) and in Adams and Seinfeld (2003). We note that the stable values reached by our model are several orders of magnitude greater than the value from (Dentener

et al., 2006). This is because the model predicts that most new particles nucleated within the plume will grow to sizes less than 50 nm, while Dentener et al. (2006) select a median diameter of 1 μm, yielding a much smaller number of much larger particles. The stable value for total particles reached by the model is less than a third of that from Adams and Seinfeld (2003), but we predict an order of magnitude more particles larger than 30 nm and almost two orders of magnitude more particles larger than 50 nm. This indicates that Adams and Seinfeld (2003) use a size distribution that includes a much larger fraction of particle number at sizes smaller than 30 nm than our model predicts for the specific case of the Parish power plant.

Table 2.2: Fraction of SO_2 oxidized and fraction of produced H_2SO_4 that condenses onto new particles rather than pre-existing particles within 50 km for each model simulation. The labels 400x400x40m and 800x800x40m refer to the two model resolutions used in this study. The A-6, Vehk, Meri, and Yu10 nucleation schemes are discussed in Sect. 2.4.1. The REM, MAR, and URB aerosol backgrounds are discussed in Sect. 2.4.2. The sunny and cloudy cases and the high-VOC and low-VOC cases are discussed in Sect. 2.4.3.

	Fraction of SO_2 oxidized	Fraction of produced H_2SO_4 that condenses onto new particles rather than pre-existing particles
Parish base case (400x400x40m, REM-sunny, A-7, high-VOC)	9%	21%
Parish (800x800x40m)	11%	18%
Parish A-6	9%	33%
Parish Vehk	9%	<<1%
Parish Meri	9%	42%
Parish Yu10	9%	13%
Parish REM-cloudy	0.8%	<<1%
Parish MAR-sunny	9%	90%
Parish MAR-cloudy	0.8%	75%
Parish URB-sunny	9%	<<1%
Parish URB-cloudy	0.8%	<<1%
Parish low-VOC	6%	9%
Conesville (400x400x40m)	4%	13%
Conesville (800x800x40m)	4%	12%

As noted in Sect. 2.1, regional and global models commonly assume that a constant fraction of SO_2 emitted from the power plant will oxidize to form H_2SO_4 and that a constant fraction of this H_2SO_4 condenses to new particles rather than pre-existing

particles. In Table 2.2, we show the fraction of the emitted SO_2 that has oxidized to form H_2SO_4 within 50 km of the source for each case and the fraction of the sulphate formed that has gone into the nucleation or growth of new particles within 50 km of the source for each case. For the base Parish case, we find that 9% of the emitted SO_2 is converted into sulphate within 50 km of the source, climbing to 26% within 100 km. We note that these numbers are greater than the fraction of SO_2 that is emitted as sub-grid sulphate from power plants in global models, which is generally 5% or less (Adams and Seinfeld, 2003; Spracklen et al., 2005; Wang and Penner, 2009; Luo and Yu, 2011), and that the horizontal resolution in such models would generally be 100s of km. However, this Parish case is a sunny summer daytime case, which should favour the highest amount of sub-grid oxidation, whereas the global models chose a representative average value. Furthermore, the emitted SO_2 in global models that is not oxidized immediately will continue to oxidize in subsequent time steps, so this low bias on sunny days may be partially corrected for in the global models. Our model also predicts that 21% of the sulphate mass will form or condense onto new particles within 50 km from the source. This is at the upper range of assumptions used for the fraction of sulphate mass that condenses onto new particles in global models (Luo and Yu, 2011). However, both the fraction of SO_2 that oxidizes and the fraction of sulphate mass that forms new particles are dependent on the conditions of each power-plant case. We will explore the effects of changing some of these conditions in Sect. 2.4.

2.3.2 Conesville

The Conesville power generation facility is located in a valley along the Muskingham river in Ohio, in a heavily forested region in the North-Eastern United States. Of the four units in operation on August 6th, 2004, two had wet lime flue gas desulphurization SO_2 controls and low NO_x burner technology with separated overfire air, and one had only low NO_x burner technology (dry bottom only). All units had electrostatic precipitators.

During the time of the measurement there was an unstable boundary layer that was ~1300 m deep and was capped by broken clouds. The wind was from the north

at ∼5 m/s. The aerosol background was typical of a rural continental area with an Aitken peak with $dN/dlog_{10}D_p$ ∼$2{\cdot}10^4$ cm^{-3} at 20 nm and $dN/dlog_{10}D_p$ ∼$5{\cdot}10^3$ cm^{-3} at particle diameters away from this peak up to 200 nm. Above 200 nm the aerosol concentrations decreased. The total number concentration was $1.7{\cdot}10^4$ cm^{-3}. The average background mixing ratios of SO_2 and NO_x measured were ∼0.6 ppbv and ∼1.6 ppbv, respectively.

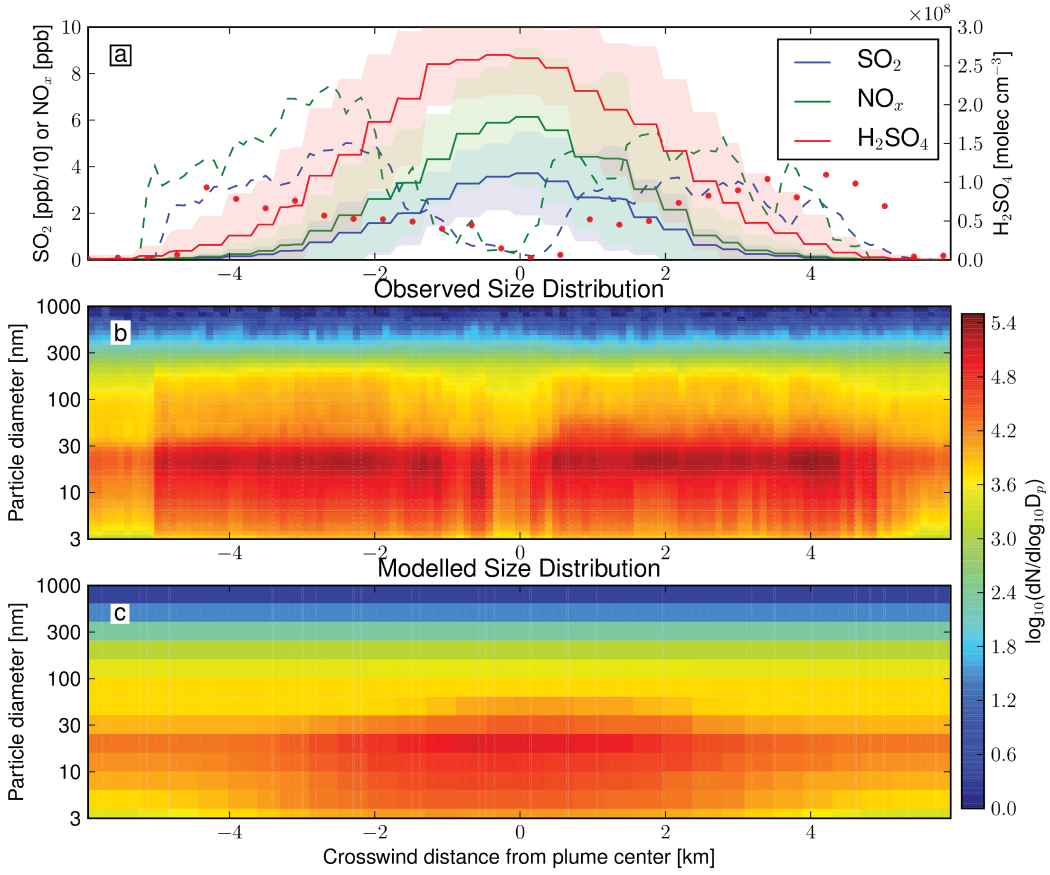

Figure 2.5: Trace gas and aerosol concentrations along the first transect south of Conesville, about 24 km from the power-plant. X-axes show flight track through cross-wind slice of plume. Model resolution is 400x400x40m. (a) Trace gas concentrations. Observed concentrations as dashed lines (SO_2 and NO_x) and dots (H_2SO_4), model results as a solid line. Shaded area indicates one standard deviation of the model results, due to turbulent fluctuations. (b) Observed aerosol number size distribution. (c) Modeled aerosol number size distribution.

The measurements and model predictions of gas-phase SO_2, NO_x, and H_2SO_4

along the first transect, ∼24 km from the source, are shown in Fig. 2.5a. The modelled values are shown as solid lines, and the measured concentrations of NO_x and SO_2 are shown as dashed lines. The measured values of H_2SO_4 are shown as dots in this figure in order to indicate the lower time resolution of those measurements. The observations show two separate plumes along this transect, which cannot be predicted by the current version of the model. The two plumes are also visible in the observed size distribution, shown in Fig. 2.5b. The SO_2-NO_x ratios for the two plumes are similar, and neither plume was observed upwind of the power plant, which leads us to believe that both plumes originate from the Conesville power plant. Since the power-plant stacks are much closer than the distance between the center of the plumes (∼3 km), the plume must have bifurcated either due to complex flows at the stack (Fanaki, 1975) or due to topographic effects from hills in the region. The boundary layer at the Conesville power generation facility was very stable until sunrise, ∼5 hours before the observations were made, which may favour bifurcation of the plume at the stack. We note that the plume width and the mixing ratios of NO_x and SO_2 predicted by the model do agree well with those observed in either of the two plumes, although the model predictions of H_2SO_4 were about double those of the measurements. If both plumes are due to the Conesville power plant, then it would seem that roughly half the mass of SO_2 and NO_x are missing from the model predictions. This may be due to an inaccuracy in the emissions that we use in the model or an incorrect prediction of the boundary-layer height in the model. If the predicted boundary-layer height was too large, the actual emissions from the power plant would be vertically diluted to a greater extent in the model, which would yield lower mixing ratios along the transect. Integrating the mixing ratios of NO_x and SO_2 across the second and third (farther) transects yields much smaller discrepancies than those observed at the first transect. The separation of the two plumes is less distinct at the second transect, ∼40 km from the source, in both the trace gas observations and the aerosol size distribution (not shown). Under unstable conditions, vertical shear in wind direction and turbulent diffusion is likely to mix two adjacent plumes together.

The modelled number distribution for the first transect south of Conesville is shown in Fig. 2.5c. The peak at ∼20 nm matches the peak in the observed number

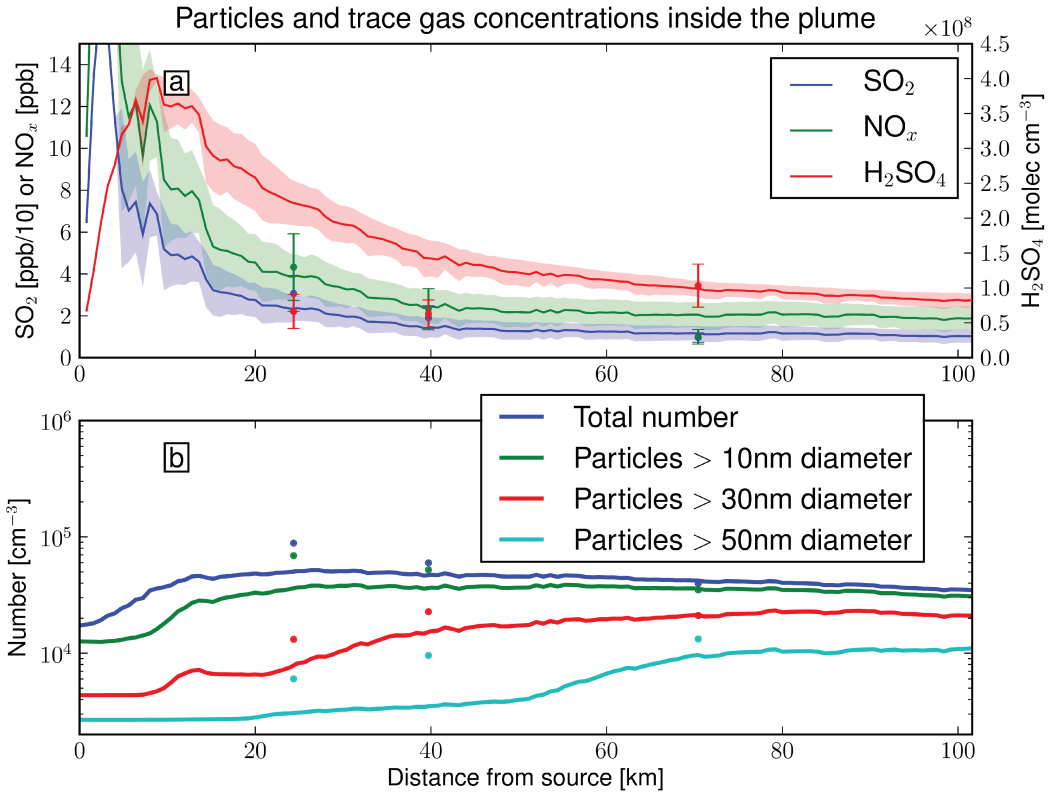

Figure 2.6: (a) Trace gases and (b) particle number versus distance downwind from the Conesville power-plant, averaged over the plume. Dots are aircraft observations; lines are model results. Shaded area and error bars indicate one standard deviation in concentration across plume width. Model resolution is 800x800x40m.

distribution. However, there is an observed increase within the plume in the number of particles with diameters between 40 nm and 200 nm that is not predicted by the model. In Fig. 2.6b, we show the total number concentration, and the number concentration of particles larger than 10, 30, and 50 nm in diameter. The unpredicted increase in 40 nm to 200 nm particles is responsible for the under-prediction of particles larger than 30 and 50 nm at the first and second transects. By the third transect, a significant fraction of the particles from the initial nucleation burst have grown larger than 30 nm, and as these particles from the nucleation burst now dominate the number concentration in this size range, the model predictions are within 1% of the observed number concentration of particles larger than 30 nm. As in the Parish case, the model predictions for number concentrations of all but the largest particles agree well (within 10%) with the observations beyond 50 km from the power plant, although the concentrations of particles larger than 50 nm are under-predicted

by 27%.

The concentrations of trace gases with distance from the power plant are shown in Fig. 2.6a. The concentrations of SO_2 and NO_x for the first two transects are well predicted by the model. At the third transect, ∼68 km from the source, the observed plume is much wider and more dilute than the modelled plume, and as a consequence, the model over-predicts the NO_x concentrations within the plume. We see the opposite trend in H_2SO_4 concentrations: the model over-predicted the concentrations of H_2SO_4 for the first two transects, but the observed concentration of H_2SO_4 increases at the third transect, and the modelled concentration agrees well with this observed value. An over-prediction of H_2SO_4 would yield larger nucleation and growth rates of aerosol particles, and thus should increase particle number concentrations. However, as discussed above, the predicted particle number concentrations at the first two transects are less than those observed in each size range. There are several possible explanations for these seemingly contradictory features. During the measurement campaign, there were broken clouds present, which would make the penetration of UV radiation into the boundary layer highly variable in space and time. Consequently, OH production rates, and thus H_2SO_4 production rates would be highly variable in space and time. It is possible that at the time of measurement of the first two transects, cloudy conditions had lowered the OH production rate, and the H_2SO_4 concentration had been depleted below the mean concentration at those locations. We will discuss further the effects of cloudy conditions upon sulphate production in Sect. 2.4.3. It is also possible that the effect of the over-prediction of H_2SO_4 upon aerosol concentrations has been compensated by an under-prediction of the nucleation rate. We will show in Sect. 2.4.1 that the predicted aerosol number concentrations could increase if a different nucleation parameterization was used.

Figure 2.7 shows that the predicted change in the number of particles per additional mass of SO_2 stabilizes at distances greater than 70 km from the power plant at an additional $6{\cdot}10^{17}$ total particles per kg SO_2. Almost all of these particles have grown to diameters larger than 30 nm by this distance, and half are larger than 50 nm. However, as the model predicts fewer particles larger than 50 nm than are observed,

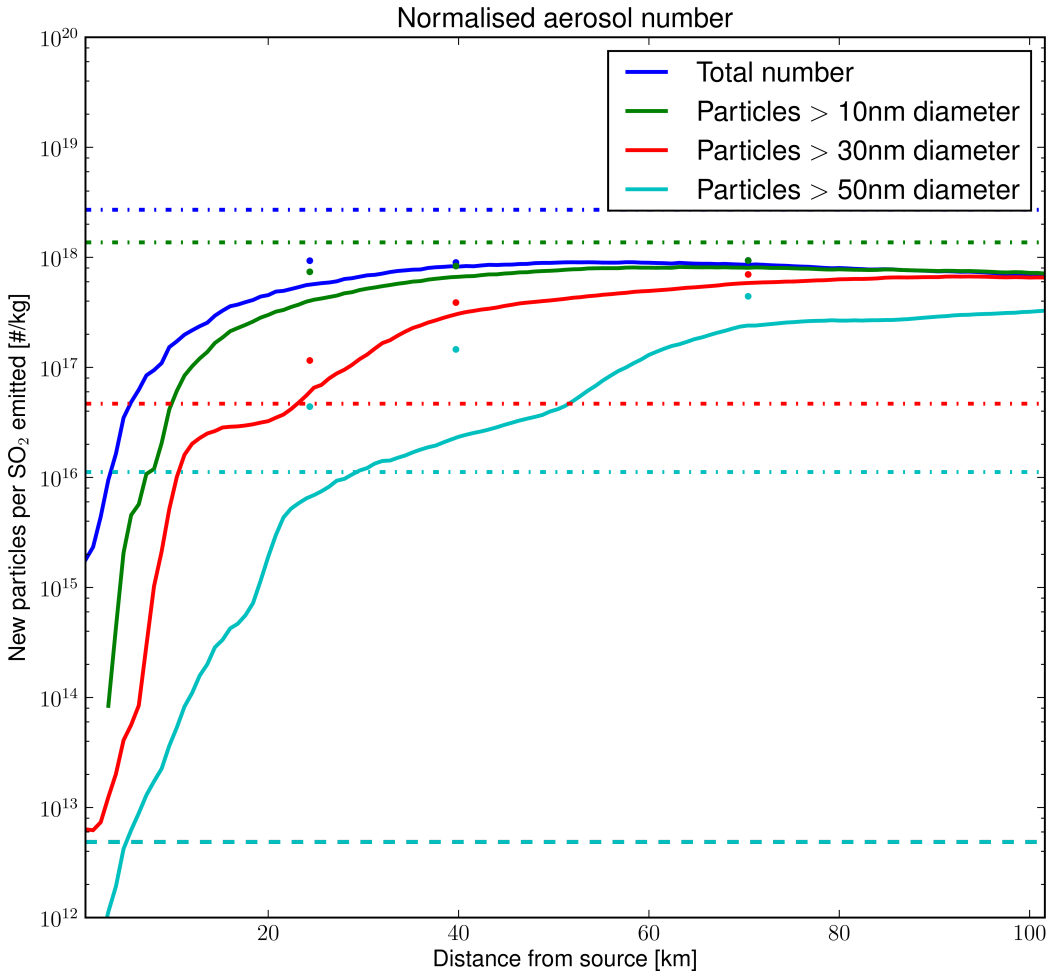

Figure 2.7: Additional predicted particles per kg SO_2 emitted versus distance from the Conesville power-plant, summed over the plume. See Sect. 2.3.1 for a description of the calculation. Model resolution is 800x800x40m. Dots indicate aircraft observations, solid lines indicate model results, dashed lines indicate the values used by Dentener et al. (2006), and dashed-dotted lines indicate the values used by Adams and Seinfeld (2003). Coloring indicates size range of particles. Essentially all particles in the Dentener et al. (2006) distribution are larger than 50 nm, so these lines overlap.

it also predicts fewer additional particles larger than 50 nm per kg SO_2 than are observed. These results are remarkably similar to those obtained for the Parish case. As total SO_2 emissions were much higher in the Conesville case than in the Parish case, the predicted concentrations of H_2SO_4 were ~2 times larger than in the Parish case even though a smaller fraction of the emitted SO_2 formed H_2SO_4 (this is due to a lower shortwave radiative flux) (Table 2.2). This, along with a lower condensation sink than in the Parish case, resulted in faster new-particle formation, and more than

twice as many new particles being formed in the Conesville case. Thus the number of particles per kg SO_2 was similar between cases. Both observations and models indicate several orders of magnitude more particles per kg SO_2 in the Conesville case than suggested by Dentener et al. (2006), and less than one third of the particles per kg of SO_2 emitted suggested by Adams and Seinfeld (2003).

The fraction of produced sulphuric acid that formed or condensed onto new particles (as opposed to condensing onto pre-existing particles) was somewhat less in the Conesville case (13%) than that in the Parish case (21%) (Table 2.2). While more particles form in the Conesville case, more of the particles in the Parish case grow beyond 50 nm, and the largest of the newly formed particles constitute a disproportionately large fraction of the condensation sink. Thus the ratio of the condensation sink of the new particles to the pre-existing particles is less in the Conesville case, and this in turn causes less of the H_2SO_4 to condense onto the new particles in the Conesville case than in the Parish case.

2.4 Sensitivity Studies

In this section, we will explore how uncertainties in model inputs as well as variability in atmospheric conditions affect the predicted nucleation and growth in the Parish plume.

2.4.1 Nucleation parameterization

The mechanisms of aerosol nucleation in the atmosphere are still very uncertain, and different schemes may predict very different nucleation rates under the same conditions. In Fig. 2.8, we show the effect of different nucleation parameterizations upon the modelled additional particles per kg SO_2 emitted for the Parish power plant. We show the additional total particles per kg SO_2 emitted in Fig. 2.8a and the additional particles larger than 30 nm per kg SO_2 in Fig. 2.8b. The classical binary nucleation scheme described by Vehkamäki et al. (2002) (Vehk, red line) does not predict any nucleation in this case because, like other classical binary nucleation schemes, it does not predict nucleation in warm lower-tropospheric conditions. Therefore, there are no additional particles beyond the background concentration. There are, however,

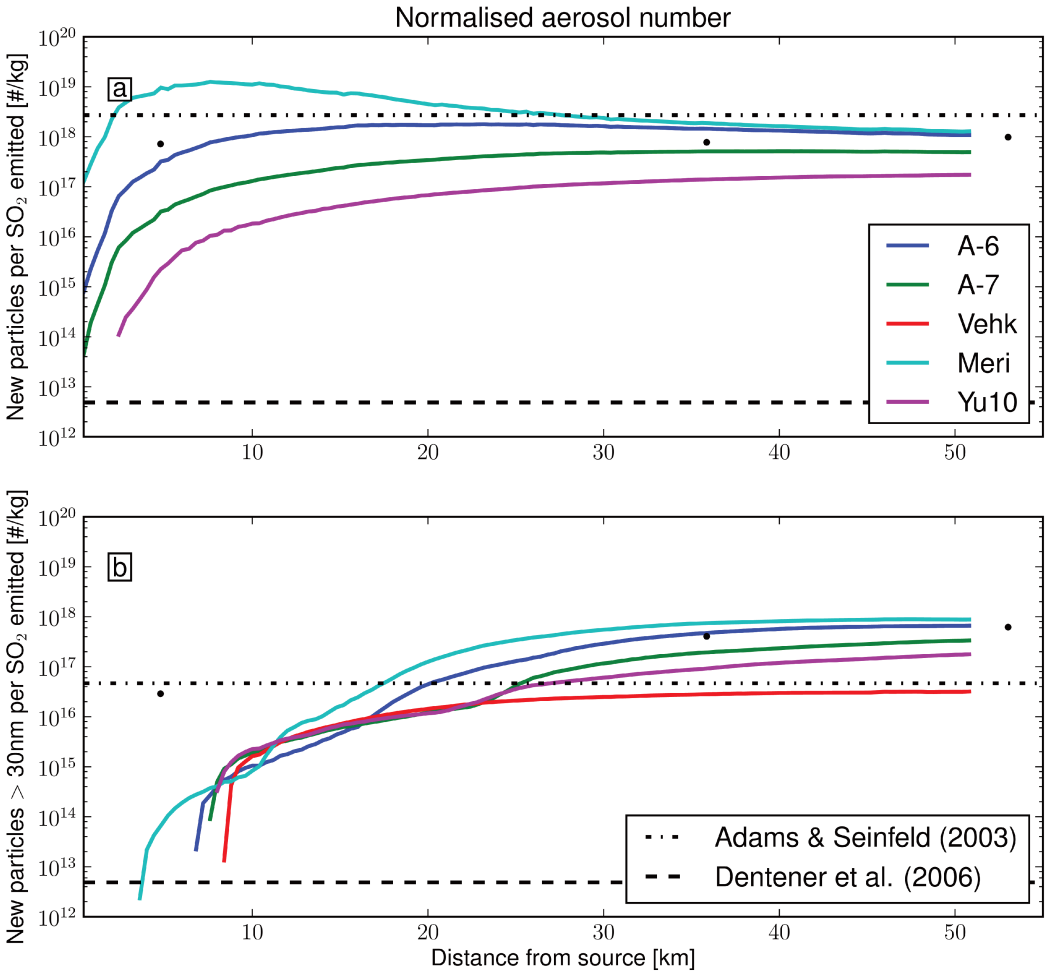

Figure 2.8: (a) Total additional predicted particles and (b) additional particles larger than 30 nm per kg SO_2 versus distance from the Parish power-plant, using several nucleation schemes. See Sect. 2.3.1 for a description of the calculation. Values are averaged over the plume. Model resolution is 400x400x40m. Black dots indicate aircraft observations, solid colored lines indicate model results, black dashed lines indicate the values used by Dentener et al. (2006), and black dashed-dotted lines indicate the values used by Adams and Seinfeld (2003).

additional particles larger than 30 nm for the Vehk case because of condensational growth of pre-existing particles smaller than 30 nm that were mixed into the plume. This causes the concentration of particles larger than 30 nm to increase above the original background concentration; however, these are an artifact of our calculation and should not truly be considered newly formed particles. The nucleation scheme from Merikanto et al. (2007) (Meri, cyan line) predicts too much nucleation in this case. The Meri case has a large number of particles close to the source that decreases

away from the source due to coagulation. The nucleation rate predicted by activation-type nucleation is sensitive to the fitting parameter A (equation 2.1). However, for values of A (A=10^{-7} s^{-1}: denoted by A-7, green line, and A=10^{-6} s^{-1}: denoted by A-6, blue line) that typically describe nucleation in continental boundary-layer conditions (Spracklen et al., 2008; Sihto et al., 2006), the median diameter of the nucleated particles and the total number of particles agree within a factor of 2 with the observations described here, excepting the first transect. We have no measurements of the rate of ion-pair production for any of our cases, and therefore we have tested the ion-mediated nucleation scheme described by Yu (2010a) while prescribing 5, 10, and 15 ion pairs cm^{-3} s^{-1}, which we believe to be a reasonable range (Harrison and Carslaw, 2003). We found that the resultant size distribution differed, but not greatly over this range. The 10 ion pairs cm^{-1} s^{-1} case is shown in Fig. 2.8 as Yu10, the purple line. The Yu scheme somewhat under-predicts the number of new particles for the Parish case.

When excluding the Vehk case that did not predict any nucleation, the choice of nucleation scheme results in an uncertainty of about one order of magnitude in the total number particles 40 km downwind and onward. There is a slightly smaller uncertainty in the number of particles larger than 30 nm at 30 km downwind and onward. This highlights the importance of the nucleation scheme in predicting nucleation in the plumes. The activation nucleation scheme with an A-factor of 10^{-7} s^{-1} generally performed the best against observations for the Parish and Conesville cases and thus it was used throughout the case studies presented earlier. This shows that for these two case studies, the nucleation in the plume had a similar dependence on sulphuric acid as has been observed in both continental field observations and lab studies (Sipilä et al., 2010). However, given that the conditions are very different in the plume nucleation cases relative to regional-scale nucleation events, we stress that this similarity in sulphuric-acid dependence does not imply that the nucleation mechanisms are necessarily the same.

There is also an uncertainty of more than a factor of 3 in the fraction of produced sulphate that condenses onto the new particles rather than pre-existing particles

(Table 2.2). However, only the Yu10 case predicted fractions within the range tested by Luo and Yu (2011). We note that the values chosen by Luo and Yu (2011) were intended to apply to all point sources of SO_2 globally under all atmospheric conditions, and that the fraction of sulphate in new particles in this particular case may far exceed that of an average case for reasons independent of the nucleation mechanism (e.g. large amounts of solar radiation and moderate amounts of pre-existing aerosol).

2.4.2 Background aerosol

In order to test the sensitivity of the model to the pre-existing aerosol size distribution, we performed additional model simulations of the Parish case with background aerosol typical of a clean marine environment (MAR), and with background aerosol typical of a polluted urban environment (URB). (The original simulations are abbreviated REM for remote continental.) We described the pre-existing background aerosol using three lognormal modes, with the number concentrations, median diameters, and geometric standard deviations as listed in Seinfeld and Pandis (2006), and reproduced in Table 2.3 of this work. The model resolution was 400x400x40m, and activation-type nucleation with an activation constant of A=10^{-7} s^{-1} was used for these simulations.

The resultant additional particles per kg SO_2 emitted are shown in Fig. 2.9 (sunny cases, the cloudy cases will be described later). The MAR-sunny case has larger increases in particle number than the base case (REM-sunny) throughout the life of the plume. The low concentration of background aerosol in the MAR-sunny case implies a low condensation sink, and hence more nucleation, but nucleation-mode self-coagulation tends to dampen this increase in number. The low background condensation sink also leads to only a small fraction of the H_2SO_4 condensing onto the existing particles, and 90% condenses onto the new particles (Table 2.2). The newly formed particles grow to larger sizes than in the base REM-sunny case, reaching 40 nm at 36 km from the source, at which point the particles in the base case had only reached 30 nm.

When the model is run with an urban background (URB-sunny), particle number

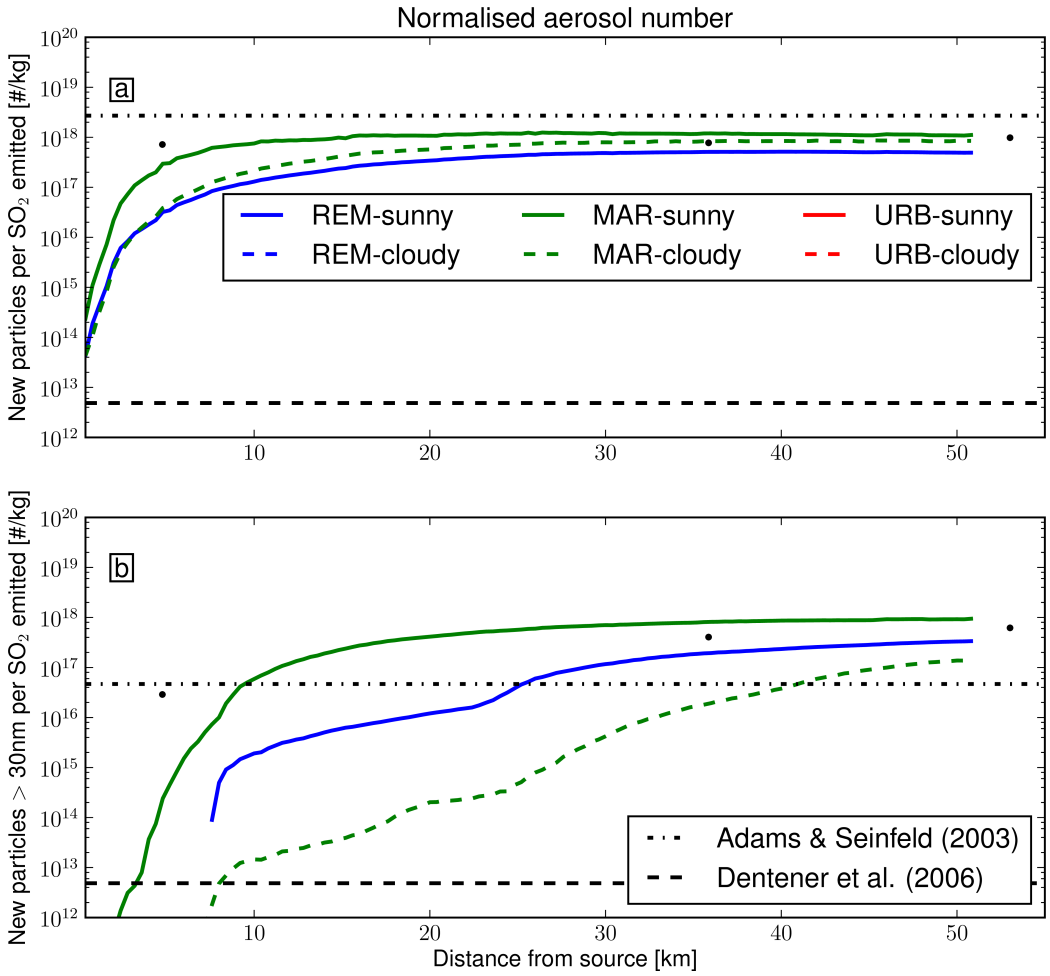

Figure 2.9: (a) Total additional predicted particles and (b) additional particles larger than 30 nm per kg SO_2 versus distance from the Parish power-plant, for different background aerosol size distributions and differing rates of OH production. See Sect. 2.3.1 for a description of the calculation. Values are averaged over the plume. Model resolution is 400x400x40m. Black dots indicate aircraft observations, solid colored lines indicate model results, black dashed lines indicate the values used by Dentener et al. (2006), and black dashed-dotted lines indicate the values used by Adams and Seinfeld (2003). Particle numbers decreased for the REM-cloudy, URB-sunny, and URB-cloudy cases, so these lines are not visible.

concentrations actually decrease below their initial values, and therefore the line for the urban background case is not visible in Fig. 2.9. The polluted background provides a large condensation sink, and nearly all the H_2SO_4 that is formed condenses onto these particles. There is thus a low concentration of H_2SO_4 in the plume and a low nucleation rate. The large number of small particles in the urban background also yield fast coagulation rates both inside and outside of the plume. The increase

in particle number due to nucleation within the plume (which is much lower than in the REM-sunny and MAR-sunny cases) is therefore less than the decrease in particle number due to coagulation.

These results show that the number of new particles formed in plumes depends greatly on the pre-existing aerosols. Next-generation parameterizations of plume subgrid particle formation must account for the amount of pre-existing aerosol.

2.4.3 Concentration of OH

As discussed in Sect. 2.2, we use a parameterization to predict the concentration of OH based on the downward shortwave radiative flux and the concentration of NO_x in the model. To test the sensitivity of the model to changes in radiation, we have performed model simulations with the downward shortwave radiative flux scaled to one third of its value in the base Parish case. In these cases, we simulate the effect of cloudy overcast conditions upon OH production. These results are also shown in Fig. 2.9 (compare the cloudy cases to the sunny cases for each background aerosol concentration). H_2SO_4 production is suppressed under these cloudy conditions (0.8% of the SO_2 has oxidized at 50 km compared to 9% for the sunny cases, Table 2.2), and therefore new-particle formation and growth is also suppressed. Regardless of the aerosol background, there are fewer particles formed within the plume. For the base case remote-continental aerosol background (REM-cloudy), very little nucleation occurs under these cloudy conditions, and the nucleated particles do not grow beyond 6 nm. Like the URB-sunny case described above, more particles are lost to coagulation than are formed by nucleation, and thus the line for the REM-cloudy case is not visible in Fig. 2.9. The URB-cloudy case is also not visible for the same reason. Under clean marine aerosol background conditions (MAR-cloudy), similar numbers of particles form, but the particles grow more slowly and do not reach the same size as in the MAR-sunny case. In the MAR-cloudy case the particles grow beyond 30 nm in diameter further downwind of the plume's source and a smaller fraction of the particles grow larger than 30 nm in diameter. These results show that we would expect very little particle formation and growth at night in the plumes except for cases where SO_3 is emitted from the plant (e.g. Zaveri et al., 2010).

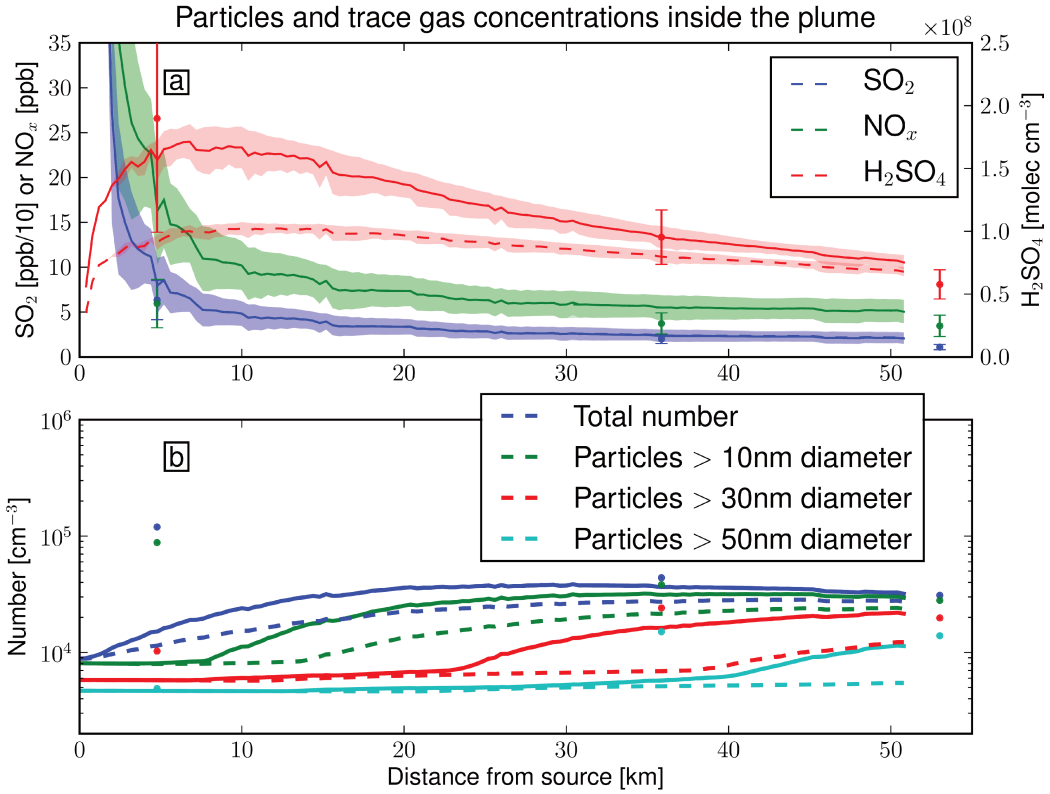

Figure 2.10: (a) Trace gases and (b) particle number vs. distance downwind from the Parish power plant averaged over the plume for differing rates of OH production due to different assumptions of VOC concentrations. Dots are aircraft observations; lines are model results. Shaded area and error bars indicate one standard deviation in concentration across plume width. The results of the high-VOC case are shown as a solid line, and the results of the low-VOC case are shown as a dashed line. Model resolution is 400x400x40m.

We do not yet explicitly account for the effect of VOCs upon OH concentrations within the model. In order to determine the sensitivity of our results to this uncertainty, we ran our model under low-VOC conditions (as described in Sect. 2.2). The concentrations of trace gases and particle number concentrations are shown in Fig. 2.10. For a constant shortwave radiation flux, maximum steady-state concentrations of OH occur at a NO_x concentration that depends on the concentrations of VOCs. Under high-VOC conditions, this NO_x concentration that yields the maximum concentration of OH will be larger than under low-VOC conditions. The parameterization we use to estimate concentrations of OH yields a maximum concentration of OH for NO_x mixing ratios of 1.2 ppbv under low-VOC conditions, and 2.0 ppbv under

high-VOC conditions. Since the area inside the plume has very high mixing ratios of NO_x, larger than 5 ppbv in the Parish case (even far from the source), the mixing ratios of NO_x will be closer to those that yield the maximum possible concentrations of OH under high-VOC conditions than under low-VOC conditions (all other parameters are held constant). Because of these high NO_x mixing ratios, more H_2SO_4 is produced under the high-VOC conditions than under the low-VOC conditions. Under the high-VOC conditions, 9% of the SO_2 has oxidized at 50 km from the source, while 6% of the SO_2 oxidized under low-VOC conditions (Table 2.2). Note that the predicted concentration of NO_x is unchanged between cases and SO_2 is only slightly changed. The higher concentrations of H_2SO_4 in the high-VOC case result in more nucleation and growth, and thus higher concentrations of aerosols at all sizes. In the low-VOC case, few particles grow to diameters larger than 30 nm within 50 km of the source, and almost no particles grow beyond 50 nm.

Although these effects of VOCs on the size distribution are not as strong as the effects of changes in the background aerosol concentrations or switching between sunny and cloudy conditions as shown above, they too are important for predicting the formation and growth of particles in plumes. An additional potentially important effect of atmospheric organics that was not tested here is the effect of secondary organic aerosol (SOA) formation in the plumes. Condensing SOA will help grow the ultrafine mode to CCN-relevant sizes (Riipinen et al., 2011; Pierce et al., 2011). The lack of SOA in our model may be part of the reason that our model predictions of the concentration of particles larger than 50 nm were biased low compared with the observations. Early in the plume, H_2SO_4 formation should dominate condensational growth; however, as the plume is diluted with background air, SOA may dominate the growth of particles in some cases. Thus, it will be important in future work to explore the effect of SOA in power-plant plume microphysics.

2.5 Conclusions

We have implemented online aerosol microphysics into an LES/CRM model. We have shown, through two case studies, that the model provides reasonable predictions of

new-particle formation and growth within the plume at distances further than 10-20 km from the source. For both cases, we predicted about one order of magnitude fewer total particles produced for each kg SO_2 emitted than the assumptions used by Adams and Seinfeld (2003) and related studies, but several orders of magnitude more particles per kg SO_2 than indicated in Dentener et al. (2006). This result was robust across all of the nucleation parameterizations we tested (except for classical binary nucleation, which predicted no new-particle formation in these warm conditions).

We have run the model using two horizontal resolutions, 400 m x 400 m and 800 m x 800 m. The discrepancy in the number of particles predicted was less than a factor of 1.5. This was less than the uncertainty in the number of particles produced due to uncertainties in VOCs or different nucleation parameterizations. We therefore expect that using a model resolution finer than 800 m x 800 m horizontal resolution would not enhance the accuracy of the model predictions at this time.

The two case studies shown here are certainly not representative of all cases, and we have included a small number of sensitivity studies to show how our results would differ under alternative aerosol background conditions and lower OH production rates. We find that for polluted background conditions, new-particle formation can be negligible. With a clean marine background, total particle numbers are about a factor of 2 larger than the remote-continental base case, and the newly formed particles grow to larger sizes. If we reduce the production rate of OH, as it would be reduced under cloudy overcast conditions, we see less new-particle formation and slower growth of all particles. In the simulated cloudy conditions, nucleation was negligible in both the moderately polluted remote continental background case and the very polluted urban background case.

We found that 9% and 4% of the emitted SO_2 oxidized to form H_2SO_4 within 50 km of the source in the Parish and Conesville cases, respectively. If the production rate of OH is decreased in the Parish case according to cloudy or low-VOC conditions, the fraction of SO_2 oxidized decreases from 9% to 0.8% or 6%, respectively. The base Parish case and the low-VOC Parish case values are larger than those chosen in many

studies (Adams and Seinfeld, 2003; Spracklen et al., 2005; Wang and Penner, 2009; Luo and Yu, 2011). However, this is implicitly accounted for to some degree by the oxidation of the emitted SO_2 in subsequent time steps in these models, and the cases here were for daytime conditions which would have above-average oxidation rates.

The work in this paper highlights how new-particle formation and growth in power-plant plumes (and anthropogenic sulphur plumes in general) depend greatly on meteorological conditions and the pre-existing particle concentrations. A power plant with constant emissions may have efficient nucleation and growth in its plume on one day, but negligible nucleation and growth on another. These results show the need for a new generation of schemes for accounting for particle formation in sub-grid sulphur plumes. Other factors that were not tested here that may be important in the plume microphysics are SO_2 and NO_x emissions rates, primary particle emissions (either as ash or H_2SO_4 formed in the plant/stack), SOA formation in the plume, wind speeds and atmospheric stability. These should also be addressed in future work.

Using the model described here, it is our intent to develop a computationally efficient, but physically based, coal-fired power plant emissions parameterization that depends on the emissions from the stack, the mean meteorological conditions and the mean background aerosol and gas concentrations that can be resolved by regional and global models. This parameterization will allow for more accurate predictions of aerosol size distributions and a greater confidence in the effects of aerosols in climate and health studies.

Until this parameterization is available, it may be wise to consider separately conditions under which it is likely there will rarely be significant aerosol nucleation within the plume. Based on our sensitivity studies, when OH concentrations are very low (for instance, at night) or when the background condensation sink is very high, it seems prudent to assume that all H_2SO_4 formed within the plume will condense onto the existing background aerosol, and that therefore aerosol mass should be increased without increasing number. Under other conditions, it may be preferable to assume

the size distribution used by Adams and Seinfeld (2003) to the size distribution assumed by Dentener et al. (2006), as the former was closer to the results we obtained for every case where particle number concentration increased inside the plume. We wish to stress that this does not imply that it will be the better assumption under all conditions, but our results suggest that it may be the better assumption under conditions when nucleation does occur.

Chapter 3

A Parameterization of Sub-Grid Particle Formation in Sulphur-Rich Plumes for Global and Regional-Scale Models.

Stevens, R. G. and Pierce, J. R.: A parameterization of sub-grid particle formation in sulphur-rich plumes for global- and regional-scale models, Atmos. Chem. Phys., 13(23), 12117-12133, doi:10.5194/acp-13-12117-2013, 2013.

3.1 Introduction

In this chapter, we develop a computationally efficient (the increase in running time for a 3D aerosol model would be negligible because the parameterization consists only of several arithmetic equations), but physically based, parameterization that predicts the characteristics of aerosol formed within sulphur-rich plumes based on parameters commonly available in global- and regional-scale models. This parameterization is based on the results of the System for Atmospheric Modelling (SAM) (Khairoutdinov and Randall, 2003), a Large-Eddy Simulation/Cloud-Resolving Model (LES/CRM) with online TwO-Moment Aerosol Sectional (TOMAS) microphysics (Adams and Seinfeld, 2002) that has been tested against aircraft observations of particle formation in plumes (Chapter 2 and Lonsdale et al., 2012). Given large-scale mean meteorological parameters ((1) wind speed, v_{g} [m s^{-1}], (2) boundary layer height, BLH [m], and (3) downward shortwave radiative flux, $DSWRF$ [W m^{-2}]), (4) emissions of SO_2, E_{SO2} [kg s^{-1}], and (5) NO_x, E_{NOx} [kg N s^{-1}], from the source, (6) mean background condensation sink, CS [s^{-1}], (7) mean background SO_2, $bgSO_2$ [ppb], and (8) NO_x, $bgNO_x$ [ppb], concentrations, and (9) the desired distance from the source, d [m], the Predicting Particle Production in Power-Plant Plumes (P6) parameterization predicts (1) the fraction of the emitted SO_2 that is oxidized to form H_2SO_4, f_{ox}, (2) the fraction of that H_2SO_4 that forms new particles instead of condensing onto pre-existing particles, f_{new}, (3) the mean mass per particle of the newly formed particles, M_{m} [kg], and (4) the number of newly formed particles per mass of SO_2

emitted, N_{new} [# (kg SO_2)$^{-1}$].

In Sect. 3.2 we provide a brief description of the SAM-TOMAS model and how the P6 training data was selected. Section 3.3 describes the form and physical basis of the P6 parameterization. The evaluation of the P6 parameterization against the full SAM-TOMAS model is presented in Sect. 3.4. We describe sensitivity studies performed using the parameterization in Sect. 3.5. Finally, we present our conclusions in Sect. 3.6.

3.2 Description of SAM-TOMAS Model and Training Data

A full description of the SAM-TOMAS model is available in Chapter 2, so we will restrict ourselves to a brief summary here. The SAM model (Khairoutdinov and Randall, 2003) is a flexible LES/CRM model with a resolution of 10s of metres to several kilometres, and a domain that can span 10s to 1000s of kilometres. The TOMAS microphysics algorithm (Adams and Seinfeld, 2002; Pierce and Adams, 2009) in SAM resolves aerosol by both mass and number independently in 15 size bins spanning 3 nm to 10 μm. Condensation, coagulation, and nucleation are explicitly resolved in the model. Sulphate, ammonia (NH_3), aerosol water, and the gas-phase concentrations of SO_2, NO_x, ammonium (NH_4) and H_2SO_4 are simulated within the model, but secondary organic aerosol formation is not explicitly simulated under the assumption that sulphate aerosol formation will dominate within sulphur-rich plumes.

The concentration of OH in the SAM-TOMAS model is currently parametrized based off of the downward shortwave radiative flux ($DSWRF$) and the concentration of NO_x. This OH parameterization is an empirical fit to results from the detailed time-dependent photochemical box model described by Olson et al. (2006). However, the uncertainties associated with the parametrized OH become large for solar zenith angles larger than 70, which, for clear-sky conditions, correspond to $DSWRF$ values less than 350 W m^{-2}. In addition, we do not account for nitrous acid (HONO) or sulphur trioxide (SO_3) emission, which may account for additional sulphuric acid formation. Both of these emissions may result in particle formation early in the plume, and may account for the under-prediction of particles within 5 km of the stack in

Chapter 2. However, we note that these processes do not seem to be necessary to accurately predict particle size and number concentrations beyond 30 km from the source. When these processes become better understood, we plan to incorporate them into a future version of the P6 parameterization.

During cloudy conditions, SO_2 may undergo aqueous oxidation through reaction with H_2O_2 or other species (Zhou et al., 2012). Currently, this is not accounted for in the SAM-TOMAS model. Therefore, SO_2 oxidation is likely underestimated under cloudy conditions. Under such conditions, however, less new-particle formation is expected because $DSWRF$, and subsequently oxidation of SO_2 though reaction with OH will also be suppressed. Also, the additional surface area from cloud droplets in the clouds and cloud-processed aerosols outside of the clouds will slow nucleation and increase coagulational losses of new particles. We therefore do not believe that this would be a significant uncertainty for predicting the number and size of aerosol formed in sulphur-rich plumes.

For this study, the model was operated as a Lagrangian 2-D wall model that passed over the power-plant after a spin-up period of 1800 seconds of model time. The wall extends upwards and horizontally perpendicular to the direction of the mean boundary-layer wind. We have evaluated the model operating in Lagrangian mode against the Eulerian mode used in Chapter 2, and we have found that the discrepancies in NO_x and SO_2 concentrations between the two models are less than one standard deviation of the concentrations (due to variability in time). Similarly, the total particle concentration within the plume differed by less than 16% between the Lagrangian and the Eulerian modes, and the particle size distributions had similar characteristics in both models. Both models compare similarly well to the measurements shown in Chapter 2.

In the simulations used here, the model resolution was held fixed at 400 x 400 x 40 m and the model domain was 120 km wide and 5 km high. We chose an empirical activation-type nucleation scheme (Kulmala et al., 2006), where nucleation rates are calculated as 10^{-7} s^{-1} $\cdot$ $[H_2SO_4]$, because this scheme provided the best match to

observations out of the 6 schemes tested in Chapter 2. We note that it is clear that such an empirical scheme will not capture all of the variability in nucleation rates. However, an increase in the nucleation rate by a factor of 10 was found in Chapter 2 to increase N_{new} by a factor of about 3 for distances greater than 30 km from the source, and we will show that values of N_{new} span six orders of magnitude across the set of training data used for this study. As more accurate parameterizations of nucleation become available, we plan to integrate them into SAM-TOMAS and incorporate the results into future versions of the P6 parameterization.

In order to determine the best-fit parameters for the P6 parameterization, we performed many simulations using the SAM-TOMAS model using a realistic range of different inputs for the emissions, meteorology, and background aerosol and trace gas concentrations. In order to choose realistic, but sufficiently diverse, conditions for the simulations, we performed the procedure described in the following three paragraphs.

Table 3.1: Parameter space used to create training data for the P6 parameterization.

Parameter	Minimum	Maximum
Latitude	30°N	70°N
Longitude	55°W	110°W
Time	July 1st, 2010, 15:00 UTC	July 28th, 2010, 21:00 UTC
Distance from source	5 km	100 km
$\log_{10}(E_{SO2}$ [kg/s])	-3	1
$\log_{10}(E_{NOx}$ [kg N/s])	-3	0.3
Emissions height	60 m	580 m

To generate a data set of realistic aerosol size distributions and trace gas concentrations, we used output from the GEOS-Chem-TOMAS model. GEOS-Chem-TOMAS uses the TOMAS aerosol microphysics module described above in the GEOS-Chem chemical transport model (www.geos-chem.org, Bey et al., 2001). The implementation of TOMAS in GEOS-Chem has been discussed previously (Pierce et al., 2013; Snow-Kropla et al., 2011; Trivitayanurak et al., 2008). Variables were output every 3 hours. The model resolution was 0.5°x 0.666°. We used Latin Hypercube sampling (a method of pseudo-randomly choosing a set of samples from a multi-dimensional space such that the full range of each dimension is sampled, but the coordinates in each

dimension are uncorrelated) to determine a set of 5000 (1) latitudes, (2) longitudes, (3) date and time, (4) distances from the emissions source (d), (5) emissions rate of SO_2 (E_{SO2}) and (6) NO_x (E_{NOx}), and (7) the effective emissions height, which implicitly includes both the height of the emissions stack and the initial buoyant rise of the plume. The range of values used for each of these variables is listed in Table 3.1. We note that while only the month of July was sampled to create the training data, the large geographic range used provided diverse meteorological conditions. As the OH parameterization used in the SAM-TOMAS model has high uncertainties for large solar zenith angles, we excluded from our range of times to be selected the hours of 3:00, 6:00, and 9:00 UTC as these should be at high solar zenith angles or outside daylight hours for the latitude and longitude range we selected. In order to further reduce the number of cases with high solar zenith angles, we subsequently excluded from our analysis any cases that had $DSWRF$ values less than 100 W m^{-2}. We then obtained the background aerosol size distribution, background SO_2 and NO_x concentrations ($bgSO_2$ and $bgNO_x$), and $DSWRF$ from the GEOS-Chem-TOMAS output that corresponded to each set of latitude, longitude, date and time. The maximum, minimum, and median values of these outputs from GEOS-Chem-TOMAS are shown in Table 3.2.

Table 3.2: Outputs from GEOS-Chem-TOMAS used as inputs for SAM-TOMAS. The fully resolved aerosol size distribution from GEOS-Chem-TOMAS was used in SAM-TOMAS, but for conciseness we only tabulate the condensation sink here. Cases where the $DSWRF$ was less than 100 were excluded from this study, because of uncertainties associated with OH production for these conditions.

Parameter	Minimum	Maximum	Median
Condensation sink [s^{-1}]	8.94×10^{-5}	1.46×10^{-2}	1.38×10^{-3}
Background SO_2 [ppb]	1.27×10^{-6}	16.6	0.0707
Background NO_x [ppb]	2.84×10^{-4}	7.93	0.0302
Downward shortwave radiative flux [W m^{-2}]	100	960	401

To drive the dynamics in SAM-TOMAS, we obtained for each set of latitude, longitude, date, and time the corresponding profiles of potential temperature, water vapour mixing ratio, wind speed and direction; surface fluxes of sensible heat, latent

heat, and momentum; the boundary-layer height (BLH, defined as the height where the turbulent kinetic energy falls below a threshold value) and the surface pressure from the National Center for Environmental Prediction (NCEP) North American Regional Reanalysis (NARR) (Mesinger et al., 2006) assimilated meteorology data, as was done in Chapter 2. The reanalysis data were provided by the National Oceanic and Atmospheric Administration (NOAA), Ocean and Atmospheric Research (OAR), Earth System Research Laboratory (ESRL) Physical Sciences Division (PSD), Boulder, Colorado, USA, from their website at: http://www.esrl.noaa.gov/psd/. The NCEP NARR data was chosen for this study because the software necessary to create input files from reanalysis data was readily available. We note that while the meteorology from the reanalysis data may not correspond exactly to the data from the GEOS-Chem-TOMAS model due to differences in spatial and temporal resolution, an exact match is not necessary to create a realistic set of training inputs.

Table 3.3: Minimum, maximum, and median values of the mean boundary-layer wind speeds and the boundary-layer heights for the training data used to create P6.

Parameter	Minimum	Maximum	Median
Wind speed [m s^{-1}]	0.178	26.1	5.98
Boundary-layer height [m]	53	2792	434

For each simulation using the SAM-TOMAS model, we used E_{SO2}, E_{NOx} and effective emissions height from the Latin hypercube sample; the background aerosol size distribution, $bgSO_2$, $bgNO_{\mathrm{x}}$, and $DSWRF$ from the output of the GEOS-Chem-TOMAS model; and the SAM-TOMAS meteorology that was driven by nudging and boundary conditions from the NCEP-NARR assimilated meteorology data. We ran the model until the emissions reached the distance from the source specified from the Latin hypercube sample. We preserved the following variables as training inputs for the P6 parameterization: (1) E_{SO2}, (2) E_{NOx}, (3) total condensation sink of the background aerosol size distribution (CS), (4) $DSWRF$, (5) the mean wind speed within the boundary layer (v_{g}), (6) BLH, (7) the distance from the source (d), (8) $bgSO_2$, and (9) $bgNO_{\mathrm{x}}$. The maximum and minimum values of these parameters are shown in Tables 3.1, 3.2, and 3.3. Other information necessary to run the SAM-TOMAS model, such as the effective emissions height, the potential temperature

profile, the water vapour mixing ratio profile, and the surface fluxes may not be available in many regional- and global-scale models and the current P6 inputs capture most of the variability in aerosol formation and growth within plumes, as we will show in Sect. 3.5. We have therefore excluded them as inputs to the parameterization. However, by including a wide range of these conditions in the simulations used to fit the parameterization, we hope to exclude a possible bias in our predictions, and to have a more realistic assessment of the accuracy of the parameterization.

3.3 Description of the Parameterization

The purpose of the Predicting Particle Production in Power-Plant Plumes (P6) parameterization is to predict the fraction of emitted SO_2 that is oxidized in the plume (f_{ox}), whether or not a significant number of new particles are nucleated, the number of new particles nucleated per kg SO_2 emitted (N_{new}, [# (kg SO_2)$^{-1}$]), the mean mass per particle of the new particles (M_{m}, [kg]), and the fraction of the H_2SO_4 formed within the plume that comprises new particles (f_{new}).

As inputs to the parameterization, we have chosen variables that are commonly available in global- and regional-scale models: the source-level SO_2 and NO_x emissions (E_{SO2} [kg s^{-1}] and E_{NOx} [kg N s^{-1}]), the downward shortwave radiative flux at the surface ($DSWRF$ [W m^{-2}]), the background aerosol condensation sink (CS [s^{-1}]), the boundary layer height (BLH [m]), the mean wind speed in the boundary layer (v_{g} [m s^{-1}]), the distance from the source (d [m]) that the plume is considered mixed with the model grid boxes, and the background SO_2 and NO_x concentrations ($bgSO_2$ [ppb] and $bgNO_x$ [ppb]). We will consistently use the given units for all inputs and outputs in all of the following equations.

Often, emissions inventories provide SO_2 and NO_x emissions within each box on a given grid, instead of associated with particular sources specifically. Therefore, it may not be known how many power plants are responsible for the emissions in a given grid box. We therefore allow the P6 parameterization to be operated in the following ways: (1) By default, it is assumed that the emissions of each anthropogenic sulphur-rich point source are known individually, in which case f_{ox}, N_{new}, M_{m}, and f_{new} will be

Table 3.4: Emissions rates for coal-fired power-plants in the USA from the 2010 EPA CAM data. "Medium" emissions are defined as the log-space mean, "high" as one standard deviation above the mean, and "low" as one standard deviation below the mean.

	SO_2	NO_x
high	1.00 kg s^{-1}	0.290 kg s^{-1}
medium	0.202 kg s^{-1}	0.0840 kg s^{-1}
low	0.0606 kg s^{-1}	0.0300 kg s^{-1}

predicted for each source plume individually. (2) If instead the total emissions of SO_2 and NO_x from sulphur-rich sources within a given area (but not the individual sources within that area) are known, the P6 parameterization will provide outputs based on the assumption that the emissions for the sources are divided between an equal number of high-emitters, medium-emitters, and low-emitters. We define high-emitters, medium-emitters, and low-emitters based on the emissions data for power-plants in the United States compiled from the Clean Air Markets (CAM) data (United States Environmental Protection Agency, 2012) as follows: for medium-emitters, we use the log-space mean emission rates for a power plant in the USA during 2010. For low and high emitters, we use an emission rate that is one standard deviation below or above the mean in log space, respectively. The high, median, and low emissions rates are listed in Table 3.4. (3) If the SO_2 emissions are known, but the NO_x emissions are not known (or the NO_x emissions from the major SO_2 sources are not known), the median SO_2:NO_x emissions ratio of 0.419 from the 2010 EPA CAM data will be assumed (as well as the high-, medium- and low- emitter assumptions from the previous P6 mode).

Even if the precise locations of power plants are known, it may not be clear at what distance from the source the particles are well-mixed within a grid box that also contains the source of emissions. However, as we will show in Sect. 3.5, the P6 values of $M_{\rm m}$, $N_{\rm new}$, and $f_{\rm new}$ are not strongly sensitive to the distance from the source beyond distances of 30 km, and $f_{\rm ox}$ depends less than linearly on the distance from the source.

In the following subsections, we describe the theory and semi-empirical fits behind the P6 parameterization.

3.3.1 Fraction Oxidized

In order to formulate a semi-empirical equation for f_{ox}, we first formulate a semi-empirical equation for the effective NO_x mixing ratio within the plume because NO_x modulates the OH concentrations and thus affects the oxidation rate of SO_2. The mean concentration of NO_x within the plume should be equal to the sum of the contributions from the background and the emitted NO_x after accounting for dilution, which should be related to v_g, BLH, and the time since emission, calculated as (d/v_g). We therefore calculate the effective NO_x concentration, $NO_{x,eff}$ [ppb], as:

$$NO_{x,eff} = bgNO_x + 1.444 \times 10^{-8} \frac{E_{NOx}}{{v_g}^{1.234}\, BLH^{0.2018}\, (\frac{d}{v_g})^{0.7902}} \tag{3.1}$$

where the exponents for v_g, BLH, and (d/v_g) have been fit for this equation to the average concentrations of NO_x in the plume using the training data (evaluation of the fit in Sect. 3.4). We allowed the scaling factor of 1.444×10^{-8} to be freely fit to the data, because the relative importance of the background concentrations and the emitted NO_x is different for f_{ox} than it is for the mean concentration of NO_x. As the relative importance of background and emitted NO_x is also different for determining nucleation, M_m, and N_{new}, we list the scaling factors used to calculate $NO_{x,eff}$ for each of these outputs in Table 3.5. The scaling factor found when fitting to the mean NO_x concentration within the plume was 9.595×10^4. However, the best fit scaling factor found for calculating f_{ox} is much lower, such that the $NO_{x,eff}$ is dominated by $bgNO_x$. Generally, NO_x concentrations are sufficiently high within the centre of the plume (and early in the plume) to prevent fast oxidation of SO_2, so the background concentrations are relatively much more important to f_{ox} than they are to the mean NO_x concentration within the plume.

We calculate an effective OH concentration using the same parameterization that is used in the SAM-TOMAS model. This parameterization calculates the OH concentration as a function of the NO_x concentration within the plume and the $DSWRF$. The parameterization, which is a fit of chemistry box-model simulations of Olson et al. (2006), was originally described in appendix A of Stevens et al. (2012), and this description is repeated as appendix A of this manuscript.

Table 3.5: Emissions scaling factors used in the P6 parameterization for determining effective SO_2 and NO_x concentrations (Eq. 3.1 and Eq. 3.9)

	E_{NOx} scaling factor	E_{SO2} scaling factor
In-plume mean concentration	9.595×10^{4}	1.705×10^{4}
f_{ox}	1.444×10^{-8}	-
nucleation	4.365×10^{5}	2.239×10^{4}
M_m	2.139×10^{7}	2.605×10^{6}
N_{new}	1.243×10^{6}	-

First, we set variables x and y:

$$x = \log(NO_{x,eff}) - 0.195 \tag{3.2}$$

$$y = \frac{DSWRF}{S_0 \cdot T} \tag{3.3}$$

where S_0 is the solar constant at the top of the atmosphere, 1370 W m^{-2}, and T is an assumed transmittance of the clear atmosphere, 0.76. We then calculate two polynomials, the first ($P1$) estimating the shape of the OH versus NO_x relationship, and the second ($P2$) capturing the dependance of OH on $DSWRF$:

$$P1 = -0.014x^6 + 0.0027x^5 + 0.1713x^4 - 0.0466x^3 - 0.7893x^2 - 0.1739x + 6.9414 \tag{3.4}$$

$$P2 = (-1345y^3 + 4002y^2 - 471.8y + 42.72) \cdot 10^4 \tag{3.5}$$

From $P1$ and $P2$, we calculate the effective OH concentration, OH_{eff}, [molec cm^{-3}]:

$$OH_{eff} = 0.82 \cdot 10^{P1 \cdot \log(P2)/6.8} \tag{3.6}$$

If we assume that the only loss mechanism for SO_2 is through reaction with OH (e.g. clear skies and ignore reactions with Criegee intermediates (Mauldin et al., 2012)), and we knew the true OH concentrations, we could calculate f_{ox} by using the rate constant k, the time elapsed t and the following equation:

$$f_{ox} = 1 - \exp(-k\,[\mathrm{OH}]\,t) \tag{3.7}$$

However, given that OH_{eff} is not the true concentration, and we must calculate t as d/v_g, we use the analogous equation:

$$f_{ox} = 1 - \exp(-1.650 \times 10^{-10} {OH_{eff}}^{0.7904} (\frac{d}{v_g})^{0.7723}) \tag{3.8}$$

where the numerical values have been selected by minimizing the error between the P6 fit f_{ox} values and the predicted f_{ox} from the SAM-TOMAS simulations. As the best-fit E_{NOx} scaling factor for calculation of $NO_{x,eff}$ is near zero, OH_{eff} is approximately equal to the OH concentration outside of the plume in the f_{ox} calculation. Since NO_x concentrations will generally be sufficiently high within the plume that OH within the plume is less than at the plume edges, the best fit exponent for OH_{eff} is less than one. Oxidation of SO_2 subsequently proceeds more slowly within the plume than at the edges, thus the best-fit exponent for (d/v_g) is also less than one.

3.3.2 Nucleation

In order to determine whether or not significant nucleation occurs within the plume, we first calculate the effective NO_x and SO_2 concentrations within the plume. The effective SO_2 concentration, $SO_{2,eff}$ [ppb], is defined similarly to $NO_{x,eff}$ as:

$$SO_{2,eff} = bgSO_2 + 2.239 \times 10^4 \frac{E_{SO2}}{{v_g}^{1.229}\, BLH^{0.1891}\, (\frac{d}{v_g})^{0.7732}} \tag{3.9}$$

where the exponents for v_g, BLH, and (d/v_g) have been fit for this equation to the average concentration of SO_2 in the plume. The scaling factor found when fitting to the mean SO_2 concentration within the plume was 1.705×10^4. The scaling factors for $SO_{2,eff}$ and $NO_{x,eff}$ for determining nucleation are 2.239×10^4 and 4.365×10^5, respectively, as listed in Table 3.5.

We then calculate *nucp*, our predictor for if nucleation is likely, from the following equation:

$$nucp = \frac{{SO_{2,eff}}^{1.92}\, DSWRF^{3.28}}{{NO_{x,eff}}^{1.24}\, CS^{3.48}} \tag{3.10}$$

We compare the value of *nucp* to 2.988×10^{14}. If it is smaller, then we predict that nucleation is slow and that any particles that are formed within the plume will be quickly lost to coagulation: there will be no net increase in particle number within the plume. If it is larger, we predict that significant new-particle formation will occur. This test is accurate for 95.8% of our training cases. For those cases where nucleation is falsely predicted or falsely not predicted, the maximum P6 or SAM-TOMAS values of M_m, respectively, were less than the median values of M_m for the full set of training

data. The maximum number of new particles formed was similarly lower than the median for the full set of training data. Particle formation rates and growth rates were therefore typically lower for the cases where this test was incorrect than for the correctly-predicted cases.

3.3.3 Mean Mass per Particle of New Particles

If we predict that there will be significant nucleation, we then predict the mean mass per particle of the newly formed particles. We expect that the particles will be growing primarily through condensation of available H_2SO_4. Therefore, we expect that the mean mass per particle, M_{m}, will be proportional to the product of the time elapsed (d/v_{g}), f_{ox} and $SO_{2,\mathrm{eff}}$. Since the pre-existing particles will be competing for the available H_2SO_4, we divide this value by the background condensation sink, CS, the first-order rate constant of the loss of condensible vapour by condensation, which is proportional to the Fuchs-corrected surface area of the particles (Kerminen et al., 2004). We add a constant minimum value to this, which corresponds to the smallest size of aerosol that can be resolved by the SAM-TOMAS model. In this way we arrive at the following equation for M_{m}:

$$M_{\mathrm{m}} = 1.475 \times 10^{-27} \left(\frac{{f_{\mathrm{ox}}}^{1.517}\, {SO_{2,\mathrm{eff}}}^{1.094}}{CS^{0.6173}}\right)\left(\frac{d}{v_{\mathrm{g}}}\right)^{0.9685} + 4.071 \times 10^{-23}\mathrm{kg} \qquad (3.11)$$

Again, we include the fitted parameters in this equation, and the fit will be evaluated in Sect. 3.4.

However, we note that the free parameters for predicting f_{ox} were optimized to reduce the rms absolute error between the parametrized f_{ox} and the SAM-TOMAS predicted f_{ox} to a minimum, and we are more interested in minimizing the rms relative error in M_{m}, since M_{m} spans several orders of magnitude. We therefore allowed the free parameters used to predict f_{ox} to change when we sought the parameters that minimize the root-mean-square error in $\log_{10}(M_{\mathrm{m}})$. Notably, the E_{NOx} scaling factor (Eq. 3.1) used within the calculation of M_{m} is several orders of magnitude larger than that used within the calculation of f_{ox}, as listed in Table 3.5. We will discuss this difference further in Sect. 3.5.

We can calculate the mass mean diameter D_{mass} [μm] as:

$$D_{\mathrm{mass}} = (\frac{M_{\mathrm{m}}}{\rho}\frac{6}{\pi})^{\frac{1}{3}} \tag{3.12}$$

where ρ is the density of the dry aerosol (assumed in SAM-TOMAS as 1770 kg m^{-3}). The number-median diameter D_m [μm] can be calculated from:

$$D_{\mathrm{m}} = D_{\mathrm{mass}} \exp(-3.5 \ln^2 \sigma_{\mathrm{g}}) \tag{3.13}$$

where σ_{g} is the geometric standard deviation of the aerosol size distribution. We choose a value of 1.4 for σ_{g}, as this was the median value found for lognormal distributions fitted to the aerosol size distributions of the training data.

3.3.4 Number of New Particles per kg SO_2 Emitted

As mentioned in Sect. 3.2, we have configured the SAM-TOMAS model to use activation-type nucleation for this study. We would therefore expect the source of new particles to increase due to nucleation proportionally with the concentration of H_2SO_4, which should be roughly proportional to f_{ox}. We would therefore expect a solution that is proportional to f_{ox} and increases with increasing $bgSO_2$, but not E_{SO2}, as N_{new} is normalized by the SO_2 emissions. We also expect the primary loss mechanism for the newly formed particles to be coagulation with pre-existing particles, and this coagulational loss rate is roughly proportional to the condensation sink. We would therefore also expect the solution to exponentially decay with $CS \cdot (d/v_{\mathrm{g}})$. We find the following solution for N_{new}:

$$N_{\mathrm{new}} = 6.939 \times 10^{23} \frac{{f_{\mathrm{ox}}}^{0.9949}\, {bgSO_2}^{0.2500}}{{E_{\mathrm{SO2}}}^{0.1280}} \exp(-4.417\, CS^{0.1441} (\frac{d}{v_{\mathrm{g}}})^{0.1736}) \tag{3.14}$$

where the free parameters for f_{ox} have been fitted to minimize the root-mean-square error in log10(N_{new}), as was the case for M_{m} above. Similar to M_{m}, the E_{NOx} scaling factor (Eq. 3.1) used to calculate f_{ox} in N_{new} is several orders of magnitude greater than that used to calculate f_{ox}, as listed in Table 3.5. This will be discussed further in Sect. 3.5. We note that the P6 fit value for N_{new} slightly decreases with increasing E_{SO2}. As N_{new} is normalized by the SO_2 emissions, this is consistent with the number of new particles formed in a given plume increasing slightly less than linearly with increasing SO_2 emissions.

3.3.5 Fraction of Sulphate Mass that Comprises New Particles

The mass of new particles per kg SO_2 emitted can be determined from the product of M_{m} and N_{new}. The product of f_{ox} and f_{new} also yields the mass of SO_2 that ultimately forms new particles per kg SO_2 emitted. We therefore can calculate f_{new} from the other three outputs:

$$f_{\mathrm{new}} = \frac{M_{\mathrm{m}} N_{\mathrm{new}}}{f_{\mathrm{ox}}} \frac{M_{\mathrm{SO2}}}{M_{\mathrm{H2SO4}}} \tag{3.15}$$

where M_{SO2} and M_{H2SO4} are the molar masses of SO_2 and H_2SO_4, respectively.

However, because the fits for M_{m}, N_{new} and f_{ox} were performed independently, this equation can yield values for f_{new} greater than 1 under some conditions, which is unphysical. Under such circumstances, we reduce M_{m} and N_{new} each by a factor of ${f_{new}}^{0.5}$ to maintain closure, and limit f_{new} to 1.

3.4 Comparison of Parameterization to Full SAM-TOMAS Model

Table 3.6: Quality of fit information for the P6 parameterization predicted outputs and the results of SAM-TOMAS.

	correlation coefficient	rms error	rms $\log_{10}$ error	fraction within a factor of 2	fraction within a factor of 10
f_{ox}	0.826	0.0190	0.845	50.3%	77.0%
M_{m}	0.891	1.38×10^{-19} kg	0.425	60.0%	96.7%
N_{new}	0.670	4.85 x 10^{18} (kg SO_2)$^{-1}$	0.741	36.2%	84.6%
f_{new}	0.650	0.289	1.07	28.6%	66.8%

We show the correlation coefficient, root-mean-square error, root-mean-square error in the logarithm of the values, and the fraction of the training data cases within a factor of two or ten for each of the outputs in Table 3.6. We also show the P6 predicted values against the SAM-TOMAS calculated values for f_{ox}, M_{m}, N_{new}, and f_{new} in Fig. 3.1. We show the values of M_{m}, N_{new}, and f_{new} only for cases where nucleation is predicted to occur.

The correlation between the P6 and SAM-TOMAS values of f_{ox} is good (R = 0.826). The rms error is comparable to the value of f_{ox} for the majority of the training cases,

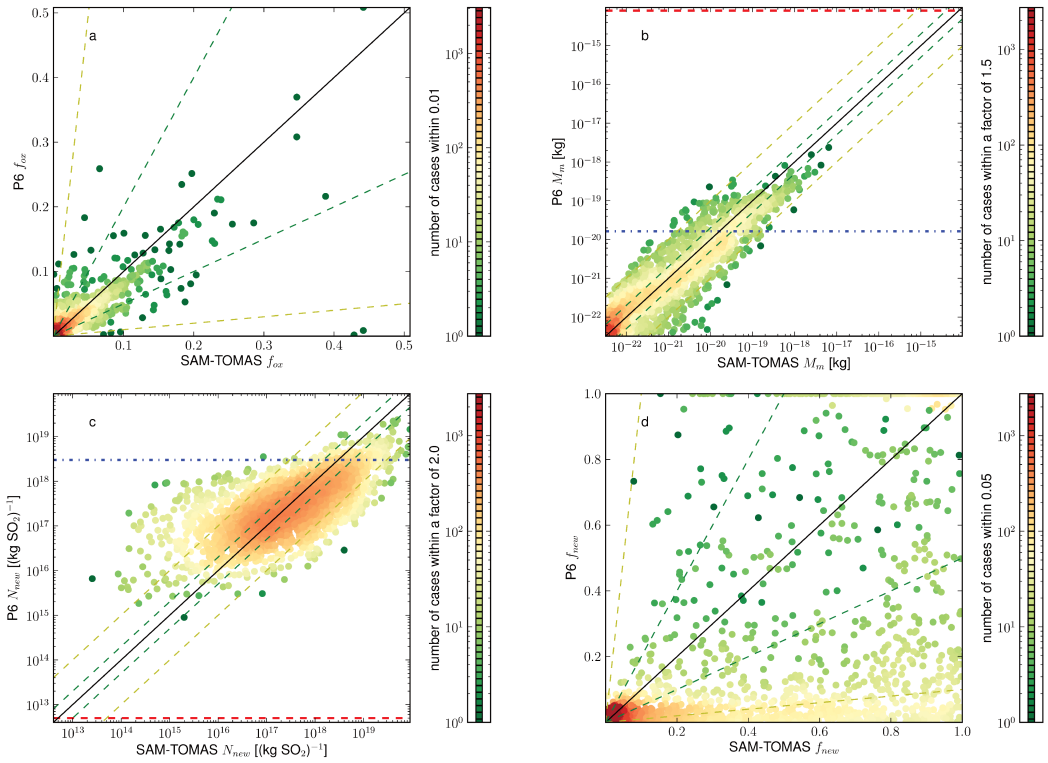

Figure 3.1: P6 vs SAM-TOMAS values of f_{ox}, M_{m}, N_{new}, and f_{new}. Color of points indicates density of cases. The red dashed lines indicate the values of M_{m} and N_{new} from Dentener et al. (2006), and the blue dashed-dotted line indicate the values of M_{m} and N_{new} from Adams and Seinfeld (2003). The green and yellow dashed lines indicate where the predicted values are within a factor of two and ten, respectively, of the calculated values.

but this value is dominated by the small number of cases where either the P6 value, the SAM-TOMAS value, or both values of f_{ox} are large. As can be seen in Fig. 1a, a large fraction (69%) of cases have both P6 and SAM-TOMAS f_{ox} less than 0.02, and the relative error can be large for these cases while the absolute error remains low.

The correlation between the P6 and SAM-TOMAS values of M_{m} is also good (R = 0.864). While the SAM-TOMAS values of M_{m} span more than five orders of magnitude, we note that the P6 values are within one order of magnitude of the SAM-TOMAS values for nearly all (96.8%) of the training cases, and for the majority of the cases (59.5%), they are within a factor of two. Along with the P6 and SAM-TOMAS values of M_{m}, we also plot the values used by (Dentener et al., 2006) and (Adams and Seinfeld, 2003) for M_{m} in Fig. 3.1b. We note that the value of M_{m} from (Dentener

et al., 2006) is more than three orders of magnitude larger than the largest value calculated by SAM-TOMAS for the training simulations. The value from Adams and Seinfeld (2003) is within the range of values predicted by SAM-TOMAS, but is more than two orders of magnitude larger than the median value of M_{m} for the training simulations. There is a large fraction of new-particle-formation cases (40%) where both P6 and SAM-TOMAS values of M_{m} do not exceed 2×10^{-22} kg, corresponding to a mass mean diameter of less than 6 nm.

While the P6 parameterization does not capture the behaviour of N_{new} as well as it captures the behaviour of f_{ox} and M_{m}, the P6 values are still within one order of magnitude of the SAM-TOMAS values for most (83.8%) of the training cases, across which the SAM-TOMAS values vary by more than six orders of magnitude. In addition to the P6 and SAM-TOMAS values of N_{new}, we also plot the values used by (Dentener et al., 2006) and (Adams and Seinfeld, 2003) for N_{new} in Fig. 3.1c. We note that the value of N_{new} from (Dentener et al., 2006) is more than two orders of magnitude smaller than the smallest value calculated by SAM-TOMAS for the training simulations. The value from Adams and Seinfeld (2003) is within the range of values predicted by SAM-TOMAS, but is nearly one order of magnitude larger than the median value of N_{new} for the training simulations.

As the P6 values of f_{new} are calculated based on f_{ox}, M_{m}, and N_{new}, instead of being fit directly to the SAM-TOMAS values, we would expect this variable to show the poorest fit to the SAM-TOMAS values. Since f_{ox} and f_{new} are uncorrelated, there will be instances where the value of f_{ox} is small, and hence the relative error in f_{ox} may be high, but the value of f_{new} is not small. Since f_{new} is calculated using f_{ox}, a large relative error in f_{ox} will yield a large relative error in f_{new}, and so this means that the relative error in f_{new} can be high, even for larger values of f_{new} (hence the absolute error will also be large). However, the correlation between the P6 and SAM-TOMAS f_{new} values remains good (R = 0.667) largely due to resolving the cluster of values near 0 and the cluster near 1 (Fig. 3.1d). The P6 parameterization correctly predicts low values for f_{new} for the large fraction (56%) of training cases where the SAM-TOMAS value of f_{new} is less than 0.1, and the P6 value of f_{new} is within 0.1 of

the SAM-TOMAS value for 63.3% of the cases.

3.5 Sensitivity Studies

3.5.1 Sensitivities to Inputs

We show the sensitivities of f_{ox}, M_{m}, N_{new}, and f_{new} to each of the P6 inputs in Figures 3.2, 3.3, 3.4, and 3.5, respectively. Each figure shows green lines for 100 randomly chosen sets of inputs within the ranges of the training data. The black line shows the sensitivity from the set of median values for each input ($E_{\mathrm{SO2}} = 0.1$ kg s^{-1}, $E_{\mathrm{NOx}} = 0.05$ kg s^{-1}, d = 50 km, other values shown in Tables 3.2 and 3.3). In each panel, one of the input variables is varied while the others are held fixed. In order to higlight the sensitivities to the inputs, each plotted line is shifted vertically to the centre of the subplot. For Fig. 3.2 (f_{ox}) and Fig. 3.5 (f_{new}), we subtract the median value of each line from its values. For Fig. 3.3 (M_{m}) and Fig. 3.4 (N_{new}), each plotted line is divided by its median value. We do not show values for M_{m}, N_{new}, or f_{new} where nucleation is not predicted to occur by the P6 parameterization. Therefore, some lines begin or end in Figures 3.3, 3.4, and 3.5 as the threshold for nucleation is crossed (Eq. 3.10)

The value of f_{ox} (Fig. 3.2) is insensitive to E_{SO2}, CS, and $bgSO_2$, as one would expect. The value of f_{ox} is also insensitive to E_{NOx}. As we note in Sect. 3.3.1, oxidation generally proceeds much more quickly at the plume edges and in the dilute plume than at the plume centre, so f_{ox} is far more sensitive to $bgNO_{\mathrm{x}}$ than to E_{NOx}. As BLH may only affect f_{ox} in the P6 parameterization through the dilution of NO_{x} emissions, f_{ox} is also insensitive to BLH. The value of f_{ox} is determined by the remaining four inputs. The value of f_{ox} increases with increasing time since emission, and so nearly linearly increases with increasing d and is nearly inversely proportional to v_{g}. The dependance of f_{ox} on $DSWRF$ and $bgNO_{\mathrm{x}}$ is determined largely by the dependance of OH on these two variables, as parametrized in SAM-TOMAS. The value increases with increasing $DSWRF$, and there is a peak in f_{ox} at $bgNO_{\mathrm{x}}$ equal to 1 ppb.

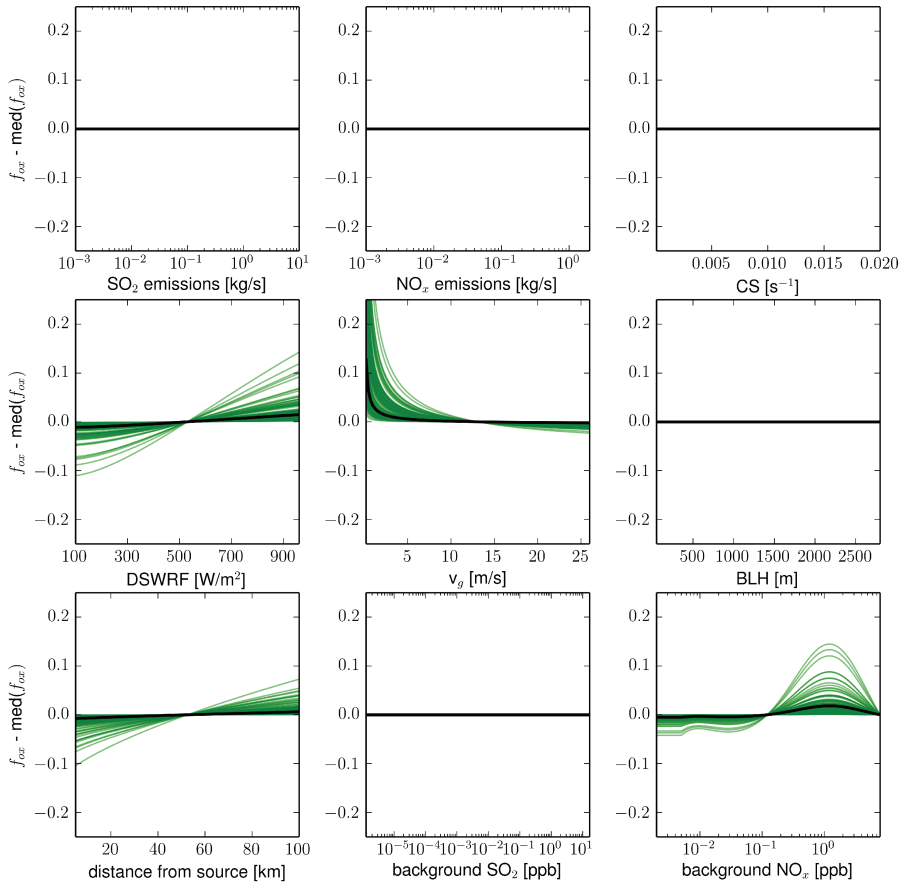

Figure 3.2: Sensitivity of f_{ox} to each of the inputs for 100 randomly selected sample inputs. The black line denotes the median value case. The median value of each plotted line is subtracted from its values to highlight the sensitivities to the inputs.

The value of M_{m} is much more sensitive to E_{NOx} than to $bgNO_{\mathrm{x}}$, unlike f_{ox}. Concentrations of SO_2 are highest close to the source, so concentrations of H_2SO_4 (and particle growth rates) may also be highest close to the source, even if SO_2 is being oxidized more slowly. The concentrations of H_2SO_4 close to the source will be more sensitive to NO_x emissions than to background NO_x concentrations, and therefore M_{m} is also more sensitive to E_{NOx} than $bgNO_{\mathrm{x}}$. This is also reflected in the dependencies of M_{m} on d and on v_{g}. The value of f_{ox} is nearly linearly increasing with d, while M_{m} increases at low values of d but becomes insensitive at higher values. The value of M_{m} is much less sensitive than f_{ox} to v_{g}, although this is convoluted by the effect of v_{g} on

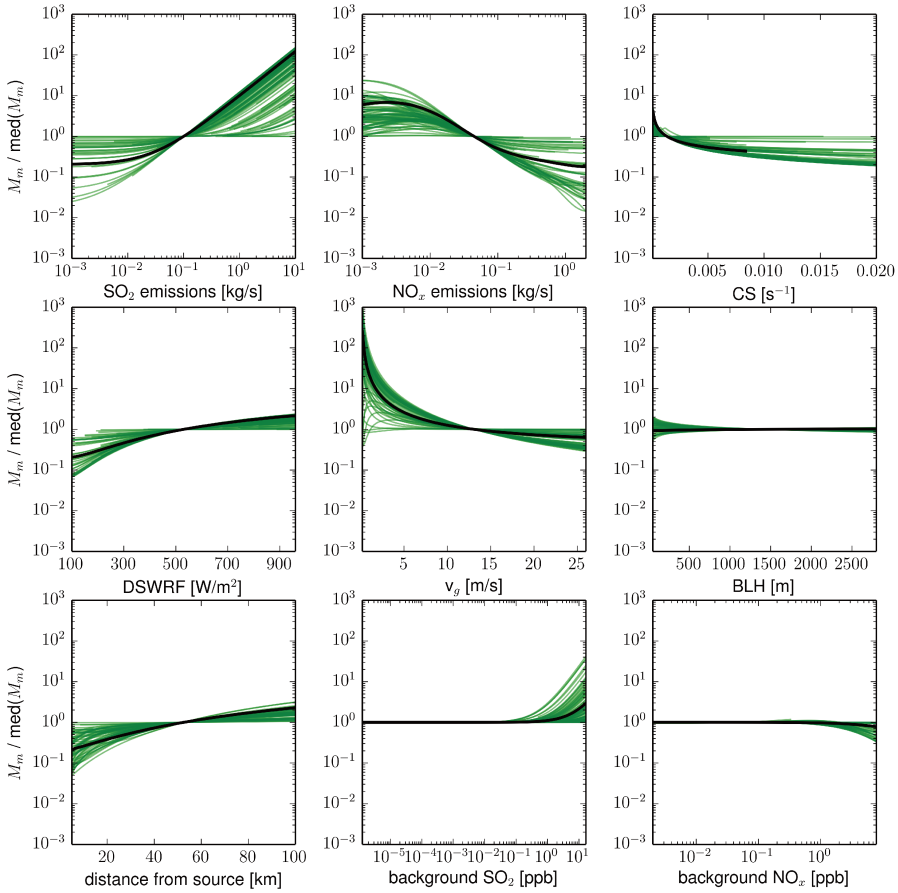

Figure 3.3: Sensitivity of $M_{\rm m}$ to each of the inputs for 100 randomly selected sample inputs. If nucleation is not predicted by the P6 parametrization, no value is shown. The black line denotes the median value case. Each plotted line is divided by its median value in order to highlight the sensitivities to the inputs.

$M_{\rm m}$ through dilution of SO_2 and $NO_{\rm x}$ emissions, which is also the cause of the slight dependance of $M_{\rm m}$ on BLH. There is a decrease in $M_{\rm m}$ with increasing CS, due to the loss in available H_2SO_4 to pre-existing particles. We also note that $M_{\rm m}$ becomes insensitive to $E_{\rm SO2}$, $bgSO_2$ and $bgNO_{\rm x}$, as well as $E_{\rm NOx}$ under some conditions, at small values of each of these inputs. If the background concentrations of $NO_{\rm x}$ or SO_2 are sufficiently low compared to emissions, in-plume $NO_{\rm x}$ or SO_2 will be dominated by the emissions, and so further reductions in the background concentrations will not significantly affect $M_{\rm m}$. The reverse is also true if the emissions are sufficiently low

compared to the background concentrations.

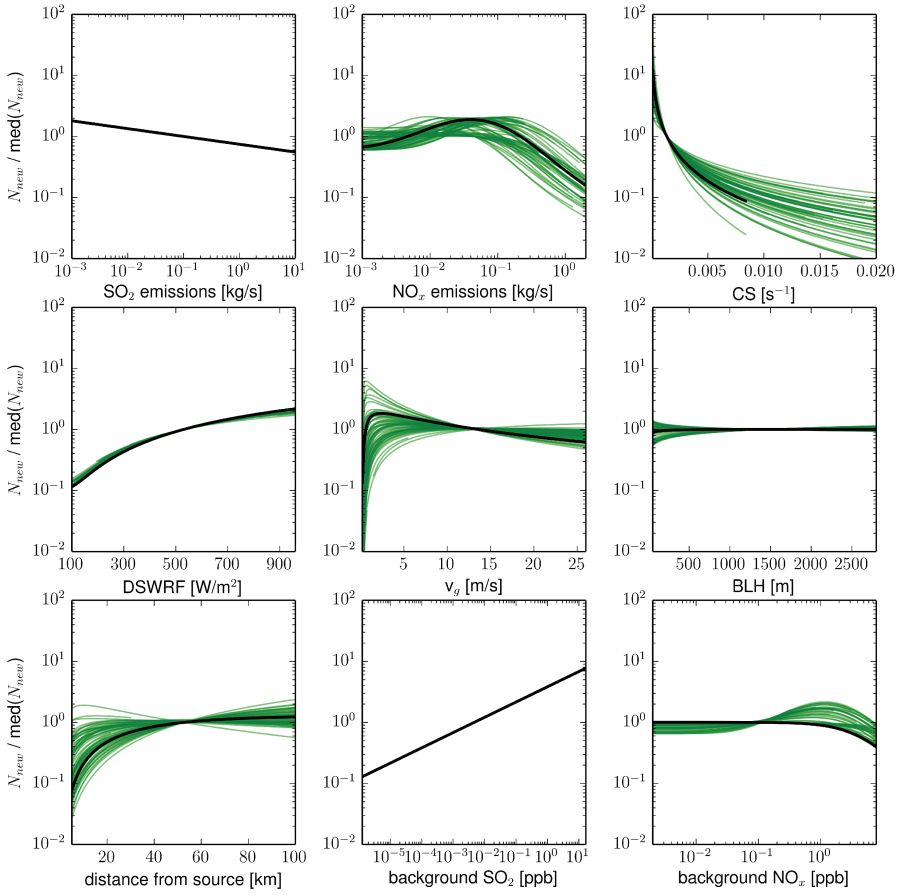

Figure 3.4: Sensitivity of N_{new} to each of the inputs for 100 randomly selected sample inputs. If nucleation is not predicted by the P6 parametrization, no value is shown. The black line denotes the median value case. Each plotted line is divided by its median value in order to highlight the sensitivities to the inputs.

The value of N_{new} depends on the inputs in a similar manner to M_{m}. It decreases with increasing CS due to both removal of new particles by coagulation and competition for available H_2SO_4. It increases with increasing $DSWRF$. The value of N_{new} is more sensitive to E_{NOx} than to $bgNO_{\mathrm{x}}$. However, N_{new} increases with increasing $bgSO_2$, but decreases with increasing E_{SO2}. Increases in either emissions of SO_2 or the background concentration of SO_2 will increase the available H_2SO_4, thus

increasing new-particle formation, but because N_{new} is defined as the number of new particles normalized by the emissions of SO_2, and emissions of SO_2 less than linearly increase the number of new particles, increases in the emissions of SO_2 have a small decreasing effect on N_{new}. The value of N_{new} also has a complex dependance on v_{g} and d, either increasing or decreasing with increasing d and decreasing v_{g}. As the time since emission (d/v_{g}) increases, N_{new} will increase due to continuing new-particle formation and will decrease due to coagulational scavenging by pre-existing particles. The dependance of N_{new} on d and v_{g} will depend on the competition between these two processes. We do note, however, that N_{new} tends to asymptote to a single value with increasing d, depending on the values of the other inputs.

Of the four outputs of the P6 parameterization, f_{new} shows the most dramatic changes for small changes in some of the inputs. Specifically, f_{new} is sensitive to small changes for high values of E_{SO2}, high values of $bgSO_2$, low values of CS, and, for some combinations of inputs, low values of v_{g}. The value of f_{new} is less sensitive to the remaining variables, but increases for increasing $DSWRF$ and d, decreases slightly for increasing BLH, and generally decreases with decreasing $bgNO_{\mathrm{x}}$.

3.5.2 Sensitivity to Number of Sources Assumed

Often, anthropogenic emissions inventories give emissions of SO_2 and NO_{x} on a given grid, and not per point source. Figure 3.6 shows the sensitivity of the P6 parameterization to assumptions about how these emissions are split between sources within the grid box. We used the P6 parameterization to predict f_{ox}, M_{m}, N_{new}, and f_{new} for 100 different sets of inputs randomly chosen from the range of values tested for each variable, assuming the emissions were split evenly amongst between 1 and 10 point sources. We also show the sensitivity for the median case as a black line, as we did in Figures 3.2, 3.3, 3.4, and 3.5. As in Figures 3.2, 3.3, 3.4, and 3.5, we shift the lines vertically to highlight the sensitivities, by subtracting the median value of each plotted line from its values for f_{ox} and f_{new} and dividing each plotted line by its median value for M_{m} and N_{new}. We do not show values for M_{m}, N_{new}, and f_{new} for cases where no nucleation is predicted. As the value of f_{ox} is insensitive to both E_{SO2} and E_{NOx}, it is also completely insensitive to assumptions about the number of

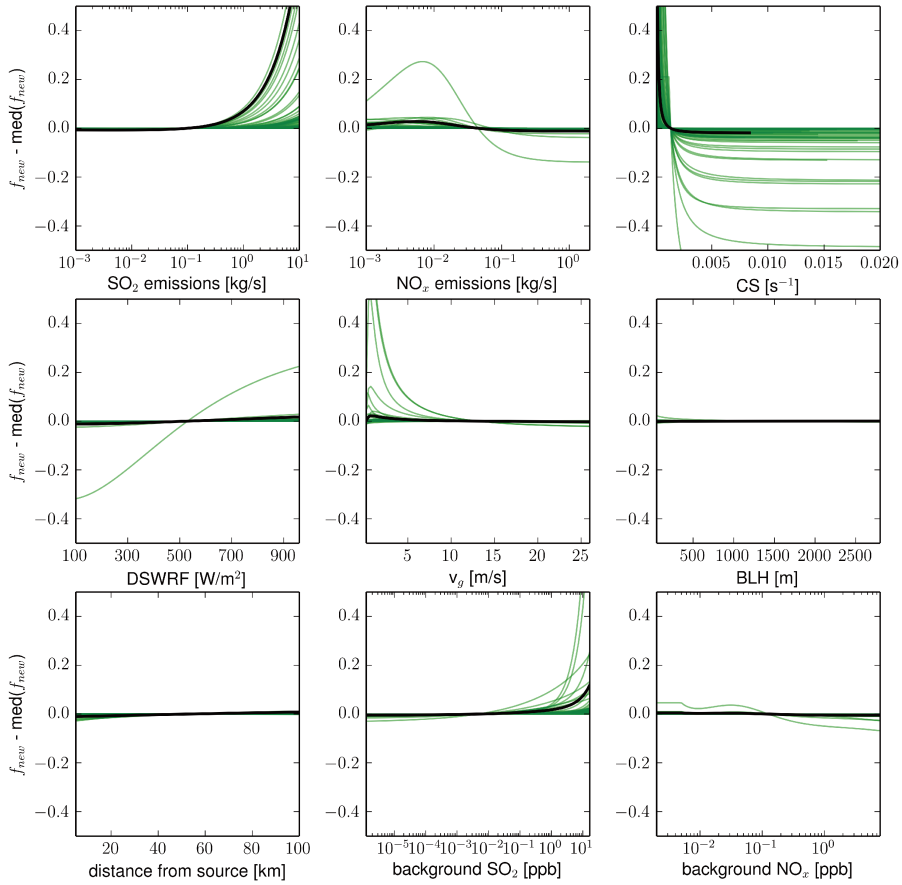

Figure 3.5: Sensitivity of f_{new} to each of the inputs for 100 randomly selected sample inputs. If nucleation is not predicted by the P6 parametrization, no value is shown. The black line denotes the median value case. The median value of each plotted line is subtracted from its values to highlight the sensitivities to the inputs.

point sources. Since M_{m} increases with increasing E_{SO2} but decreases with increasing E_{NOx} across most of the ranges of these two variables, M_{m} may increase or decrease as the emissions are split amongst additional sources. The value of N_{new} decreases with increasing E_{SO2}, but peaks for E_{NOx} values near 0.05 kg s^{-1}, and so may also increase or decrease as E_{NOx} is split amongst a larger number of sources. We tested 10,000 randomly generated samples within the range of inputs used for the training data, and for an increase in the number of sources from 1 to 10, the values of M_{m} and N_{new} stayed within a factor of 3 for 64% and 85% of the cases, respectively (note that

values for M_{m} and N_{new} span 5 and 3 orders of magnitude, so a factor of 3 change is small compared to this range). The value for f_{new} can change more dramatically for large values of E_{SO2}, but the change was less than ± 0.01 for 78% of the samples tested.

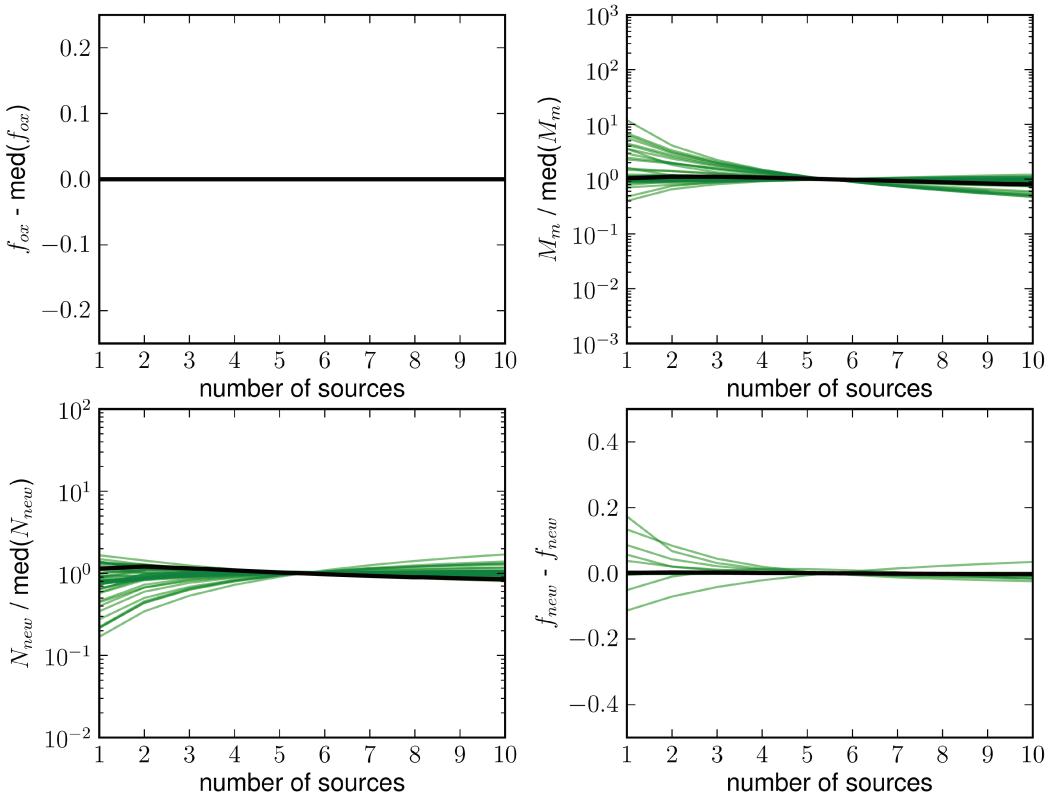

Figure 3.6: Sensitivity of f_{ox}, M_{m}, N_{new}, and f_{new} to the assumed number of emission sources, while keeping total emissions of SO_2 and NO_x constant, for 100 randomly selected sets of inputs. If nucleation is not predicted by the P6 parametrization, no value is shown. The black line in each figure denotes the median value case. In order to highlight the sensitivities to the number of sources assumed, for f_{ox} and f_{new}, the median value of each plotted line is subtracted from the line, and for M_{m} and N_{new}, each plotted line is divided by its median value.

As discussed earlier, we include three different options for specifying SO_2 and NO_x emissions in our included Fortran code of the P6 parameterization. Two of these options involve specifying the total emissions in the grid box and allowing P6 to make assumptions about the size of the sources (Table 3.3). Fortunately, the analysis above shows that the P6 outputs are generally not very sensitive to the number of sources assumed, so the lack of knowledge of individual sources likely will not create large errors in P6 outputs.

3.6 Conclusions

In this study, we describe the Predicting Particles Produced in Power-Plant Plumes (P6) parameterization: a physically based, but computationally efficient, parameterization that predicts the characteristics of aerosol formed in sulphur-rich plumes based on variables that are commonly available in global- and regional-scale models. The parameterization predicts the fraction of the emitted SO_2 that is oxidized to form H_2SO_4, the fraction of that H_2SO_4 that forms new particles, the mean mass per particle of the new particles, and the number of new particles per kg SO_2 emitted. It takes as inputs the source-level SO_2 and NO_x emissions rates, the background aerosol condensation sink, the downward shortwave radiative flux, the mean boundary-layer wind speed, the boundary-layer height, the background SO_2 and NO_x concentrations, and the distance from the source. The increase in running time of a 3D aerosol model due to implementing the P6 parameterization would be negligible because the parameterization consists only of several arithmatic equations.

In order to create a set of training data for the P6 parameterization, we used the SAM-TOMAS LES/CRM model with online aerosol microphysics. We have shown that the results of the parameterization show good agreement with the results of the SAM-TOMAS model and that the P6 parameterization captures the variability in aerosol formation and growth in sulphur-rich plumes, with correlation coefficients ranging from 0.650 for f_{new} to 0.891 for f_{ox}.

While the P6 parameterization reproduces well the behaviour of the SAM-TOMAS model, we note that it inherits the limitations of the SAM-TOMAS model. Aqueous-phase oxidation of SO_2 is not accounted for, and therefore f_{ox} may be underpredicted under cloudy conditions. Nitrous acid (HONO) and sulphur trioxide (SO_3) emission are not accounted for, and these processes may result in particle formation early in the plume. Nucleation rates are parameterized using an empirical fit proportional to H_2SO_4 concentrations. Despite these limitations, the SAM-TOMAS model has been previously shown to well represent the formation and growth of aerosol in coal-fired power-plant plumes (Chapter 2 and Lonsdale et al., 2012). We therefore believe that the P6 parameterization captures well the variability in new-particle formation and

growth within sulphur-rich plumes.

The median value of f_{ox} predicted by the P6 parameterization (0.0098) for the training cases is much less than the fraction of emitted SO_2 mass added as sub-grid sulphate by Adams and Seinfeld (2003) (0.03) or Dentener et al. (2006) (0.025). Additionally, we excluded night-time cases from our training data, where no oxidation of SO_2 and no new-particle formation would be predicted by the P6 parameterization. Consequently, we expect that predictions of total aerosol mass near sulphur-rich point sources using global-scale models implementing the P6 parameterization will be less than those using the Adams and Seinfeld (2003) or Dentener et al. (2006) assumptions. Additionally, as the median values of both N_{new} and M_m predicted by SAM-TOMAS were less than those predicted by Adams and Seinfeld (2003), we expect that both globally averaged aerosol number concentrations and globally averaged CCN concentrations would be less than those using the Adams and Seinfeld (2003) assumption, with large regional differences (e.g. less CCN formation using the P6 parameterization under cloudy, polluted conditions than sunny, low-background-aerosol conditions). It is our intent to perform a complete comparison of the results of a global chemical-transport model with and without the parameterization as a future work.

This parameterization will allow for improved representation of sub-grid formation and growth of sulphate aerosol in global- and regional-scale models, allowing for more accurate predictions of aerosol size distributions and improved confidence in studies of aerosol effects on health and climate.

Chapter 4

The Contribution of Sub-Grid, Plume-Scale Nucleation to Global and Regional Aerosol and CCN Concentrations.

Stevens, R. G. and Pierce, J. R.: The contribution of sub-grid, plume-scale nucleation to global and regional aerosol and CCN concentrations, in preparation for Atmos. Chem. Phys., 2014

4.1 Introduction

In this chapter, we implement the P6 sub-grid sulphate parameterization (Chapter 3) into a global chemical-transport model with online aerosol microphysics. We test the sensitivities of predicted N3, N10, N40, N80 (the number concentration of particles with diameters larger than 3, 10, 40 and 80 nm, respectively) to assumptions about sub-grid sulphate. As the output of the P6 parameterization is expected to be sensitive to pre-existing aerosol due to condensation and coagulation sinks, we investigate the sensitivity of predictions to the global amount of secondary organic aerosol and grid-resolved nucleation scheme. We also investigate the sensitivity of N80 enhancement to sub-grid sulphate to greater emissions of SO_2 and NO_x to better understand the effects of pollution controls on CCN concentrations.

In Sect. 4.2, we describe the GEOS-Chem-TOMAS model specifications and we describe the simulations performed for this study. In Sect. 4.3 we discuss the sensitivities of our results to the treatment of sub-grid sulphate, and how these interact with additional secondary organic aerosol emissions and grid-resolved nucleation scheme. In Sect. 4.4 we present the results of an adjoint to the P6 parameterization, and discuss the sensitivity of our results to the inputs of P6. In Sect. 4.5 we discuss the sensitivities to SO_2 and NO_x emissions. In Sect. 4.6 we compare the results of our simulations with surface-based N10, N40, N80, and N150 measurements. Finally, we present our conclusions in Sect. 4.7.

4.2 Model Specifications and Descriptions of Simulations

For this study, we implemented the P6 sub-grid sulphate parameterization into the GEOS-Chem-TOMAS model. GEOS-Chem-TOMAS uses the TwO Moment Aerosol Sectional (TOMAS) microphysics algorithm (Adams and Seinfeld, 2002; Pierce and Adams, 2009) in the GEOS-Chem v9-02 chemical transport model (`http://geos-chem.org`, Bey et al., 2001). The implementation of TOMAS in GEOS-Chem has been discussed previously (Pierce et al., 2013; Snow-Kropla et al., 2011; Trivitayanurak et al., 2008). The TOMAS module resolves aerosol by both mass and number independently. For this study, the aerosol was simulated using 15 size bins spanning 3 nm to 10 μm (Lee and Adams, 2012). Condensation, coagulation, and nucleation are explicitly resolved in the model. The model was run at 4° latitude by 5° longitude resolution with 47 vertical layers from the surface to 0.01 hPa and with meteorological inputs from the GEOS5 re-analysis (`http://gmao.gsfc.nasa.gov`).

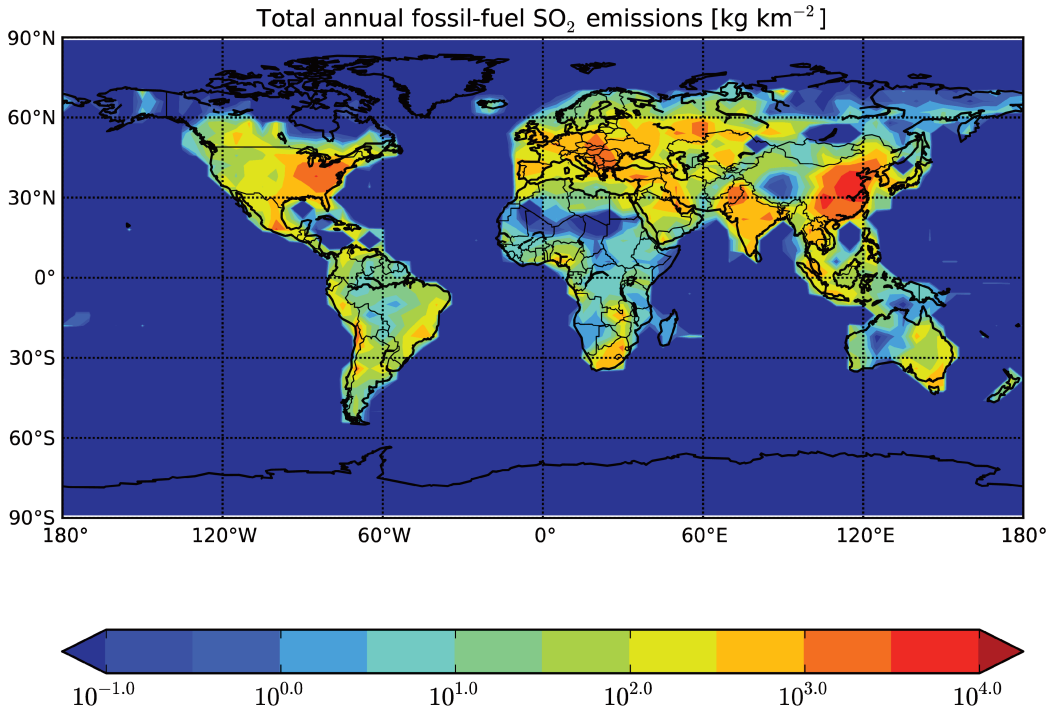

Figure 4.1: Total annual fossil-fuel SO_2 emissions used for this study, excluding shipping emissions.

Anthropogenic emissions in GEOS-Chem are provided by the Emissions Database for Global Atmospheric Research (EDGAR) inventory (Olivier et al., 1996), except where it overwritten by the following regional inventories: The Environmental Protection Agency 2005 National Emissions Inventory (NEI05) (http://www.epa.gov/ttn/chief/net/2005inventory.html) over the United States, the Criteria Air Contaminants (CAC) for anthropogenic emissions over Canada (http://www.ec.gc.ca/inrp-npri/), the Big Bend Regional Aerosol and Visibility Study (BRAVO) emissions inventory over Mexico and the southwestern United States (Kuhns et al., 2001), the Streets inventory for Asian emissions (Streets et al., 2003) over Asia, and the Cooperative Programme for Monitoring and Evaluation of the Long-Range Transmission of Air Pollutants in Europe (EMEP) over Europe (Auvray and Bey, 2005). The total annual fossil-fuel SO_2 emissions, not including shipping emissions, from these inventories is shown in Fig. 4.1 for the simulated year, 2005. Biogenic emissions were from the Model of Emissions of Gases and Aerosols from Nature (MEGAN) (Guenther et al., 2006), except for an additional secondary organic aerosol (SOA) source in some simulations that we will describe below. Biomass burning emissions were from the Global Fire Emissions Database version 3 (GFEDv3) (van der Werf et al., 2010).

The P6 parameterization predicts characteristics of sub-grid sulphate formed in sulphur-rich plumes based on variables commonly available in global- and regional-scale models. A full description is available in Chapter 3. Specifically, the parameterization predicts the fraction of SO_2 oxidized to form H_2SO_4 (f_{ox}), the fraction of the H_2SO_4 that forms new particles (f_{new}), the number of new particles formed per kg SO_2 emitted (N_{new}), and the median diameter of the newly formed particles (D_{m}). The parameterization takes as inputs the emissions of SO_2 (E_{SO2}) and NO_x (E_{NOx}) from the power-plant, the pre-existing aerosol condensation sink (CS), the downward shortwave radiative flux ($DSWRF$), the mean boundary-layer wind speed (v_{g}), the boundary-layer height (BLH), the distance from the source (d), and the background concentrations of SO_2 ($bgSO_2$) and NO_x ($bgNO_{\mathrm{x}}$).

The P6 parameterization is based upon the results of the System for Atmospheric

Modelling (Khairoutdinov and Randall, 2003) with the TOMAS microphysics module described above, thus P6 inherits limitations of SAM-TOMAS model. It does not account for new-particle formation that may be occurring within power-plant stacks or immediately after emission, due to possible direct emissions of sulphur trioxide (SO_3) or nitrous acid (HONO). The P6 parameterization also does not account for aqueous-phase oxidation of SO_2 or in-cloud aerosol processing. This missing oxidation pathway would lead to an underestimation of the fraction of SO_2 oxidized, but we do not expect this to strongly affect predictions of aerosol number because little new-particle formation would be predicted under cloudy conditions because of the suppression of sunlight, which in turn would lead to lower OH concentrations and lower H_2SO_4 concentrations (Chapter 2). Finally, condensational growth due to SOA within sulphur-rich plumes is not accounted for, which we will discuss further in Sect. 4.3. Despite these limitations, the SAM-TOMAS model has been shown to predict well the number and size of aerosol formed in coal-fired power plant plumes (Chapter 2 and Lonsdale et al., 2012). We therefore expect that the P6 parameterization well represents the variability in new-particle formation and growth rates within sulphur-rich plumes.

Because the emissions inventories used by GEOS-Chem do not provide source-specific emissions, but instead emissions summed across a 1° x 1° grid, the distance downwind from the source is not calculable. We therefore use a length scale equal to half of the square root of the grid cell horizontal area, as suggested in Appendix B, for the distance from the source (d) required for P6. In GEOS-Chem-TOMAS, the value of boundary-layer height (BLH) used as input to P6 is based on BLH values from the GEOS-5 reanalysis. We note that the BLH values from the GEOS-5 reanalysis were found to be unrealistically low under night-time conditions, and thus the boundary-layer heights within GEOS-Chem-TOMAS used as input to P6 have been adjusted from the original GEOS-5 reanalysis values by limiting them to a minimum of the mechanical mixing depth, which is calculated based on the local friction velocity (Heald et al., 2012; Walker et al., 2012). We also note that the BLH values were defined within the GEOS-5 dataset as the height where the diffusivity falls below a critical value (Rienecker, 2006). The BLH values used to create the P6 parameterization

came from the North American Regional Reanalysis dataset, where they were defined as the height where the turbulent kinetic energy falls below a critical value (Mesinger et al., 2006), and these values may differ due to the different definitions. However, of the nine inputs to the P6 parameterization, the BLH is the input to which all outputs of P6 have the weakest sensitivity. We therefore do not expect that uncertainties in BLH values will have a large impact on our results. We also make the following assumption about the sizes of individual sources, as recommended in Chapter 3: We assume that within each model grid cell, the SO_2 emissions are split between an equal number of low emitters, medium emitters, and high emitters. We define high emitters, medium emitters, and low emitters based on the emissions data for power-plants in the United States compiled from the Clean Air Markets (CAM) data (United States Environmental Protection Agency, 2012) as follows: For medium emitters, we use the log-space mean emission rates for a power plant in the USA during 2010. For low and high emitters, we use an emission rate that is one standard deviation below or above the mean in log space, respectively. The low, medium, and high emission rates of SO_2 are 0.0606 kg s^{-1}, 0.202 kg s^{-1}, and 1.00 kg s^{-1}, respectively. We further assume that the low, medium, and high emitters emit 0.0300 kg N s^{-1}, 0.0840 kg N s^{-1}, and 0.290 kg N s^{-1} of NO_x, derived in the same way from the 2010 EPA CAM NO_x emissions data.

We performed 19 simulations with GEOS-Chem-TOMAS, summarized in Table 4.1. All simulations were performed with meteorology and emissions for the year 2005. Simulations labelled NoSGS did not include any sub-grid sulphate emissions. Simulations labelled AS3 emitted 3% of anthropogenic SO_2 as sub-grid sulphate, using the bi-modal size distribution described in Adams and Seinfeld (2003) comprised of a nucleation mode containing 15% of the emitted sulphate mass with a 10 nm number mean diameter and a geometric standard deviation of 1.6; and an Aitken mode containing the rest of the sulphate mass with a 70 nm number mean diameter and a geometric standard deviation of 2.0. Simulations labelled LY5 emitted 5% of anthropogenic SO_2 as sub-grid sulphate, emitting 5% of the sulphate into the same nucleation mode as AS3, but the remaining sulphate was condensed onto pre-existing aerosol, as was done for one of the simulations described in Luo and Yu (2011).

Table 4.1: Summary of GEOS-Chem-TOMAS simulations performed. The different sub-grid sulphate schemes and nucleation schemes are described in Sect. 4.2. Extra SOA refers to emissions of 100 Tg yr^{-1} of SOA, co-located with emissions of CO.

Name	Sub-grid sulphate	Extra SOA	Boundary-layer nucleation	Changes to emissions
NoSGS_yXSOA_Napa	none	on	Ternary	-
NoSGS_yXSOA_Act	none	on	Activation	-
NoSGS_nXSOA_Napa	none	off	Ternary	-
NoSGS_nXSOA_Act	none	off	Activation	-
AS3_yXSOA_Napa	AS3	on	Ternary	-
AS3_yXSOA_Act	AS3	on	Activation	-
AS3_nXSOA_Napa	AS3	off	Ternary	-
AS3_nXSOA_Act	AS3	off	Activation	-
LY5_yXSOA_Napa	LY5	on	Ternary	-
LY5_yXSOA_Act	LY5	on	Activation	-
LY5_nXSOA_Napa	LY5	off	Ternary	-
LY5_nXSOA_Act	LY5	off	Activation	-
P6_yXSOA_Napa	P6	on	Ternary	-
P6_yXSOA_Act	P6	on	Activation	-
P6_nXSOA_Napa	P6	off	Ternary	-
P6_nXSOA_Act	P6	off	Activation	-
P6_hiSO2	P6 ($E_{SO2} \cdot 1.5$)	off	Ternary	$SO_2 \cdot 1.5$
P6_hiNOx	P6 ($E_{NOx} \cdot 1.5$)	off	Ternary	$NO_x \cdot 1.5$
P6_hiboth	P6 ($E_{SO2} \cdot 1.5$ and $E_{NOx} \cdot 1.5$)	off	Ternary	$SO_2 \cdot 1.5$ and $NO_x \cdot 1.5$

Simulations labelled P6 used the P6 parameterization to predict the fraction of anthropogenic SO_2 to emit as sub-grid sulphate, as well as the fraction of the emitted sulphate to emit as particles or condense onto pre-existing particles, and the size of the emitted particles. The amount of sub-grid sulphate emitted and the size of the particles emitted therefore varied with each time step and with each model grid cell in simulations labelled P6.

Secondary organic aerosol (SOA) production in TOMAS is calculated as 10% of global monoterpene emissions (based on MEGAN, (Guenther et al., 2006)), resulting in approximately 19 Tg yr^{-1} of SOA. However, the study of Spracklen et al. (2011) suggested that including emissions of an additional 100 Tg yr^{-1} of SOA co-located with anthropogenic pollution yields much better agreement of organic aerosol mass

with Aerosol-Mass-Spectrometer-based observations. This additional source of "anthropogenically controlled" SOA has been implemented into GEOS-Chem-TOMAS previously (D'Andrea et al., 2013), where it was also found to provide much better agreement with size distribution observations. This SOA is condensed irreversibly to the Fuchs-corrected aerosol surface area as this was shown to give the best agreement with size distributions in D'Andrea et al. (2013). Simulations labelled 'yXSOA' therefore contain additional emissions of 100 Tg yr^{-1} of SOA correlated with anthropogenic CO emissions. Simulations labelled 'nXSOA' do not contain these additional emissions. One limitation of our yXSOA simulations is that the extra SOA does not aid in the sub-grid nucleation and growth as the P6 scheme does not handle sub-grid growth from SOA. The implications of this will be discussed in the results section.

Binary (H_2SO_4 + H_2O) nucleation rates were predicted in all simulations by the classical binary nucleation scheme described by Vehkamäki et al. (2002). In addition to binary nucleation, ternary (H_2SO_4 + NH_3 + H_2O) nucleation was predicted in simulations labelled 'Napa' by the parameterization of ternary homogeneous nucleation of sulphuric acid, ammonia and water described by Napari et al. (2002) scaled down globally by a constant factor of 10^5 which has been shown to predict nucleation rates closer to measurements than other commonly used nucleation schemes (Jung et al., 2010; Westervelt et al., 2013, 2014). Within simulations labelled 'Act', nucleation in the boundary layer was predicted using activation-type nucleation, and ternary nucleation was shut off (binary nucleation was left on). The nucleation rate in activation-type nucleation simulations was a linear function of sulphuric acid concentration, according to the following equation (Kulmala et al., 2006; Sihto et al., 2006):

$$J = 2 \cdot 10^{-6}[H_2SO_4] \tag{4.1}$$

where J is the nucleation rate and the units of the prefactor are s^{-1}.

Lonsdale et al. (2012) showed that the emissions rate of SO_2 from US coal-fired power plants was, on average, 56% greater in 1997 than in 2010, and that the emissions rate of NO_x was 108% greater in 1997 than 2010. These decreases were achieved primarily through the implementation of pollution-control technologies or switching

to coal with lower sulphur contents. In order to assess the potential effect of such pollution controls on sub-grid sulphate formation, we performed three additional simulations with nucleation and SOA assumptions the same as the P6_nXSOA_Napa simulation. Simulation P6_hiSO2 differs from the P6_nXSOA_Napa simulation only in that both the assumed SO_2 emissions used as input to P6 and the modelled fossil-fuel emissions of SO_2 (excluding those from shipping) are increased globally by 50%. We note that actual SO_2 emissions have not decreased globally, and thus the SO_2 emissions in this simulation are not meant to represent any previous year but rather a general sensitivity to these emissions. Similarly, in simulation P6_hiNOx, both the assumed emissions of NO_x used as input to P6 and the modelled fossil-fuel NO_x emissions are increased globally by 50%. We note that NO_x pollution controls have not been implemented globally, and that fossil-fuel NO_x emissions include other sources than coal-fired power plants, such as vehicular exhaust. However, the available inventories for anthropogenic NO_x do not separate coal-fired power plants from other anthropogenic sources, and it is beyond the scope of this paper to estimate what proportion of anthropogenic NO_x emissions are due to coal-fired power-plant emissions. Thus the NO_x emissions in simulation P6_hiNOx are not representative of any past year, and again are for general sensitivity purposes only. Simulation P6_hiboth includes increased emissions of SO_2 used as input to P6 and increased emissions of fossil-fuel SO_2 by 50%, as well as increased assumed NO_x emissions used as input to P6 and increased fossil-fuel NO_x emissions by 50%.

4.3 Sensitivity to Sub-Grid Sulphate Scheme.

We present in Table 4.2 the globally and annually averaged changes in boundary-layer N3, N10, N40 and N80 for each simulation, excluding the emissions sensitivity studies, from the corresponding simulation with no sub-grid sulphate that had the same amount of SOA emissions and the same grid-resolved nucleation scheme.

The simulations with AS3 sub-grid sulphate have decreases in N3, but increases in N10, N40, and N80 (Table 4.2). As the median diameter of the AS3 nucleation mode

Table 4.2: Globally, annually averaged changes in N3, N10, N40 and N80 attributable to sub-grid sulphate emissions. Each simulation is compared to the NoSGS case with the same SOA emissions and the same grid-resolved nucleation scheme.

Simulation	% change in N3	% change in N10	% change in N40	% change in N80
AS3_yXSOA_Napa	-0.36	+8.93	+11.67	+9.73
AS3_yXSOA_Act	-0.50	+4.40	+9.90	+8.43
AS3_nXSOA_Napa	-3.71	+4.44	+5.32	+4.94
AS3_nXSOA_Act	-1.41	+3.17	+4.52	+4.07
LY5_yXSOA_Napa	+5.21	+24.17	+25.17	+19.72
LY5_yXSOA_Act	+1.05	+13.86	+23.72	+19.11
LY5_nXSOA_Napa	-9.51	+3.91	+11.27	+10.78
LY5_nXSOA_Act	-3.48	+4.48	+11.90	+10.56
P6_yXSOA_Napa	-13.57	-9.09	-3.72	-0.86
P6_yXSOA_Act	-2.69	-2.83	-0.45	+1.32
P6_nXSOA_Napa	-18.34	-12.97	+0.32	+3.46
P6_nXSOA_Act	-5.86	-4.87	+3.80	+5.71

is 10 nm, the added particles are sufficiently large to provide an additional coagulation sink for the smallest particles resolved by GEOS-Chem-TOMAS, and increased competition for H_2SO_4, which somewhat suppresses new-particle formation. These feedbacks result in a decrease in the number of particles smaller than 10 nm, but increases in particle number concentrations at larger sizes.

In Fig. 4.2 we show the annually averaged changes in boundary-layer N80 between the four AS3 simulations and the corresponding simulations with no sub-grid sulphate. Regardless of SOA amount and grid-resolved nucleation scheme, the inclusion of AS3 sub-grid sulphate increases N80 over industrialized regions. However, the two simulations that include anthropogenically controlled SOA (yXSOA, panels a and c) show a greater increase in N80, especially over the northern hemisphere. In these simulations, the newly formed sub-grid sulphate particles grow more quickly due to the condensation of the additional SOA mass, and a greater fraction grow larger than 80 nm. This is consistent with the findings of D'Andrea et al. (2013), where including an additional 100 Tg yr^{-1} of SOA was found to increase globally and annually averaged boundary-layer N80 by 29.9%. The increased survivability of the sub-grid sulphate particles can also be seen in the N3, N10 and N40 changes

(Table 4.2). The two AS3 simulations with anthropogenically controlled SOA show smaller decreases in N3 and larger increases in N10 and N40 from the corresponding no sub-grid sulphate cases than the AS3 simulations without this extra source of SOA.

The two AS3 simulations with ternary nucleation (Napa) show a much greater increase in N80 over north-western South America and the Malay Archipelago. In these regions, little ammonia is present, so less nucleation is predicted by the ternary nucleation scheme than the activation nucleation scheme. Thus, when no sub-grid sulphate is included, the simulations with activation-type nucleation (Act) have higher N80 in these regions than the simulations with ternary nucleation, and so the addition of a fixed amount of sub-grid sulphate causes a smaller relative change in N80 for the activation-type nucleation simulations than the ternary nucleation simulations in these regions.

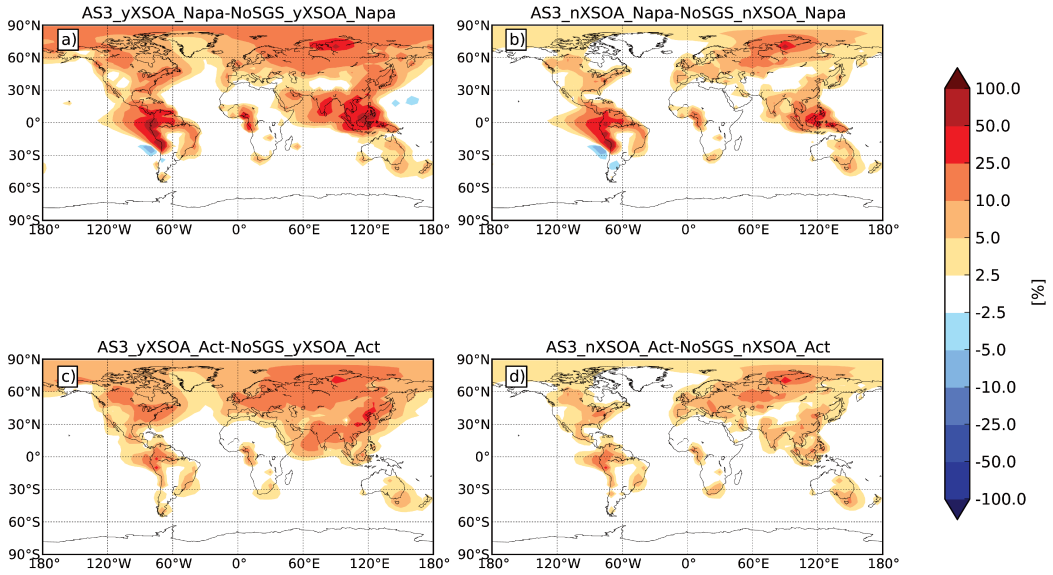

Figure 4.2: Change in annually averaged boundary-layer N80 between the AS3 sub-grid sulphate simulations and the simulations with no sub-grid sulphate. Top row (a, b): Napari ternary grid-resolved nucleation. Bottom row (c, d): activation-type grid-resolved nucleation. Left column (a, c): with anthropogenically-controlled SOA. Right column (b, d): without anthropogenically-controlled SOA.

The changes in N80 between simulations with LY5 sub-grid sulphate and the

corresponding simulations with no sub-grid sulphate (not shown) are similarly distributed spatially to those from the AS3 simulations, but greater in magnitude (see Table 4.2). The effects of changing SOA amount and grid-resolved nucleation scheme are also similar for the LY5 simulations. The increase in the magnitude of the changes in N80 for the LY5 simulations relative to the AS3 simulaitons is in part due to the increased fraction of SO_2 that is assumed to be oxidized on the sub-grid scale (5% for LY5, compared to 3% for AS3). In addition, while both AS3 and LY5 sub-grid sulphate use the same size distribution for nucleation mode particles, the remaining sulphate mass is emitted as Aitken-mode particles in AS3, whereas the remaining mass is condensed onto pre-existing particles in LY5. In the LY5 simulations, particles emitted into the nucleation mode in one model time step will be grow by sub-grid condensation during following time steps, and this will speed their growth to CCN sizes. In contrast, the Aitken-mode particles emitted in simulations using the AS3 sub-grid sulphate scheme will remove nucleation-mode particles in subsequent time steps through coagulation. Because of these effects, the LY5 scheme more efficiently produces CCN-sized particles.

We note that the LY5 simulations with anthropogenically controlled SOA are the only simulations that show an increase in N3 compared to the simulations without sub-grid sulphate (Table 4.2). As the nucleation-mode sub-grid sulphate is still being emitted with median diameter 10 nm, as in the AS3 simulations, one would expect a decrease in the number of sub-10 nm particles, as was seen for the AS3 simulations. Through inspection of globally averaged size distributions (not shown), we have determined that the number of sub-10 nm particles decreases in these simulations as well, but the increases in N10 are sufficiently large to more than compensate for these decreases, resulting in a net increase in N3.

Figure 4.3 shows the annually averaged change in N80 between the four P6 simulations and the corresponding simulations without sub-grid sulphate. In contrast to the AS3 and LY5 simulations, the enhancement in N80 due to sub-grid sulphate for the P6 simulations is less for the simulations where anthropogenically controlled SOA is included (yXSOA, panels a and c) than for the two simulations without this

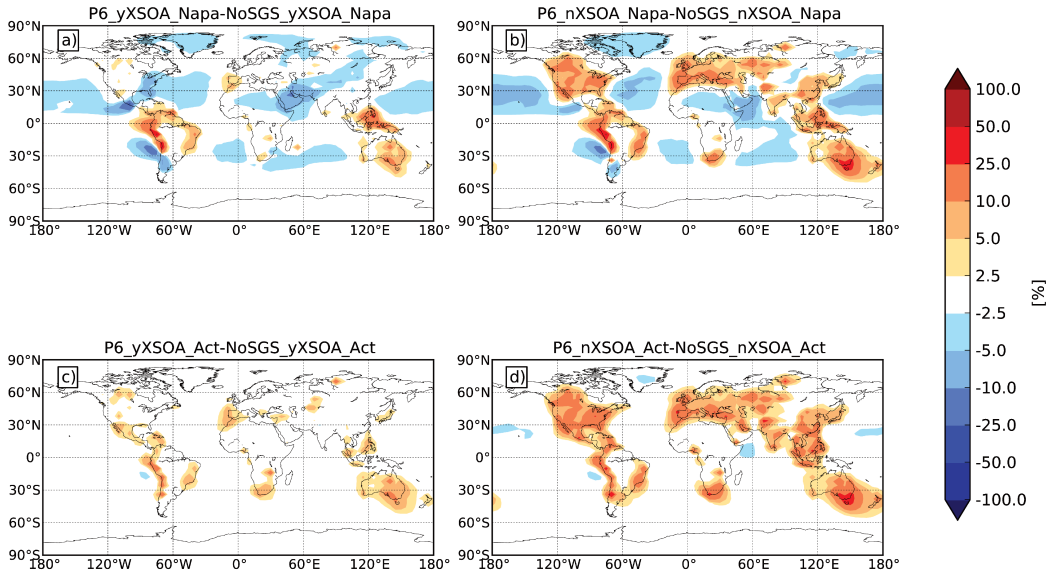

Figure 4.3: Change in annually averaged boundary-layer N80 between the P6 sub-grid sulphate simulations and the simulations with no sub-grid sulphate. Top row (a, b): Napari ternary grid-resolved nucleation. Bottom row (c, d): activation-type grid-resolved nucleation. Left column (a, c): with anthropogenically-controlled SOA. Right column (b, d): without anthropogenically-controlled SOA.

extra source of SOA (nXSOA, panels b and d). Notably, in the simulations with anthropogenically controlled SOA and ternary nucleation, globally, annually averaged N80 is less when using P6 sub-grid sulphate than with no sub-grid sulphate (P6_yXSOA_Napa vs. NoSGS_yXSOA_Napa), as shown in Fig. 4.3a and listed in Table 4.2. We will show in the following section that the additional SOA increases the pre-existing condensation sink, which in turn causes P6 to predict much less sub-grid new-particle formation and growth. However, higher concentrations of SOA would be expected to condense onto newly formed particles at the sub-grid scale as well as at the grid-resolved scale, which would increase the growth and survivability of the newly formed particles. It has been shown that SOA may preferentially form within anthropogenic plumes (Carlton et al., 2009, 2010; D'Andrea et al., 2013; Heald et al., 2011; Offenberg et al., 2009; Spracklen et al., 2011; Surratt et al., 2007), which may imply that SOA preferentially condenses onto particles within sulphur-rich plumes, compared to particles outside of such plumes. These processes would compensate somewhat for suppression of new-particle formation by the enhanced background condensation sink but are not currently accounted for by the P6 parameterization.

It is therefore possible that sub-grid new-particle formation and growth is underpredicted by the P6 parameterization for the cases with anthropogenically controlled SOA.

In Fig. 4.3a and Fig. 4.3b a decrease in N80 is shown over the oceanic regions downwind of polluted regions. This decrease occurs for the two ternary nucleation cases (Napa), but not for the activation-type nucleation cases (Act). The sub-grid condensation of H_2SO_4 in all P6 cases increases the coagulation sink downwind of polluted regions, and the larger particles are more efficiently removed by wet deposition. In the activation-type nucleation simulations, nucleation and growth over the oceanic regions dampens this decrease in N80, but the Napari ternary nucleation scheme predicts little new-particle formation over ocean regions, and the regions of decreased N80 persist. These decreases are even more strongly pronounced for smaller particles, and this effect is responsible for the more negative values of the changes in N3, N10, and N40 in the P6 Napa simulations than the P6 Act simulations shown in Table 4.2.

When anthropogenically controlled SOA is included, the P6 cases show much smaller annually averaged increases in N80 than the AS3 and LY5 cases, particularly in the northern hemisphere (see Table 4.2 and compare Fig. 4.2, panels a and c with Fig. 4.3, panels a and c). As mentioned above, the P6 parameterization may be underestimating sub-grid new-particle formation and growth in these cases because it does not include any enhancement of new-particle formation and growth by SOA within the sub-gid plumes. Without this source of SOA, the P6 cases show similar globally, annually averaged increases in N80 to the AS3 cases, which are roughly half those of the LY5 cases (Table 4.2). The increases in N80 are distributed somewhat differently in P6 than AS3 and LY5, however (compare Fig. 4.2, panels b and d with Fig. 4.3, panels b and d). The P6 cases show little increase in N80 over the Arctic compared to the AS3 and LY5 cases because less sunlight is available at such high latitudes for OH formation and subsequent oxidation of SO_2. Compared to the AS3 cases, this is compensated by increased N80 over eastern North America, South Africa, southeast Australia, Portugal and Spain. The P6 parameterization tends to predict more new-particle formation and growth over these regions due to the relatively greater

sunlight and lower condensation sink in these regions (shown in next section). The assumption that the amount and size of sub-grid sulphate formed is constant (e.g. AS3 and LY5) may therefore be unable to resolve important regional differences in sub-grid new-particle formation and growth.

4.4 The P6 Adjoint, and Sensitivities to P6 Inputs.

In order to better understand the results of P6 simulations, including differences bewtween P6 simulations due to SOA amount and emissions, and differences in the P6 simulations from AS3 and LY5 simulations, we have created an adjoint to the P6 parameterization. This adjoint allows us to quickly test the sensitivity of the P6 outputs (fraction of emitted SO_2 oxidized to form H_2SO_4 (f_{ox}), fraction of that H_2SO_4 that forms new particles (f_{new}), median diameter of newly formed particles (D_m), and number of newly formed particles per kg SO_2 emitted (N_{new})) to changes in each of the P6 inputs (emissions of SO_2 (E_{SO2}) and NO_x (E_{NOx}) from the source, background condensation sink of pre-existing particles (CS), downward shortwave radiative flux ($DSWRF$), mean boundary-layer wind speed (v_g), boundary-layer height (BLH), distance from the source (d), and mean background concentrations of SO_2 ($bgSO_2$) and NO_x ($bgNO_x$)). We can use the adjoint to calculate the derivative of each of the outputs of P6 with respect to each of the inputs of P6 for a given set of inputs. We have run the P6 adjoint offline using the monthly-mean values of each of the P6 inputs as output by GEOS-Chem-TOMAS. (While the values from the P6 adjoint calculated based on monthly means of the P6 inputs will not be equal to monthly-means of values calculated based on the instantaneous values of the P6 inputs due to non-linearities in the equations, we do not expect that the differences due to these non-linearities would qualitatively alter any of our analysis below.) We discuss below the results of the adjoint of simulation P6_nXSOA_Napa. We choose P6_nXSOA_Napa for this discussion because, as noted above, the P6 parameterization does not currently include the effects of anthropogenically controlled SOA on sub-grid new-particle formation and growth, and because the scaled Napari ternary nucleation scheme has been shown to yield results that compare more favourably with observations (Westervelt et al., 2013).

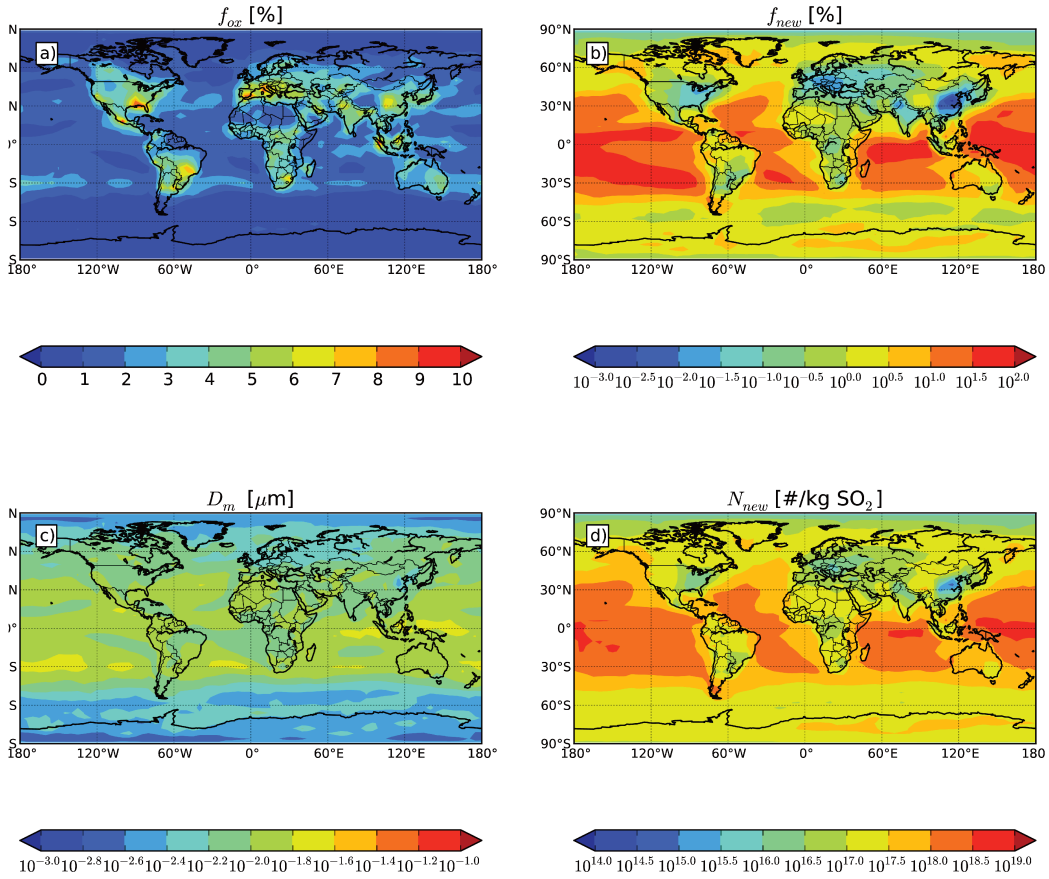

Figure 4.4: Annually averaged outputs of the P6 parameterization, as calculated offline from monthly-means of the P6 inputs for simulation P6_nXSOA_Napa: a) fraction of emitted SO_2 oxidized (f_{ox}), b) fraction of H_2SO_4 formed that comprises new particles (f_{new}), c) median diameter of emitted particle (D_{m}), and d) number of new particles per kg SO_2 emitted (N_{new}). We note these values are calculable even in the absence of emissions, see Sect. 4.4.

We show in Fig. 4.4 the annually averaged values of each of the P6 outputs, as calculated offline by the adjoint for simulation P6_nXSOA_Napa. (We note that because emissions rates are assumed [e.g. high emitters, medium emitters and low emitters, see Sect. 4.2] for the purposes of calculating the P6 outputs, we can calculate these outputs even where there are no emissions, such as over oceans. However, since the amount of sub-grid sulphate to be emitted is expressed as a fraction of SO_2 emissions (f_{ox}), no sub-grid sulphate will be emitted in the absence of SO_2 emissions.) In Fig. 4.5 we show the annually averaged sensitivity of N_{new} to each of the P6 inputs

for simulation P6_nXSOA_Napa, as the percentage change in N_{new} for a percentage change in the input. For each latitude and longitude point, we exclude months where no nucleation would be predicted based on the monthly mean of the P6 inputs, as the sensitivity of N_{new} to a change in the P6 inputs is ill-defined for no-nucleation cases.

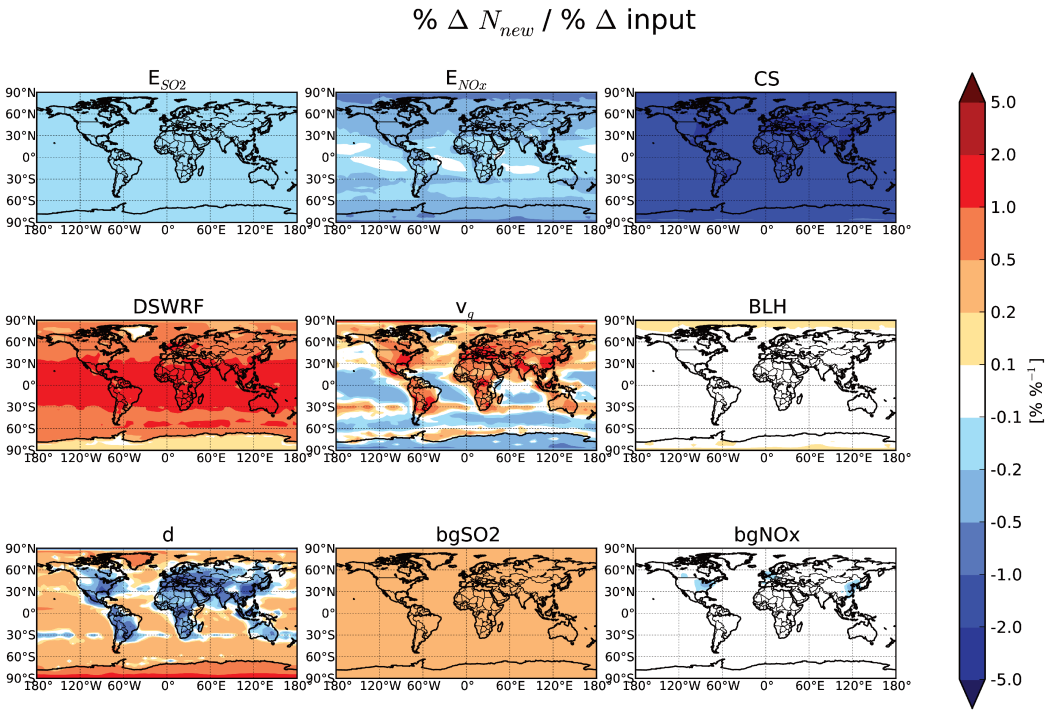

Figure 4.5: Annually averaged sensitivity of N_{new} to each of the inputs to P6 for simulation P6_yXSOA_Napa, given as the percentage change in the value of N_{new} for a percentage change in the value of the input.

As shown in Fig. 4.4a, over high-pollution regions, the f_{ox} values calculated offline are generally between 5% and 8%. This is slightly higher than the 3% and 5% values assumed by AS3 and LY5, respectively, and also note that the P6 scheme does not account for aqueous-phase oxidation. The value of f_{ox} is higher in high-pollution regions, as the background NO_x concentrations in these regions are closer to those optimal for OH production, and hence SO_2 oxidation. The value of f_{ox} is commonly lower than 4% in rural regions, and can fall to less than 1% in very remote regions. In contrast f_{new} is much lower over polluted regions, with values less than 0.1% over the eastern US, Europe, and less than 0.01% over China. For the LY5 sub-grid sulphate

scheme, the value of f_{new} is assumed to be 5% everywhere. The AS3 sub-grid sulphate scheme emits 15% of sulphate into the nucleation mode, and while this is not directly comparable to f_{new} in the P6 scheme as the remaining sulphate is emitted into the Aitken mode and not condensed onto pre-existing particles, both the AS3 and LY5 schemes assume a far greater proportion of sub-grid sulphate forms new particles than is predicted by the P6 parameterization over high-pollution regions. As a much smaller fraction of sub-grid sulphate forms new particles in the simulations using the P6 scheme, there are many fewer particles available to grow to CCN sizes, and hence generally a smaller change in N80 from the simulations without sub-grid sulphate. For the P6 case with anthropogenically controlled SOA and ternary nucleation (P6_yXSOA_Napa), the growth of pre-existing particles by this sub-grid condensation allows them to more effectively remove particles through coagulation resulting in a decrease in N80 from the corresponding case with no sub-grid sulphate (NoSGS_yXSOA_Napa).

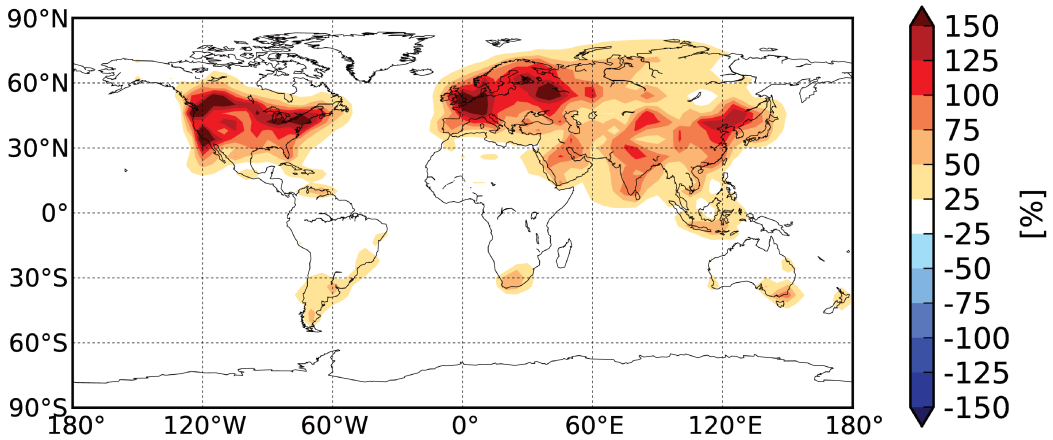

Figure 4.6: Change in annually averaged condensation sink due to anthropogenically-controlled SOA (simulations included no sub-grid sulphate and used Napari ternary grid-resolved nucleation).

We note that N_{new} and f_{new} are very sensitive to the condensation sink (CS). Over the eastern United States, Europe, India and China, a 1% increase in CS yields a decrease in the predicted values of N_{new} and f_{new} of more than 2% (Fig 4.5 for N_{new}). We show in Fig. 4.6 the difference in CS between simulations NoSGS_yXSOA_Napa

and NoSGS_nXSOA_Napa, to show the change in CS due to the extra SOA. Figure 4.6 shows that inclusion of the anthropogenically controlled SOA increases CS by more than 75% over most of the continental northern hemisphere, and increases CS by more than 100% over most of North America and Europe. We would therefore expect much lower values of N_{new} and f_{new} in these regions. The decrease in N_{new} would result in a lower number of new particles that could potentially grow to CCN sizes. A much greater fraction of the sub-grid-oxidized SO_2 would also be expected to condense onto pre-existing particles, further increasing the condensation sink and suppressing further new-particle formation, both at the grid-resolved scale and the sub-grid scale. Together, these processes are responsible for a drastic reduction in the number of sub-grid sulphate particles that may grow to CCN sizes when anthropogenically controlled SOA is included. However, as noted in the previous section, anthropogenically controlled SOA would be expected to condense onto newly formed particles at the sub-grid scale, but sub-grid condensation of SOA is not currently resolved by P6. Since anthropogenically controlled SOA may preferentially form within coal-fired power-plant plumes, it is likely that the enhanced growth of newly formed particles by this SOA would offset to some extent the suppression of new-particle formation and growth shown by our results.

4.5 Effects of Pollution Controls

As described in Sect. 4.2, we performed additional simulations in order to test the effects of pollution controls upon our results. The simulations P6_hiSO2, P6_hiNOx, and P6_hiboth differ from P6_nXSOA_Napa only in that the emissions of SO_2, NO_x, or both SO_2 and NO_x have been increased by 50%. Emissions of sub-grid sulphate in the P6 sub-grid sulphate scheme (and both other sub-grid sulphate schemes used in this study) are normalized by the modelled emissions of SO_2. Thus, the emissions of sub-grid sulphate would be increased by 50% in the P6_hiSO2 and P6_hiboth simulations if the P6 outputs remained constant. The differences in globally, annually averaged N3, N10, N40, and N80 between the P6_hiSO2, P6_hiNOx, and P6_hiboth simulations and the P6_nXSOA_Napa simulation are shown in Table 4.3, and the

annually averaged differences are shown in Fig. 4.7. The globally, annually averaged N80 in simulations P6_hiSO2, P6_hiP6NOx, and P6_hiP6both increase from the P6_nXSOA_Napa simulation by 9.00%, 1.47%, and 10.24%, respectively. The increase in SO_2 emissions provides an increase in new-particle formation and growth through the additional source of sulphate, at both the grid-resolved and sub-grid scales. The increased NO_x concentrations in the P6_hiNOx and P6_hiboth simulations allow for greater OH production and faster oxidation of SO_2, at both the grid-resolved and sub-grid scales, except in the most polluted regions.

Table 4.3: Globally, annually averaged changes in N3, N10, N40 and N80 due to 50% increases in emissions from the P6_nXSOA_Napa simulation.

Simulation	% change in N3	% change in N10	% change in N40	% change in N80
P6_hiSO2	-8.18	-0.68	+7.35	+9.00
P6_hiNOx	+0.61	+2.04	+2.22	+1.47
P6_hiboth	-8.14	+0.80	+9.26	+10.24

The increases in the assumed emissions of SO_2 (E_{SO2}) and NO_x (E_{NOx}) used as input to P6 will alter the values of the P6 outputs, and thus the number and size of sub-grid sulphate formed in the emissions sensitivity simulations. As the background concentrations of SO_2 ($bgSO_2$) and NO_x ($bgNO_x$) will be increased in the P6_hiSO2 and P6_hiNOx simulations, respectively, there will also be differences in the P6 outputs due to differences in $bgSO_2$ and $bgNO_x$. Additionally, changes in sulphate formation and growth (at both the grid-resolved and sub-grid scales) will result in changes to the grid-resolved aerosol condensation sink (CS), which will also influence the P6 outputs. We have used the adjoint to estimate the differences in the annually averaged P6 outputs between the P6_hiSO2, P6_hiNOx, and P6_hiboth simulations, and the P6_nXSOA_Napa simulation (Fig. 4.8). The fraction of SO_2 oxidized (f_{ox}) in the P6_hiSO2 simulation does not significantly differ from that of the P6_nXSOA_Napa simulation (Fig. 4.8a), as f_{ox} is not sensitive to E_{SO2}, $bgSO_2$, or CS. The number of new particles formed per kg SO_2 emitted (N_{new}) in P6_hiSO2 generally decreases by 20%-30% over polluted regions (Fig. 4.8b) due to an increase in the condensation sink. However, since N_{new} is normalized by SO_2 emissions, which

are increased by 50% in this simulation, there would still be a net increase in the number of sub-grid sulphate particles formed. In order to demonstrate the net change in the number of sub-grid particles formed, including the increases due to increased SO_2 emissions, we plot the relative difference between N_{new}·1.5 from the P6_hiSO2 and P6_hiboth simulations and the value of $N_{\rm new}$ in the P6_nXSOA_Napa simulation in Fig. 4.9. In simulation P6_hiSO2 (Fig. 9a), it is only over eastern China that there is a net decrease in the number of sub-grid sulphate particles formed due to the additional SO_2 emissions. This decrease the number of sub-grid particles formed is due to the increase in SO_2 emissions greatly increasing the condensation sink in eastern China (not shown). The median diameter of newly formed particles ($D_{\rm m}$) in simulation P6_hiSO2 increases by 13%-16% over most of the globe (Fig. 4.8c). Thus, both the emitted number and size of sub-grid sulphate particles are increased in the P6_hiSO2 simulation, and sub-grid processes contribute to the increase in the particle concentrations from the increase in SO_2.

The value of $f_{\rm ox}$ in the P6_hiNOx simulations decreases over very polluted regions and increases over remote regions (Fig. 4.8d), but these relative changes are less than 20% (or an absolute change in $f_{\rm ox}$ of 1%) in either direction. Whether $f_{\rm ox}$ decreases or increases depends on the NO_x concentrations in the region. In high-NO_x regimes, in-plume OH concentrations (and hence SO_2 oxidation) will decrease with increasing NO_x, and oxidation will increase with increasing NO_x in low-NO_x regimes. The value of N_{new} in P6_hiNOx decreases by 10%-20% over most of the globe, with greater decreases over Europe and China (Fig. 4.8e). The value of $D_{\rm m}$ decreases by 11%-14% over most of the globe (Fig. 4.8f). These increases in $f_{\rm ox}$ and decreases in $N_{\rm new}$ and $D_{\rm m}$ will result in more sub-grid oxidation of SO_2, but fewer and smaller new particles emitted at the sub-grid scale. Thus, the only change in sub-grid sulphate that may contribute to the modelled increase in N80 (Fig. 4.7b) is an increase in condensation of sub-grid-oxidized SO_2 onto pre-existing particles less than 80 nm in diameter. It is therefore likely that the increases in N80 in this simulation are primarily due to grid-resolved processes.

In the P6_hiboth simulation, the changes in $f_{\rm ox}$ (Fig. 4.8g) are nearly identical to

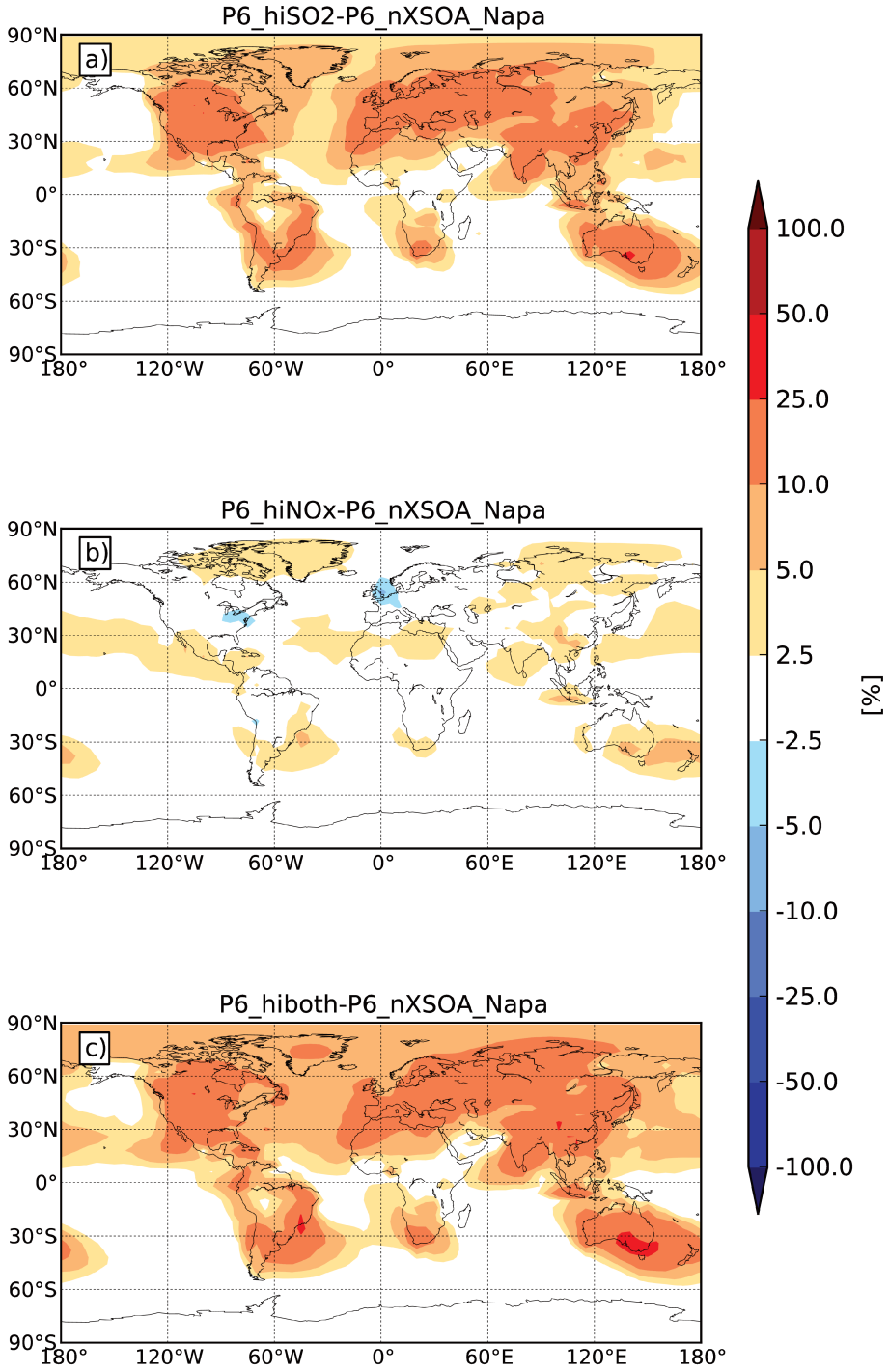

Figure 4.7: Change in annually averaged N80 between a) P6_hiSO2, b) P6_hiNOx, c) P6_hiboth and P6_nXSOA_Napa.

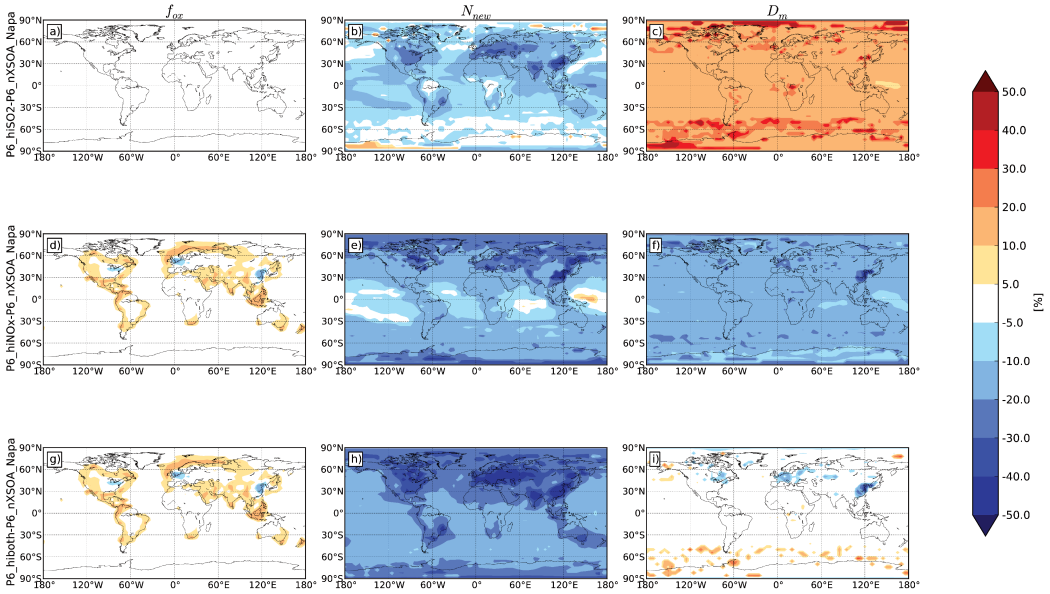

Figure 4.8: Relative changes in the fraction of SO_2 oxidized on the sub-grid scale (f_{ox}), number of newly formed sub-grid sulphate particles per kg SO_2 emitted (N_{new}), and median diameter of sub-grid sulphate particles (D_m) from the P6_nXSOA_Napa simulation to the P6_hiSO2, P6_hiNOx, and P6_hiboth simulations, as calculated offline by the P6 adjoint.

the changes for the P6_hiNOx simulation. The changes in D_m due to increases in SO_2 and increases in NO_x nearly cancel each other over most of the globe (Fig. 4.8i), with some exceptions: D_m decreases over eastern Canada, over Europe, and over Eastern China, and it increases over some regions where no anthropogenic sulphur (and thus no sub-grid sulphate) is emitted. The value of N_{new} decreases, as it did for both the P6_hiSO2 and P6_hiNOx simulations. However, the decreases are sufficiently large over polluted regions, including eastern North America, Europe, India, and China, to result in a net decrease in sub-grid new particle formation, even after accounting for increases due to increased total sulphate emission (Fig. 4.9b). Over the most polluted regions, we thus have decreases in sub-grid oxidation of SO_2 and decreases in the number and size of sub-grid sulphate particles emitted due to increasing SO_2 and NO_x, while less polluted regions show increases in both sub-grid oxidation and the number of sub-grid sulphate particles emitted. Thus changes in sub-grid sulphate are not uniform with respect to changing emissions when the effects of those emissions on grid-resolved SO_2, NO_x, and aerosol condensation sink are included. These results are consistent with Lonsdale et al. (2012), where they found that NO_x and SO_2 emissions

controls may increase or decrease the number of particles in the plume depending on the background NO_x regime, background condensation sinks as well as how strongly NO_x and SO_2 are controlled.

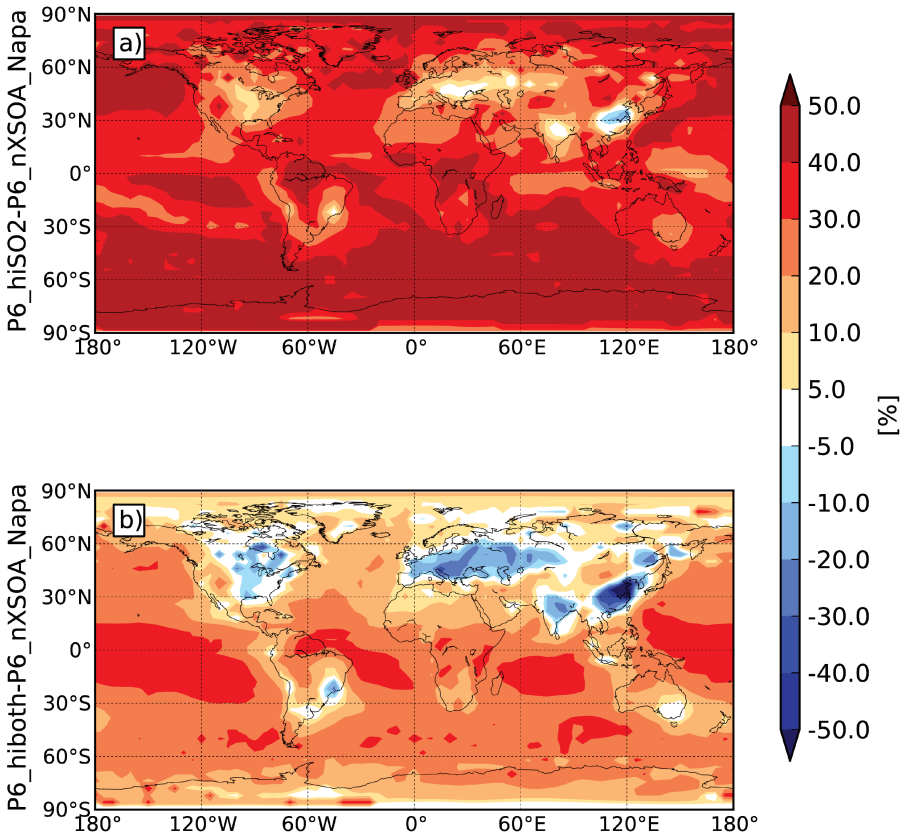

Figure 4.9: Relative change in the number of newly formed sub-grid sulphate particles (including increases due to increases in SO_2 emissions) from the P6_nXSOA_Napa simulation to the a) P6_hiSO2 and b) P6_hiboth simulations, as calculated offline by the P6 adjoint.

4.6 Comparison with Observations

In order to assess the sub-grid sulphate schemes simulated in our study, we used data from the 21 surface-based aerosol size distribution measurements compiled by D'Andrea et al. (2013) from the following sources: the BEACHON campaign (Levin et al., 2012), the European Supersites for Atmospheric Aerosol Research (www.eusaar.net,

Asmi et al., 2011; Reddington et al., 2011), the RoMANS 2 campaign (instrumentation and site descriptions are same as RoMANS 1 campaign as per Levin et al. (2009)), Environment Canada (Leaitch et al., 2013; Pierce et al., 2012; Riipinen et al., 2011), and Kent State University (Erupe et al., 2010; Kanawade et al., 2012). The measurement sites span many terrain types, including forests, mountains, rural sites, arctic sites and coastal sites. However, urban sites were excluded because the 4° x 5° resolution used for this study cannot resolve urban features. All size distribution measurements were obtained using either a Differential Mobility Particle Sizer (DMPS) (Aalto et al., 2001) or a Scanning Mobility Particle Sizer (SMPS) (Wang and Flagan, 1990). For a map of the locations as well as figures showing the size-distribution comparisons for similar simulations, please see D'Andrea et al. (2013).

For brevity, we do not show the full comparisons at the sites in figures, but we list in Table 4.4 the log-mean bias (LMB), slope of a linear regression of the logarithms of the values (m), and coefficient of determination (R^2) between the annually averaged N10, N40, N80, and number concentrations of particles larger than 150 nm (N150) for each simulation (excluding the emissions sensitivity tests) and those measured at the 21 surface sites. These statistics evaluate how well the model captures the magnitude and variability across the measurement sites. We do not compare simulated N3 against observations because measurements of particles smaller than 10 nm were not available at most of the surface sites, and we include N150 to show more information about the larger end of the size distribution. Compared to the choice of SOA amount or grid-resolved nucleation scheme, the choice of sub-grid sulphate scheme has a small effect on the goodness-of-fit metrics shown here. The maximum changes in LMB, m, and R^2 between simulations that differ only in sub-grid sulphate scheme are 0.087, 0.109, and 0.030, respectively. Many other uncertain model parameters and processes can also change aerosol number concentrations, such as emissions and deposition rates, and a change in these parameters or processes within the model may affect our goodness-of-fit metrics.

The simulations without sub-grid sulphate and without anthropogenically controlled SOA (NoSGS_nXSOA) are both biased high for N10, and biased low for N40,

Table 4.4: Log-mean bias (LMB), slope of the log-linear regression (m), and coefficient of determination (R^2) between the simulated annually averaged N10, N40, N80, and N150 and those measured at 21 surface sites. For each group of simulations with the same SOA amount and grid-resolved nucleation scheme, the best statistical result in each column is bolded. For each group of simulations with the same sub-grid sulphate scheme, the best statistical result in each column is italicized.

Simulation	LMB				m				R^2			
	N10	N40	N80	N150	N10	N40	N80	N150	N10	N40	N80	N150
NoSGS_yXSOA_Napa	0.086	*0.018*	0.077	**0.138**	0.813	*0.850*	*0.825*	*0.842*	0.874	**0.893**	***0.863***	*0.784*
AS3_yXSOA_Napa	0.095	0.040	0.102	0.158	0.802	*0.846*	*0.824*	*0.846*	0.885	*0.888*	*0.856*	*0.778*
LY5_yXSOA_Napa	0.122	0.070	0.131	0.180	**0.857**	***0.881***	***0.846***	***0.856***	**0.890**	*0.878*	*0.846*	*0.772*
P6_yXSOA_Napa	**0.061**	***0.003***	**0.071**	0.142	0.798	*0.846*	*0.827*	*0.849*	0.871	0.892	***0.863***	***0.789***
NoSGS_yXSOA_Act	***0.005***	-0.050	***0.029***	***0.113***	0.658	0.780	0.783	0.825	0.866	*0.897*	0.860	0.779
AS3_yXSOA_Act	*0.030*	***-0.011***	*0.067*	*0.141*	0.685	0.803	0.800	0.837	**0.870**	0.883	0.852	0.774
LY5_yXSOA_Act	*0.073*	0.031	0.105	*0.168*	**0.761**	**0.850**	**0.828**	**0.849**	0.858	0.868	0.843	0.769
P6_yXSOA_Act	*-0.007*	-0.056	***0.029***	*0.121*	0.652	0.779	0.785	0.832	**0.870**	***0.898***	**0.862**	**0.784**
NoSGS_nXSOA_Napa	0.308	-0.050	-0.134	-0.256	***0.963***	0.781	0.661	0.577	0.894	0.853	0.833	0.763
AS3_nXSOA_Napa	0.304	-0.042	-0.121	-0.239	*0.948*	0.779	0.670	0.593	0.897	0.858	0.833	0.757
LY5_nXSOA_Napa	0.283	***-0.026***	***-0.093***	**-0.215**	*0.937*	**0.800**	**0.695**	0.612	**0.898**	**0.866**	0.831	0.751
P6_nXSOA_Napa	**0.262**	-0.050	-0.111	**-0.215**	*0.927*	0.794	0.693	**0.623**	0.892	0.863	**0.842**	**0.768**
NoSGS_nXSOA_Act	0.203	-0.115	-0.162	-0.262	0.809	0.729	0.644	0.577	*0.907*	0.864	0.836	0.766
AS3_nXSOA_Act	0.206	-0.099	-0.146	-0.244	0.812	0.738	0.657	0.594	*0.907*	0.866	0.833	0.760
LY5_nXSOA_Act	0.195	**-0.079**	**-0.115**	**-0.218**	**0.813**	**0.764**	**0.682**	0.614	*0.905*	0.869	0.830	0.753
P6_nXSOA_Act	**0.174**	-0.107	-0.136	-0.219	0.785	0.746	0.671	**0.621**	***0.911***	**0.874**	**0.843**	**0.770**

N80, and N150. For these cases, the inclusion of any of the three sub-grid sulphate schemes considered here increases N40, N80, and N150 at the expense of N10, and therefore decreases the absolute LMB. However, when anthropogenically controlled SOA is included, the simulations without sub-grid sulphate (NoSGS_yXSOA) tend to have small positive biases for each size range (except for the NoSGS_yXSOA_Act N40, which has a small negative bias). The AS3 and LY5 sub-grid sulphate schemes increase aerosol concentrations at all sizes for the cases with anthropogenically controlled SOA, (since the extra SOA enhances survivability of the small particles, as shown by D'Andrea et al. (2013)) and so increase this positive bias. The P6 parameterization predicts that a larger fraction of sub-grid sulphate will condense onto pre-existing particles for the cases with this extra SOA due to the increased coagulation sink, and so only N150 increases from the NoSGS_yXSOA cases, and N10, N40, and N80 decrease due to enhanced coagulation from the larger aerosol. These decreases lead to a decrease in the absolute LMB from the NoSGS_yXSOA_Napa case to the P6_yXSOA_Napa case for all size ranges except for N150, and only a small increase in the absolute LMB for all size ranges from the NoSGS_yXSOA_Act case to the P6_nXSOA_Act case.

Log-linear regressions for all cases and all size ranges yield slopes less than 1. This is generally due to an overprediction of aerosol number concentrations at the cleaner sites, and an underprediction of of aerosol number concentrations at the more polluted sites. To a certain extent, this behaviour is expected due to model resolution effects alone. The cleanest sites will be influenced by pollution within the same grid cell, and local pollution sources that may influence the measurements at the most polluted sites will be diluted to the model resolution. For nearly all combinations of size range, SOA amount and grid-resolved nucleation scheme, the LY5 sub-grid sulphate scheme yields the slope closest to one. The differences in aerosol number concentrations between simulations, while small everywhere, are greatest for polluted sites, which would be expected if anthropogenic sulphate is a strong contributor to particle number concentrations at these sites. The LY5 scheme typically predicts more particles at all sites than any other sub-grid sulphate scheme, as evidenced by the more positive LMB, but these differences are most pronounced at the most polluted

sites. Where the LMB is negative, this increase in aerosol number concentrations yields better agreement with measurements at the more polluted sites. Where the LMB is positive, this increase yields a worse agreement with the measurements at the more polluted sites, but a more consistent bias against the measurements across all of the sites.

Regardless of the SOA amount or grid-resolved nucleation scheme used, simulations using P6 sub-grid sulphate had higher R^2 values for N80 and N150 than any other sub-grid sulphate scheme included in this study. For those cases using activation nucleation, the simulations using the P6 scheme had the highest R^2 values for N10 and N40 as well. While this difference is small, we believe that this improved correlation is due to the fact that the P6 parameterization predicts different amounts and sizes of sub-grid sulphate under different conditions, and thus can represent more spatial heterogeneity that the other sub-grid sulphate schemes tested in this study.

4.7 Conclusions

In this study, we implemented the P6 parameterization for sub-grid sulphate into the GEOS-Chem-TOMAS global chemical-transport model. This is the first implementation of P6 into a global model. We have shown that the P6 parameterization predicts smaller or similar increases in globally, annually averaged N80 attributable to sub-grid sulphate than two other previously used assumptions for sub-grid sulphate, depending on model assumptions regarding SOA and nucleation. When we included emissions of an additional 100 Tg yr^{-1} of SOA while using previous treatments of sub-grid sulphate, the increases in N80 attributable to sub-grid sulphate increased. This increase was due to increases in condensational growth of the sub-grid sulphate particles. The proportion of global N80 attributable to sub-grid sulphate depends not only on the choice of sub-grid sulphate scheme, but also on other model parameters and processes that affect pre-existing N80 and the grid-resolved condensational growth of sub-grid sulphate.

However, the number of new sub-grid sulphate particles predicted by the P6 parameterization depends strongly on the pre-existing aerosol condensation sink. The increase in pre-existing condensation sink due to the additional SOA drastically decreased the sub-grid new-particle formation predicted by the P6 parameterization, thus decreasing the influence of sub-grid sulphate on N80. For sufficiently large pre-existing condensation sink, the P6 sub-grid sulphate scheme predicted that nearly all sub-grid sulphate would condense onto pre-existing particles, and the growth of these particles resulted in enhanced coagulational losses and more efficient removal by deposition, producing little change in aerosol number concentrations.

In addition, we tested the sensitivity of the results of GEOS-Chem-TOMAS with P6 sub-grid sulphate to changes in emissions. We found that global increases in SO_2 emissions, NO_x emissions, or both SO_2 and NO_x emissions by 50% would increase globally, annually averaged N80 by 9.00%, 1.47%, or 10.24%, respectively. Increases in SO_2 emissions generally increase both the size and number of sub-grid sulphate particles emitted, as well as increasing grid-resolved SO_2 available to form SO_4. Increases in NO_x emissions increase both sub-grid and grid-resolved oxidation of SO_2 except in very polluted (NO_x concentrations $> \sim$1ppb) regions, where increasing NO_x concentrations decrease oxidation rates. Increased NO_x emissions also decrease both the number and size of sub-grid particles emitted. The combined effect of increases in SO_2 and NO_x emissions is a decrease in the number of sub-grid sulphate particles emitted over polluted regions, an increase in the number of sub-grid sulphate particles emitted over remote regions, and little change in the size of sub-grid sulphate particles.

Finally, we have compared the simulated annually averaged N10, N40, N80, and N150 against those measured at 21 surface-based measurement sites. Differences in sub-grid sulphate scheme were not found to strongly affect the number concentrations in these size ranges at these sites. For cases without anthropogenically controlled SOA, a reduction in the absolute log-mean bias between simulated and observed number concentrations was obtained by including any sub-grid sulphate scheme. When anthropogenically controlled SOA was included, the AS3 and LY5 schemes tended to increase the absolute log-mean bias. The P6 sub-grid sulphate scheme only slightly

increased the absolute log-mean bias or reduced the absolute log-mean bias from the case with no sub-grid sulphate. This was due to the reduction in new-particle formation predicted under higher condensation sink conditions. The R^2 values for N80 and N150 were highest when using the P6 sub-grid sulphate scheme, regardless of SOA amount or grid-resolved nucleation scheme. For the Activation-type grid-resolved nucleation cases, the P6 sub-grid sulphate scheme also yielded the highest R^2 values for the N10 and N40, as well. We believe that the P6 scheme yields better correlation with observations because the differences in sub-grid scale new-particle formation and growth under different conditions predicted by the P6 sub-grid sulphate scheme allows it to better represent spatial heterogeneity in these processes than constant assumptions about the number and size of sulphate formed at the sub-grid scale.

The additional anthropogenically controlled SOA included in many of our simulations would be expected to condense onto the newly formed particles at the sub-grid scale, a process that is not currently resolved by P6. Anthropogenically controlled SOA may preferentially form in coal-fired power-plant plumes, and so this additional SOA may condense preferentially onto particles formed within these plumes compared to pre-existing particles. The P6 parameterization thus likely underestimates the number and size of newly formed particles in simulations where anthropogenically controlled SOA is included. However, we note that when the anthropogenically controlled SOA was included, the simulations with P6 sub-grid sulphate had smaller absolute log-mean biases from observed aerosol number concentrations than the simulations with AS3 or LY5 sub-grid sulphate, and similar absolute log-mean biases to the simulations with no sub-grid sulphate. This would suggest that the number of newly formed particles predicted by P6 when anthropogenically controlled SOA is included may be more realistic than the number of newly formed particles predicted by the AS3 or LY5 sub-grid sulphate assumptions. Other uncertain model processes also influence aerosol number concentrations, so it is also possible that the P6 parameterization benefits from a cancelling of errors in this case. We intend to include sub-grid condensation of SOA in a future version of P6 to better resolve these uncertainties.

Due to the physical basis of the P6 parameterization, we believe it to yield more

representative predictions for the number and size of aerosol formed than previous assumptions about sub-grid sulphate. Moreover, no constant assumption about the number and size of sub-grid sulphate formed can resolve differences in new-particle formation and growth due to changes in background chemical or meteorological conditions. However, the differences between simulated size distributions at the surface-based measurement sites considered in this work were too small to establish P6 as unambiguously providing better agreement with observations. Continuing evaluation of the P6 parameterization against observations is therefore planned as future work.

Chapter 5

Conclusion

5.1 Summary

Aerosols have been shown to have detrimental effects on human health (Arya, 1999; Dockery et al., 1993; Peng et al., 2005; Stieb et al., 2002) and a cooling effect on climate (Albrecht, 1989; Twomey, 1974; Charlson et al., 1992; Dusek et al., 2006; Boucher et al., 2013). Sulphur-rich emissions plumes are one of the largest sources of anthropogenic aerosol to the atmosphere (Dentener et al., 2006). However, global- and regional-scale models with resolutions of 100s and 10s of kilometres, respectively, cannot resolve the new-particle formation and growth that occurs in these plumes. These models have therefore typically used crude assumptions about the size and amount of aerosol formed within these plumes that do not depend on emissions, meteorological conditions, or background pollutant concentrations. These assumptions have been shown to have large effects on aerosol number and cloud condensation nuclei (CCN) concentrations (Adams and Seinfeld, 2003; Spracklen et al., 2005; Wang and Penner, 2009; Luo and Yu, 2011; Lee et al., 2013). Better representation of the new-particle formation and growth within these plumes is therefore necessary to provide better estimates of effects on human health and climate of these particles.

In order to study the new-particle formation and growth and growth within these plumes, we implemented TwO-Moment Aerosol Sectional (TOMAS) microphysics into the System for Atmospheric Modelling (SAM), a Large-Eddy Simulation (LES) / Cloud Resolving Model (CRM). We have shown that the SAM-TOMAS model provides reasonable predictions of new-particle formation and growth within the plumes of two coal-fired power plants at distances further than 10-20 km from the source. We have also shown that the amount of new-particle formation and growth strongly depends on the amount of sunlight simulated, through its control of OH concentrations, and on background aerosol concentrations, which suppress new-particle formation

and growth by acting as a condensational sink for H_2SO_4 and a coagulational sink of newly formed particles.

We then performed thousands of simulations using the SAM-TOMAS model with varying emissions, meteorological conditions, and background aerosol and trace gas concentrations. Based on the results of these simulations, we created the Predicting Particles Produced in Power-Plant Plumes (P6) parameterization: a computationally efficient, but physically-based parameterization that predicts the characteristics of aerosol formed within sulphur-rich plumes using variables commonly available in global- and regional-scale models. We have shown that the results of the parameterization show good agreement with the results of the SAM-TOMAS model and that the P6 parameterization captures the variability in aerosol formation and growth in sulphur-rich plumes, with correlation coefficients ranging from 0.650 for f_{new} to 0.891 for f_{ox}.

We have implemented the P6 parameterization into the GEOS-Chem-TOMAS global chemical-transport model. We have shown that the P6 parameterization predicts smaller or similar increases in N80 attributable to sub-grid sulphate than two other previously-used assumptions for sub-grid sulphate, depending on model assumptions regarding nucleation and amount of secondary organic aerosol (SOA). An increase in the annual production of condensible SOA was shown to increase the number concentration of particles larger than 80 nm (N80) attributable to sub-grid sulphate when using previous sub-grid sulphate schemes. This was due to increases in condensational growth of sub-grid sulphate particles. However, when we used the P6 parameterization to predict sub-grid sulphate, an increase in condensible SOA increased the background aerosol condensation sink, which caused P6 to predict much less sub-grid new-particle formation and growth than without the extra SOA. This resulted in a decrease in the additional N80 attributable to sub-grid sulphate, contrary to what was predicted using previous sub-grid sulphate schemes. The proportion of global N80 attributable to sub-grid sulphate therefore depends not only on the choice of sub-grid sulphate scheme, but also on other model parameters and processes that affect pre-existing N80 concentrations and the grid-resolved condensational growth of

sub-grid sulphate.

Finally, we compare the model results against obervations of particle number concentrations. While the differences in aerosol number concentrations due to the treatment of sub-grid sulphate were too small to unambiguously establish the P6 parameterization as providing better agreement with observations than the other sub-grid sulphate schemes tested here, the P6 parameterization does generally improve correlation with observations. We believe that the improved corellation is due to the ability of the P6 parameterization to resolve spatial heterogeneity in sub-grid new-particle formation and growth, which is impossible for any constant assumption about sub-grid sulphate.

Through these three studies, we have first shown that new-particle formation and growth in sulphur-rich plumes depends strongly on meteorological conditions and pre-existing aerosol condensation sink. We then created the P6 parameterization for use in global- and regional-scale models to resolve this variability in new-particle formation and growth, and to better predict the amount and size of aerosol formed within these plumes. Finally, we have implemented the P6 parameterization into a global chemical-transport model, and we have shown how the results compare to those of two previously-used sub-grid sulphate schemes.

5.2 Future Work

In Sect. 2.3, we showed that while the SAM-TOMAS predictions compare well with observations beyond 10-20 km from the source, the SAM-TOMAS model underpredicted aerosol number concentrations close to the source. The observed particles may be due to emissions of SO_3, which would quickly oxidize to form H_2SO_4, or emissions of HONO, which may photolyse to create an OH source near the stack (where there is normally a minimum in OH) (Cichanowicz, 2007; Mueller and Imhoff, 1994; Srivastava et al., 2004; Zaveri et al., 2010). SO_3 emissions may provide a source of aerosol during night-time conditions, when little oxidation of SO_2 by OH would be expected. This source of aerosol can be represented within the SAM-TOMAS model by implementing either direct emissions of H_2SO_4 gas or sulphate aerosol from the

stack. The emissions can be constrained by size-resolved observations of new-particle formation within power-plant plumes during night-time conditions, which was one of the goals of the aircraft-based 2013 Southeast Nexus (SENEX) field campaign (http://www.esrl.noaa.gov/csd/projects/senex/). We can then use the SAM-TOMAS model to test whether this additional source of aerosol would significantly change the amount and size of aerosol produced in aerosol plumes during daytime conditions, and incorporate them into a future version of P6, if necessary.

We also did not account for SOA formation within sulphur-rich plumes, which may increase new-particle formation rates and would increase the growth rates of these particles. SOA formation may be enhanced within such anthropogenic plumes compared to background conditions (Spracklen et al., 2011), and so this may be an especially important growth mechanism within sulphur-rich plumes. In order to constrain these effects, observations would be needed in sulphur-rich plumes emitted into regions with high concentrations of volatile organic compounds (VOCs). Fortunately, this was another goal of the 2013 SENEX campaign. Future work should include implementing SOA formation into the SAM-TOMAS model, and then to compare the results of the extended SAM-TOMAS model against observations from the SENEX campaign where high VOC concentrations were observed. Once we are confident that these processes are well-represented by the SAM-TOMAS model, we can incorporate them into a future version of the P6 parameterization.

A third process not accounted for by SAM-TOMAS, and hence by P6, is the aqueous-phase oxidation of SO_2 within clouds. This process would cause SAM-TOMAS and P6 to underestimate the fraction of SO_2 oxidized under cloudy conditions. The SAM-TOMAS model can be extended to include this aqueous-phase oxidation based on liquid water contents already predicted by the model. We can then compare the predictions of SAM-TOMAS against observations taken during the SENEX field campaign for multiple plumes with varying amounts of cloudiness. Once we are satisfied that this process is well-represented within SAM-TOMAS, we can incorporate it into a future version of the P6 parameterization.

The surface-based observations used for comparison in Sect. 4.6 were insufficient to determine unambiguously whether the P6 sub-grid sulphate scheme provides better agreement with observations than previously-used assumptions about sub-grid sulphate. We therefore intend to continue evaluation of the P6 parameterization against observations. We intend to test the results of the P6 parameterization without the use of a global or regional model against observations of new-particle formation and growth within sulphur-rich plumes from the 2013 SENEX campaign described above. Additionally, as the predictions of the P6 parameterization would vary seasonally due to changes in meteorological conditions as well as seasonal differences in background pollutant concentrations, it is possible that the P6 parameterization would capture seasonal cycles in sub-grid new-particle formation and growth that cannot be captured by a constant assumption about the number and size of aerosol formed at the sub-grid scale. We may be able to better evaluate the P6 parameterization implemented in a global model by comparing against observed seasonal cycles in size-resolved aerosol number concentrations at surface-based sites averaged across multiple years.

While the P6 parameterization was designed with coal-fired power plants in mind, it may be applicable for other sulphur-rich plumes. For instance, aerosol formation has been shown to occur in volcanic plumes (Boulon et al., 2011), but this aerosol formation is very uncertain in part because of the variability in new-particle formation and growth due to differences in meteorological conditions and pre-existing aerosol condensation sink. As volcanic emissions often occur in much less polluted regions than anthropogenic emissions, more new-particle formation may occur in volcanic plumes relative to the SO_2 emissions than in anthropogenic plumes. We intend to apply the P6 parameterization to volcanic emissions in order to determine an estimate of the aerosol formation and growth within volcanic plumes.

Appendix A

OH Parameterization Details

As mentioned in Sect. 2.2, the OH parameterization used in the SAM-TOMAS model is an empirical fit to the results of many simulations from the detailed time-dependent photochemical box model described by Olson et al. (2006). These simulations span conditions observed below 1 km over the eastern United States as sampled from the NASA DC-8 during the Intercontinental Chemical Transport Experiment-North America (INTEX-A) field campaign (Singh et al., 2006). Thus, the values of the inputs to the box model covered a wide range (e.g., ozone concentrations ranging from 20-80 ppbv). The OH parameterization fits the detailed model calculations well for all simulations except those with high levels of isoprene. Thus, the initial parameterization was derived based on calculations for conditions where the observed isoprene mixing ratio was 150 pptv or less. This base OH parameterization is referred to as the "low-VOC" case. The OH parameterization works as follows. First, we set variables x and y:

$$x = \log([\mathrm{NO_x}]) - 0.195 \tag{A.1}$$

$$y = \frac{DSWRF}{S_0 \cdot T} \tag{A.2}$$

Where $[\mathrm{NO_x}]$ is the mixing ratio of $\mathrm{NO_x}$ in ppbv, $DSWRF$ is the downward shortwave radiative flux at the surface in W $\mathrm{m^{-2}}$, $\mathrm{S_0}$ is the solar constant at the top of the atmosphere, 1370 W $\mathrm{m^{-2}}$, and T is an assumed transmittance of the clear atmosphere, 0.76. The first polynomial ($P1$) estimates the shape of the OH versus $\mathrm{NO_x}$ relationship:

$$P1 = -0.014x^6 + 0.0027x^5 + 0.1713x^4 - 0.0466x^3 - 0.7893x^2 - 0.1739x + 6.9414 \tag{A.3}$$

The second polynomial ($P2$) scales the curve based on $DSWRF$:

$$P2 = (-1345y^3 + 4002y^2 - 471.8y + 42.72) \cdot 10^4 \tag{A.4}$$

Finally, we calculate the concentration of OH in molecules per $\mathrm{cm^3}$:

$$[\mathrm{OH}] = 0.82 \cdot 10^{P1 \cdot \log(P2)/6.8} \tag{A.5}$$

One process not accounted for in the OH parameterization is the effect of the presence of large amounts of highly reactive VOCs on OH production. This was revealed by the difficulty in devising a parameterization that could encompass the OH calculations associated with high isoprene mixing ratios during INTEX-A. The additional peroxy radicals from isoprene oxidation induce a shift in the peak OH production to a higher NO_x level. To understand the potential effect of high VOC concentrations in our study, a second parameterization, referred to as the high-VOC case, was developed based on an isoprene mixing ratio of 1.5 ppbv (the 95th percentile value observed during INTEX-A). This parameterization uses the the following equation for x (all other equations the same):

$$x = \log([NO_x] \cdot 0.6) - 0.195 \tag{A.6}$$

In this way, we shift the concentration of NO_x that corresponds to the peak concentration of OH from ∼1.2 ppbv in the low-VOC case to ∼2.0 ppbv in the high-VOC case. Due to the proximity of our test cases to known biogenic and anthropogenic sources of VOCs, we assume high-VOC conditions for purposes of calculating OH in all the model runs described in Chapter 2, except where explicitly stated otherwise. In the Parish case, the plume passes over major roadways and urban sprawl surrounding Houston; In the Conesville case, the plume passes over a heavily forested region during late summer when biogenic emissions would be high. We perform sensitivity simulations to test this high-VOC assumption.

As a final note regarding the calculation of OH, it is important to point out that field observations suggest that current chemical mechanisms tend to underestimate OH levels in environments of low NO_x and high isoprene (Lelieveld et al., 2008; Hofzumahaus et al., 2009; Stone et al., 2011). While adequate chemical mechanisms to represent these field observations do not exist, it is reasonable to expect that true peak OH concentrations are shifted to lower NO_x than these calculations would suggest.

Appendix B

What If One or More of the P6 Inputs are Not Available?

E_{SO2}, E_{NOx}: If no estimate of the SO_2 emissions is available, the P6 parameterization can be run assuming a representative distribution of power-plants within the area. This is described in more detail in Sect. 3.3. If the total NO_x emissions are unknown, the parameterization will assume a E_{SO2}:E_{NOx} ratio of 0.419 based on the 2010 CAM data.

$DSWRF$: The clear-sky $DSWRF$ can be calculated by:

$$DSWRF = S_0\, T \cos(sza) \tag{B.1}$$

where S_0 is the solar constant at the top of the atmosphere, 1370 W m^{-2}, T is the transmittance of the atmosphere, and sza is the solar zenith angle. The clear-sky transmittance has a value of about 0.76 (globally averaged, (Seinfeld and Pandis, 2006)), and the solar zenith angle can be calculated based on the latitude, longitude, time of day and day of year. This approximation will typically over-estimate $DSWRF$, as it assumes no cloud cover. If no input is given, a value of 400 W m^{-2} will be assumed.

CS: The value of CS can be approximated based on a typical aerosol background for the location in question. We note that the typical aerosol size distributions listed in (Seinfeld and Pandis, 2006) for urban, rural, remote continental, and marine conditions correspond to condensation sinks of 0.060 s^{-1}, 0.0063 s^{-1}, 0.011 s^{-1}, and 0.0010 s^{-1}, respectively. Also, the remote continental size distribution yields a PM10 mass concentration of 25.88 μg m^{-3}, so we suggest that CS may be estimated from PM10 mass concentrations by multiplying by 4.3×10^{-4} $s^{-1}(\mu g\ m^{-3})^{-1}$. If no input is given, we will assume the value for a remote continental case, 0.011 s^{-1}.

v_g: The value of v_g must be assumed if not known. We choose a typical value of 6 m s^{-1} if no input is given.

BLH: The BLH can be approximated by typical values for the location and time of day. If no value is given, a value of 500 m will be assumed.

d: We recognize that there is some ambiguity about what value should be used as input for d by global and regional-scale model users. One interpretation is that d is the distance where the air mass passing over the source enters the next adjacent grid-cell. Another is the distance where the width of the plume equals the grid width, allowing the plume to be resolved. However, solving for either of these distances under changing wind direction and meteorological conditions is not a trivial task even if the location of the power plant within the grid cell is known, and often the location will not be available. We suggest then that users of our parameterization use half the horizontal grid cell resolution as an approximation for d. We show in our sensitivity studies that for distances greater than 30 km, M_m, N_{new}, and f_{new} are not strongly dependant on d, and f_{ox} is a less than linearly function of d.

$bgSO_2$,$bgNO_x$: Following tables 2.7 of Seinfeld and Pandis (2006), we suggest values of $bgNO_x$ of 10 ppb for urban locations, 1 ppb for rural locations, and 0.05 ppb for remote locations. For $bgSO_2$ we suggest values of 10 ppb for urban locations, and 0.5 ppb for remote continental conditions, and 0.05 for marine conditions. If no input is given, values of 0.5 ppb and 1 ppb are used for $bgSO_2$ and $bgNO_x$.

Appendix C

Summary of Equations Necessary for Each P6 Output

We note that the full parameterization is available programmed in Fortran 90 as a supplement. However, if the provided code is insufficient for the users' needs, we request that the users contact the authors to find out if the P6 parameterization has already been translated into the necessary programming language, if the necessary adjustments have already been made, or if an updated version is available. In the case where this still proves insufficient, we summarize in this appendix which equations from the preceding manuscript are necessary to calculate each output. We strongly recommend that users consult the preceeding manuscript for a full discussion of caveats and assumptions associated with the P6 parameterization. We also recommend that users ensure that they use the correct value from Table 3.5 whenever they use Eq. 3.1 or Eq. 3.9.

Fraction of SO_2 oxidized ($f_{\rm ox}$):
Eq. 3.1-3.6, 3.8 (2^{nd} row from Table 3.5).

Nucleation:
Eq. 3.1, 3.9, 3.10 (3^{rd} row from Table 3.5).

Mean mass of new particles ($M_{\rm m}$):
First, determine if significant nucleation has occurred ($M_{\rm m}$ is poorly defined otherwise):
Eq. 3.1, 3.9, 3.10 (3^{rd} row from Table 3.5).
Then calculate $f_{ox,eff}$: Eq. 3.1-3.6, 3.8 (4th row from Table 3.5).
Then Eq. 3.11.
If you are also using $f_{\rm new}$, calculate it now as noted below. If $f_{\rm new} > 1$, divide $M_{\rm m}$ by ${f_{new}}^{0.5}$ to maintain closure.

Median diameter of new particles (D_{m}):
Calculate M_{m} as noted above. Then Eq. 3.12, 3.13.

Number of new particles per kg SO_2 (N_{new}):
First, determine if significant nucleation has occurred (N_{new} very small otherwise):
Eq. 3.1, 3.9, 3.10 (3^{rd} row from Table 3.5).
Then calculate f_{ox},eff: Eq. 3.1-3.6, 3.8 (5th row from Table 3.5).
Then Eq. 14.
If you are also using f_{new}, calculate it now as noted below. If $f_{\mathrm{new}} > 1$, divide N_{new} by ${f_{new}}^{0.5}$ to maintain closure.

Fraction of sulphate mass that comprises new particles (f_{new}):
Calculate f_{ox}, M_{m}, and N_{new} as noted above. Then use Eq. 3.15.

Bibliography

Aalto, P., Hämeri, K., Becker, E., Weber, R., Salm, J., Mäkelä, J. M., Hoell, C., O'Dowd, C. D., Karlsson, H., Hansson, H.-C., Väkevä, M., Koponen, I. K., Buzorius, G., and Kulmala, M.: Physical characterization of aerosol particles during nucleation events, Tellus B, 53, 344–358, 2001.

Adams, P. J. and Seinfeld, J. H.: Predicting global aerosol size distributions in general circulation models, Journal of Geophysical Research, 107, 1–23, doi: 10.1029/2001JD001010, 2002.

Adams, P. J. and Seinfeld, J. H.: Disproportionate impact of particulate emissions on global cloud condensation nuclei concentrations, Geophysical Research Letters, 30, 1239, doi:10.1029/2002GL016303, 2003.

Albrecht, B.: Aerosols, cloud microphysics, and fractional cloudiness., Science (New York, NY), 245, 1227–1230, 1989.

Arya, S. P.: Air Pollution Meteorology and Dispersion, Oxford University Press, Inc., New York, USA, 1999.

Asmi, a., Wiedensohler, a., Laj, P., a. M. Fjaeraa, Sellegri, K., Birmili, W., Weingartner, E., Baltensperger, U., Zdimal, V., Zikova, N., Putaud, J.-P., Marinoni, a., Tunved, P., Hansson, H.-C., Fiebig, M., Kivekäs, N., Lihavainen, H., Asmi, E., Ulevicius, V., Aalto, P. P., Swietlicki, E., Kristensson, a., Mihalopoulos, N., Kalivitis, N., Kalapov, I., Kiss, G., de Leeuw, G., Henzing, B., Harrison, R. M., Beddows, D., O'Dowd, C., Jennings, S. G., Flentje, H., Weinhold, K., Meinhardt, F., Ries, L., and Kulmala, M.: Number size distributions and seasonality of submicron particles in Europe 20082009, Atmospheric Chemistry and Physics, 11, 5505–5538, doi:10.5194/acp-11-5505-2011, 2011.

Auvray, M. and Bey, I.: Long-range transport to Europe: Seasonal variations and implications for the European ozone budget, Journal of Geophysical Research, 110, D11 303, doi:10.1029/2004JD005503, 2005.

Bey, I., Jacob, D. J., Yantosca, R. M., Logan, J. a., Field, B. D., Fiore, A. M., Li, Q., Liu, H. Y., Mickley, L. J., and Schultz, M. G.: Global modeling of tropospheric chemistry with assimilated meteorology: Model description and evaluation, Journal of Geophysical Research, 106, 23 073, doi:10.1029/2001JD000807, 2001.

Boucher, O., Randall, D., Artaxo, P., Bretherton, C., Feingold, G., Forster, P., Kerminen, V.-M., Kondo, Y., Liao, H., Lohmann, U., Rasch, P., Satheesh, S., Sherwood, S., Stevens, B., and Zhang, X.: Clouds and Aerosols, in: Climate Change 2013: The Physical Science Basis. Contribution of Working Group I to the Fifth Assessment Report of the Intergovernmental Panel on Climate Change, edited by Stocker, T., Qin, D., Plattner, G.-K., Tignor, M., Allen, S., Boschung, J., Nauels, A., Xia, Y., Bex, V., and Midgley, P., chap. 7, pp. 571–657, Cambridge University Press, Cambridge, United Kingdom and New York, NY, USA, 2013.

Boulon, J., Sellegri, K., Hervo, M., and Laj, P.: Observations of nucleation of new particles in a volcanic plume., Proceedings of the National Academy of Sciences of the United States of America, 108, 12 223–6, doi:10.1073/pnas.1104923108, 2011.

Brown, S. S., Dubé, W. P., Osthoff, H. D., Stutz, J., Ryerson, T. B., Wollny, A. G., Brock, C. a., Warneke, C., de Gouw, J. a., Atlas, E., Neuman, J. A., Holloway, J. S., Lerner, B. M., Williams, E. J., Kuster, W. C., Goldan, P. D., Angevine, W. M., Trainer, M., Fehsenfeld, F. C., and Ravishankara, a. R.: Vertical profiles in NO_3 and N_2O_5 measured from an aircraft: Results from the NOAA P-3 and surface platforms during the New England Air Quality Study 2004, Journal of Geophysical Research, 112, D22 304, doi:10.1029/2007JD008883, 2007.

Carlton, a. G., Wiedinmyer, C., and Kroll, J. H.: A review of Secondary Organic Aerosol (SOA) formation from isoprene, Atmospheric Chemistry and Physics Discussions, 9, 8261–8305, doi:10.5194/acpd-9-8261-2009, 2009.

Carlton, A. G., Pinder, R. W., Bhave, P. V., and Pouliot, G. A.: To what extent can biogenic SOA be controlled?, Environmental science & technology, 44, 3376–80, doi:10.1021/es903506b, 2010.

Charlson, R. J., Schwartz, S. E., Hales, J. M., Cess, R. D., Coakley, J. a., Hansen, J. E., and Hofmann, D. J.: Climate forcing by anthropogenic aerosols., Science (New York, N.Y.), 255, 423–430, doi:10.1126/science.255.5043.423, 1992.

Cichanowicz, J. E.: Estimating total sulfuric acid emissions from stationary power plants, Rep. 1016384, Tech. rep., Electr. Power Res. Inst., Palo Alto, California, 2007.

D'Andrea, S. D., Häkkinen, S. a. K., Westervelt, D. M., Kuang, C., Levin, E. J. T., Kanawade, V. P., Leaitch, W. R., Spracklen, D. V., Riipinen, I., and Pierce, J. R.: Understanding global secondary organic aerosol amount and size-resolved condensational behavior, Atmospheric Chemistry and Physics, 13, 11 519–11 534, doi:10.5194/acp-13-11519-2013, 2013.

Dentener, F., Kinne, S., Bond, T., Boucher, O., Cofala, J., Generoso, S., Ginoux, P., Gong, S., Hoelzemann, J. J., Ito, A., Marelli, L., Penner, J. E., Putaud, J. P., Textor, C., Schulz, M., Van Der Werf, G. R., and Wilson, J.: Emissions of primary aerosol and precursor gases in the years 2000 and 1750 prescribed data-sets for AeroCom, Atmospheric Chemistry and Physics, 6, 4321–4344, doi: 10.5194/acpd-6-2703-2006, 2006.

Dockery, D., Pope, C., Xu, X., Spengler, J. D., Ware, J. H., Fay, M. E., Ferris, B. G., and Speizer, F. E.: An association between air pollution and mortality in six US cities, New England Journal of Medicine, 329, 1753–1759, doi:10.1056/NEJM199312093292401, 1993.

Dusek, U., Frank, G. P., Hildebrandt, L., Curtius, J., Schneider, J., Walter, S., Chand, D., Drewnick, F., Hings, S., Jung, D., Borrmann, S., and Andreae, M. O.: Size matters more than chemistry for cloud-nucleating ability of aerosol particles., Science (New York, N.Y.), 312, 1375–8, doi:10.1126/science.1125261, 2006.

Eisele, F. and Tanner, D.: Measurement of the gas phase concentration of H2SO4 and methane sulfonic acid and estimates of H2SO4 production and loss in the atmosphere, Journal of Geophysical Research, 98, 9001–9010, 1993.

Erupe, M. E., Benson, D. R., Li, J., Young, L.-H., Verheggen, B., Al-Refai, M., Tahboub, O., Cunningham, V., Frimpong, F., Viggiano, A. a., and Lee, S.-H.: Correlation of aerosol nucleation rate with sulfuric acid and ammonia in Kent, Ohio: An atmospheric observation, Journal of Geophysical Research, 115, D23 216, doi:10.1029/2010JD013942, 2010.

Fanaki, F. H.: Experimental Observations of a Bifurcated Buoyant Blume, Boundary-Layer Meteorology, 9, 479–495, 1975.

Guenther, A., Karl, T., Harley, P., Wiedinmyer, C., Palmer, P. I., and Geron, C.: Estimates of global terrestrial isoprene emissions using MEGAN (Model of Emissions of Gases and Aerosols from Nature), Atmospheric Chemistry and Physics Discussions, 6, 107–173, doi:10.5194/acpd-6-107-2006, 2006.

Harrison, R. G. and Carslaw, K. S.: Ion-aerosol-cloud processes in the lower atmosphere, Reviews of Geophysics, 41, 1012, doi:10.1029/2002RG000114, 2003.

Heald, C. L., Coe, H., Jimenez, J. L., Weber, R. J., Bahreini, R., Middlebrook, a. M., Russell, L. M., Jolleys, M., Fu, T.-M., Allan, J. D., Bower, K. N., Capes, G., Crosier, J., Morgan, W. T., Robinson, N. H., Williams, P. I., Cubison, M. J., DeCarlo, P. F., and Dunlea, E. J.: Exploring the vertical profile of atmospheric organic aerosol: comparing 17 aircraft field campaigns with a global model, Atmospheric Chemistry and Physics, 11, 12 673–12 696, doi:10.5194/acp-11-12673-2011, 2011.

Heald, C. L., Lee, T., Benedict, K. B., Schwandner, F. M., Li, Y., Clarisse, L., Hurtmans, D. R., Van Damme, M., Clerbaux, C., Coheur, P.-F., Philip, S., Martin, R. V., and Pye, H. O. T.: Atmospheric ammonia and particulate inorganic nitrogen over the United States, Atmospheric Chemistry and Physics, 12, 10 295–10 312, doi: 10.5194/acp-12-10295-2012, 2012.

Hegg, D. a. and Hobbs, P. V.: Measurements of gas-to-particle conversion in the plumes from five coal-fired electric power plants, Atmospheric Environment (1967), 14, 99–116, doi:10.1016/0004-6981(80)90113-4, 1980.

Hegg, D. a., Hobbs, P. V., and Lyons, J. H.: Field studies of a power plant plume in the arid southwestern United States, Atmospheric Environment (1967), 19, 1147–1167, doi:10.1016/0004-6981(85)90199-4, 1985.

Hofzumahaus, A., Rohrer, F., Lu, K., Bohn, B., Brauers, T., Chang, C.-C., Fuchs, H., Holland, F., Kita, K., Kondo, Y., Li, X., Lou, S., Shao, M., Zeng, L., Wahner, A., and Zhang, Y.: Amplified trace gas removal in the troposphere., Science (New York, N.Y.), 324, 1702–4, doi:10.1126/science.1164566, 2009.

Jung, J., Fountoukis, C., Adams, P. J., and Pandis, S. N.: Simulation of in situ ultrafine particle formation in the eastern United States using PMCAMx-UF, Journal of Geophysical Research: Atmospheres, 115, doi:10.1029/2009JD012313, 2010.

Kanawade, V. P., Benson, D. R., and Lee, S.-H.: Statistical analysis of 4-year observations of aerosol sizes in a semi-rural continental environment, Atmospheric Environment, 59, 30–38, doi:10.1016/j.atmosenv.2012.05.047, 2012.

Kerminen, V., Lehtinen, K., Anttila, T., and Kulmala, M.: Dynamics of atmospheric nucleation mode particles: a timescale analysis, Tellus B, 56, 135–146, 2004.

Kerminen, V.-M. and Kulmala, M.: Analytical formulae connecting the real and the apparent nucleation rate and the nuclei number concentration for atmospheric nucleation events, Journal of Aerosol Science, 33, 609–622, doi:10.1016/S0021-8502(01)00194-X, 2002.

Khairoutdinov, M. and Randall, D.: Cloud resolving modeling of the ARM summer 1997 IOP: Model formulation, results, uncertainties, and sensitivities, Journal of the Atmospheric Sciences, 60, 607–626, doi:10.1175/1520-0469(2003)060⟨0607:CRMOTA⟩2.0.CO;2, 2003.

Kleffmann, J.: Daytime sources of nitrous acid (HONO) in the atmospheric boundary layer., Chemphyschem : a European journal of chemical physics and physical chemistry, 8, 1137–44, doi:10.1002/cphc.200700016, 2007.

Kuhns, H., Green, M., and Etyemezian, V.: Big Bend Regional Aerosol and Visibility Observational (BRAVO) Study Emissions Inventory, technical report prepared for the BRAVO Steering Committee, Tech. Rep. 702, 2001.

Kulmala, M. and Kerminen, V.-M.: On the formation and growth of atmospheric nanoparticles, Atmospheric Research, 90, 132–150, doi:10.1016/j.atmosres.2008.01.005, 2008.

Kulmala, M., Lehtinen, K., and Laaksonen, A.: Cluster activation theory as an explanation of the linear dependence between formation rate of 3 nm particles and sulphuric acid concentration, Atmos. Chem. and Phys., 6, 787–793, 2006.

Leaitch, W. R., Sharma, S., Huang, L., Toom-Sauntry, D., Chivulescu, A., Macdonald, A. M., von Salzen, K., Pierce, J. R., Bertram, A. K., Schroder, J. C., Shantz, N. C., Chang, R. Y.-W., and Norman, A.-L.: Dimethyl sulfide control of the clean summertime Arctic aerosol and cloud, Elementa: Science of the Anthropocene, 1, 000 017, doi:10.12952/journal.elementa.000017, 2013.

Lee, L. a., Pringle, K. J., Reddington, C. L., Mann, G. W., Stier, P., Spracklen, D. V., Pierce, J. R., and Carslaw, K. S.: The magnitude and causes of uncertainty in global model simulations of cloud condensation nuclei, Atmospheric Chemistry and Physics, 13, 8879–8914, doi:10.5194/acp-13-8879-2013, 2013.

Lee, Y. H. and Adams, P. J.: A Fast and Efficient Version of the TwO-Moment Aerosol Sectional (TOMAS) Global Aerosol Microphysics Model, Aerosol Science and Technology, 46, 678–689, doi:10.1080/02786826.2011.643259, 2012.

Lelieveld, J., Butler, T. M., Crowley, J. N., Dillon, T. J., Fischer, H., Ganzeveld, L., Harder, H., Lawrence, M. G., Martinez, M., Taraborrelli, D., and Williams, J.: Atmospheric oxidation capacity sustained by a tropical forest., Nature, 452, 737–40, doi:10.1038/nature06870, 2008.

Levin, E., Kreidenweis, S., McMeeking, G., Carrico, C., Collett Jr., J., and Malm, W.: Aerosol physical, chemical and optical properties during the Rocky Mountain Airborne Nitrogen and Sulfur study, Atmospheric Environment, 43, 1932–1939, doi:10.1016/j.atmosenv.2008.12.042, 2009.

Levin, E. J. T., Prenni, a. J., Petters, M. D., Kreidenweis, S. M., Sullivan, R. C., Atwood, S. a., Ortega, J., DeMott, P. J., and Smith, J. N.: An annual cycle of size-resolved aerosol hygroscopicity at a forested site in Colorado, Journal of Geophysical Research, 117, D06 201, doi:10.1029/2011JD016854, 2012.

Li, G., Lei, W., Zavala, M., Volkamer, R., Dusanter, S., Stevens, P., and Molina, L. T.: Impacts of HONO sources on the photochemistry in Mexico City during the MCMA-2006/MILAGO Campaign, Atmospheric Chemistry and Physics, 10, 6551–6567, doi:10.5194/acp-10-6551-2010, 2010.

Lonsdale, C. R., Stevens, R. G., Brock, C. A., Makar, P. A., Knipping, E. M., and Pierce, J. R.: The effect of coal-fired power-plant SO2 and NOx control technologies on aerosol nucleation in the source plumes, Atmospheric Chemistry and Physics, 12, 11 519–11 531, doi:10.5194/acp-12-11519-2012, 2012.

Luo, G. and Yu, F.: Sensitivity of global cloud condensation nuclei concentrations to primary sulfate emission parameterizations, Atmospheric Chemistry and Physics, 11, 1949–1959, doi:10.5194/acp-11-1949-2011, 2011.

Makkonen, R., Asmi, A., Korhonen, H., Kokkola, H., Järvenoja, S., Räisänen, P., Lehtinen, K. E. J., Laaksonen, A., Kerminen, V.-M., Järvinen, H., Lohmann, U., Bennartz, R., Feichter, J., and Kulmala, M.: Sensitivity of aerosol concentrations and cloud properties to nucleation and secondary organic distribution in ECHAM5-HAM global circulation model, Atmospheric Chemistry and Physics, 9, 1747–1766, doi:10.5194/acp-9-1747-2009, 2009.

Mauldin, R. L., Berndt, T., Sipilä, M., Paasonen, P., Petäjä, T., Kim, S., Kurtén, T., Stratmann, F., Kerminen, V.-M., and Kulmala, M.: A new atmospherically relevant oxidant of sulphur dioxide., Nature, 488, 193–196, doi:10.1038/nature11278, 2012.

Merikanto, J., Napari, I., Vehkamäki, H., Anttila, T., and Kulmala, M.: New parameterization of sulfuric acid-ammonia-water ternary nucleation rates at tropospheric conditions, Journal of Geophysical Research, 112, D15 207, doi:10.1029/2006JD007977, 2007.

Mesinger, F., DiMego, G., Kalnay, E., Mitchell, K., Shafran, P. C., Ebisuzaki, W., Jović, D., Woollen, J., Rogers, E., Berbery, E. H., Ek, M. B., Fan, Y., Grumbine, R., Higgins, W., Li, H., Lin, Y., Manikin, G., Parrish, D., and Shi, W.: North American Regional Reanalysis, Bulletin of the American Meteorological Society, 87, 343–360, doi:10.1175/BAMS-87-3-343, 2006.

Mueller, S. F. and Imhoff, R. E.: Estimates of particle formation and growth in coal-fired boiler exhaust-I. Observations, Atmospheric Environment, 28, 595–602, doi:10.1016/1352-2310(94)90035-3, 1994.

Napari, I., Noppel, M., Vehkamäki, H., and Kulmala, M.: Parametrization of ternary nucleation rates for H_2SO_4-NH_3-H_2O vapors, Journal of Geophysical Research, 107, 4381, doi:10.1029/2002JD002132, 2002.

Offenberg, J. H., Lewandowski, M., Edney, E. O., Kleindienst, T. E., and Jaoui, M.: Influence of aerosol acidity on the formation of secondary organic aerosol from biogenic precursor hydrocarbons., Environmental Science & Technology, 43, 7742–7, doi:10.1021/es901538e, 2009.

Olaguer, E. P., Rappenglück, B., Lefer, B., Stutz, J., Dibb, J., Griffin, R., Brune, W. H., Shauck, M., Buhr, M., Jeffries, H., Wiuete, W., and Pinto, J. P.: Deciphering the Role of Radical Precursors during the Second Texas Air Quality Study, Journal of the Air & Waste Management Association, 59, 1258–1277, doi:10.3155/1047-3289.59.11.1258, 2009.

Olivier, J. G. J., Bouwman, A. F., Van der Maas, C. W. M., Berdowski, J. J. M., Veldt, C., Bloos, J. P. J., Visschedijk, A. J. H., Zandveld, P. Y. J., and Haverlag, J. L.: RIVM report nr. 771060002 / TNO-MEP report nr. R96/119: Description of EDGAR Version 2.0: A set of global emission inventories of greenhouse gases and ozone-depleting substances for all anthropogenic and most natural sources on a per country basis and on 1°x1°grid., Tech. rep., Netherlands Organization for Applied Scientific Research (TNO), 1996.

Olson, J. R., Crawford, J. H., Chen, G., Brune, W. H., Faloona, I. C., Tan, D., Harder, H., and Martinez, M.: A reevaluation of airborne HO_x observations from NASA field campaigns, Journal of Geophysical Research, 111, D10 301, doi:10.1029/2005JD006617, 2006.

Parrish, D. D., Allen, D. T., Bates, T. S., Estes, M., Fehsenfeld, F. C., Feingold, G., Ferrare, R., Hardesty, R. M., Meagher, J. F., Nielsen-Gammon, J. W., Pierce, R. B., Ryerson, T. B., Seinfeld, J. H., and Williams, E. J.: Overview of the Second Texas Air Quality Study (TexAQS II) and the Gulf of Mexico Atmospheric Composition and Climate Study (GoMACCS), Journal of Geophysical Research, 114, D00F13, doi:10.1029/2009JD011842, 2009.

Peng, R. D., Dominici, F., Pastor-Barriuso, R., Zeger, S. L., and Samet, J. M.: Seasonal analyses of air pollution and mortality in 100 US cities., American journal of epidemiology, 161, 585–94, doi:10.1093/aje/kwi075, 2005.

Peters, A., Wichmann, H. E., Tuch, T., Heinrich, J., and Heyder, J.: Respiratory effects are associated with the number of ultrafine particles., American Journal of Respiratory and Critical Care Medicine, 155, 1376–1383, 1997.

Pierce, J. R. and Adams, P. J.: Global evaluation of CCN formation by direct emission of sea salt and growth of ultrafine sea salt, Journal of Geophysical Research, 111, D06 203, doi:10.1029/2005JD006186, 2006.

Pierce, J. R. and Adams, P. J.: Uncertainty in global CCN concentrations from uncertain aerosol nucleation and primary emission rates, Atmospheric Chemistry and Physics, 9, 1339–1356, doi:10.5194/acp-9-1339-2009, 2009.

Pierce, J. R., Chen, K., and Adams, P. J.: Contribution of primary carbonaceous aerosol to cloud condensation nuclei: processes and uncertainties evaluated with a global aerosol microphysics model, Atmospheric Chemistry and Physics, 7, 5447–5466, doi:10.5194/acp-7-5447-2007, 2007.

Pierce, J. R., Riipinen, I., Kulmala, M., Ehn, M., Petäjä, T., Junninen, H., Worsnop, D. R., and Donahue, N. M.: Quantification of the volatility of secondary organic compounds in ultrafine particles during nucleation events, Atmospheric Chemistry and Physics, 11, 9019–9036, doi:10.5194/acp-11-9019-2011, 2011.

Pierce, J. R., Leaitch, W. R., Liggio, J., Westervelt, D. M., Wainwright, C. D., Abbatt, J. P. D., Ahlm, L., Al-Basheer, W., Cziczo, D. J., Hayden, K. L., Lee, a. K. Y., Li, S.-M., Russell, L. M., Sjostedt, S. J., Strawbridge, K. B., Travis, M., Vlasenko, A., Wentzell, J. J. B., Wiebe, H. a., Wong, J. P. S., and Macdonald, a. M.: Nucleation and condensational growth to CCN sizes during a sustained pristine biogenic SOA event in a forested mountain valley, Atmospheric Chemistry and Physics, 12, 3147–3163, doi:10.5194/acp-12-3147-2012, 2012.

Pierce, J. R., Evans, M. J., Scott, C. E., D'Andrea, S. D., Farmer, D. K., Swietlicki, E., and Spracklen, D. V.: Weak global sensitivity of cloud condensation nuclei and the aerosol indirect effect to Criegee + SO_2 chemistry, Atmospheric Chemistry and Physics, 13, 3163–3176, doi:10.5194/acp-13-3163-2013, 2013.

Ångström, A.: On the Atmospheric Transmission of Sun Radiation and on Dust in the Air, Geografiska Annaler, 11, 156–166, 1929.

Reddington, C. L., Carslaw, K. S., Spracklen, D. V., Frontoso, M. G., Collins, L., Merikanto, J., Minikin, A., Hamburger, T., Coe, H., Kulmala, M., Aalto, P., Flentje, H., Plass-Dülmer, C., Birmili, W., Wiedensohler, A., Wehner, B., Tuch, T., Sonntag, A., O'Dowd, C. D., Jennings, S. G., Dupuy, R., Baltensperger, U., Weingartner, E., Hansson, H.-C., Tunved, P., Laj, P., Sellegri, K., Boulon, J., Putaud, J.-P., Gruening, C., Swietlicki, E., Roldin, P., Henzing, J. S., Moerman, M., Mihalopoulos, N., Kouvarakis, G., Ždímal, V., Zíková, N., Marinoni, A., Bonasoni, P., and Duchi, R.: Primary versus secondary contributions to particle number concentrations in the European boundary layer, Atmospheric Chemistry and Physics, 11, 12 007–12 036, doi:10.5194/acp-11-12007-2011, 2011.

Rienecker, M.: File Specification for GEOS-5 DAS Gridded Output, Tech. rep., Global Modeling and Assimilation Office, Goddard Space Flight Center, Greenbelt, Maryland, 2006.

Riipinen, I., Pierce, J. R., Yli-Juuti, T., Nieminen, T., Häkkinen, S., Ehn, M., Junninen, H., Lehtipalo, K., Petäjä, T., Slowik, J., Chang, R., Shantz, N. C., Abbatt, J., Leaitch, W. R., Kerminen, V.-M., Worsnop, D. R., Pandis, S. N., Donahue, N. M., and Kulmala, M.: Organic condensation: a vital link connecting aerosol formation to cloud condensation nuclei (CCN) concentrations, Atmospheric Chemistry and Physics, 11, 3865–3878, doi:10.5194/acp-11-3865-2011, 2011.

Seinfeld, J. H. and Pandis, S. N.: Atmospheric Chemistry and Physics: From Air Pollution to Climate Change, John Wiley and Sons, Inc., Hoboken, New Jersey, 2 edn., 2006.

Sihto, S., Kulmala, M., Kerminen, V.-M., Dal Maso, M., Petäjä, T., Riipinen, I., Korhonen, H., Arnold, F., Janson, R., Boy, M., Laaksonen, A., and Lehtinen, K.: Atmospheric sulphuric acid and aerosol formation: implications from atmospheric measurements for nucleation and early growth mechanisms, Atmospheric Chemistry and Physics, 6, 4079–4091, 2006.

Singh, H. B., Brune, W. H., Crawford, J. H., Jacob, D. J., and Russell, P. B.: Overview of the summer 2004 Intercontinental Chemical Transport Experiment-North America (INTEX-A), Journal of Geophysical Research, 111, D24S01, doi: 10.1029/2006JD007905, 2006.

Sipilä, M., Berndt, T., Petäjä, T., Brus, D., Vanhanen, J., Stratmann, F., Patokoski, J., Mauldin, R. L., Hyvärinen, A.-P., Lihavainen, H., and Kulmala, M.: The role of sulfuric acid in atmospheric nucleation., Science (New York, N.Y.), 327, 1243–6, doi:10.1126/science.1180315, 2010.

Snow-Kropla, E. J., Pierce, J. R., Westervelt, D. M., and Trivitayanurak, W.: Cosmic rays, aerosol formation and cloud-condensation nuclei: sensitivities to model uncertainties, Atmospheric Chemistry and Physics, 11, 4001–4013, doi: 10.5194/acp-11-4001-2011, 2011.

Spracklen, D. V., Pringle, K. J., Carslaw, K. S., Chipperfield, M. P., and Mann, G. W.: A global off-line model of size-resolved aerosol microphysics: II. Identification of key uncertainties, Atmospheric Chemistry and Physics Discussions, 5, 3437–3489, doi:10.5194/acpd-5-3437-2005, 2005.

Spracklen, D. V., Carslaw, K. S., Kulmala, M., Kerminen, V.-M., Sihto, S.-L., Riipinen, I., Merikanto, J., Mann, G. W., Chipperfield, M. P., Wiedensohler, A., Birmili, W., and Lihavainen, H.: Contribution of particle formation to global cloud condensation nuclei concentrations, Geophysical Research Letters, 35, 1–5, doi: 10.1029/2007GL033038, 2008.

Spracklen, D. V., Jimenez, J. L., Carslaw, K. S., Worsnop, D. R., Evans, M. J., Mann, G. W., Zhang, Q., Canagaratna, M. R., Allan, J., Coe, H., McFiggans, G., Rap, a., and Forster, P.: Aerosol mass spectrometer constraint on the global secondary organic aerosol budget, Atmospheric Chemistry and Physics, 11, 12 109–12 136, doi:10.5194/acp-11-12109-2011, 2011.

Srivastava, R. K., Miller, C. a., Erickson, C., and Jambhekar, R.: Emissions of sulfur trioxide from coal-fired power plants., Journal of the Air & Waste Management Association (1995), 54, 750–62, 2004.

Stevens, R. G., Pierce, J. R., Brock, C. A., Reed, M. K., Crawford, J. H., Holloway, J. S., Ryerson, T. B., Huey, L. G., and Nowak, J. B.: Nucleation and growth of sulfate aerosol in coal-fired power plant plumes: sensitivity to background aerosol and meteorology, Atmospheric Chemistry and Physics, 12, 189–206, doi:10.5194/acp-12-189-2012, 2012.

Stieb, D. M., Judek, S., and Burnett, R. T.: Meta-analysis of time-series studies of air pollution and mortality: effects of gases and particles and the influence of cause of death, age, and season., Journal of the Air & Waste Management Association (1995), 52, 470–84, 2002.

Stone, D., Evans, M. J., Edwards, P. M., Commane, R., Ingham, T., Rickard, a. R., Brookes, D. M., Hopkins, J., Leigh, R. J., Lewis, a. C., Monks, P. S., Oram, D., Reeves, C. E., Stewart, D., and Heard, D. E.: Isoprene oxidation mechanisms: measurements and modelling of OH and HO_2 over a South-East Asian tropical rainforest during the OP3 field campaign, Atmospheric Chemistry and Physics, 11, 6749–6771, doi:10.5194/acp-11-6749-2011, 2011.

Streets, D. G., Bond, T. C., Carmichael, G. R., Fernandes, S. D., Fu, Q., He, D., Klimont, Z., Nelson, S. M., Tsai, N. Y., Wang, M. Q., Woo, J.-H., and Yarber, K. F.: An inventory of gaseous and primary aerosol emissions in Asia in the year 2000, Journal of Geophysical Research, 108, 8809, doi:10.1029/2002JD003093, 2003.

Surratt, J. D., Lewandowski, M., Offenberg, J. H., Jaoui, M., Kleindienst, T. E., Edney, E. O., and Seinfeld, J. H.: Effect of acidity on secondary organic aerosol formation from isoprene., Environmental Science & Technology, 41, 5363–9, 2007.

Trivitayanurak, W., Adams, P. J., Spracklen, D. V., and Carslaw, K. S.: Tropospheric aerosol microphysics simulation with assimilated meteorology: model description and intermodel comparison, Atmospheric Chemistry and Physics, 8, 3149–3168, doi:10.5194/acp-8-3149-2008, 2008.

Twomey, S.: Pollution and planetary albedo, Atmospheric Environment, 8, 1251–1256, doi:10.1016/0004-6981(74)90004-3, 1974.

United States Environmental Protection Agency: Clean Air Markets: Data and Maps, URL http://ampd.epa.gov/ampd/, 2012.

van der Werf, G. R., Randerson, J. T., Giglio, L., Collatz, G. J., Mu, M., Kasibhatla, P. S., Morton, D. C., DeFries, R. S., Jin, Y., and van Leeuwen, T. T.: Global fire emissions and the contribution of deforestation, savanna, forest, agricultural, and peat fires (19972009), Atmospheric Chemistry and Physics, 10, 11 707–11 735, doi:10.5194/acp-10-11707-2010, 2010.

Vehkamäki, H., Kulmala, M., Napari, I., Lehtinen, K. E. J., Timmreck, C., Noppel, M., and Laaksonen, A.: An improved parameterization for sulfuric acidwater nucleation rates for tropospheric and stratospheric conditions, Journal of Geophysical Research, 107, 4622, doi:10.1029/2002JD002184, 2002.

Volkamer, R., Sheehy, P., Molina, L. T., and Molina, M. J.: Oxidative capacity of the Mexico City atmosphere Part 1: A radical source perspective, Atmospheric Chemistry and Physics, 10, 6969–6991, doi:10.5194/acp-10-6969-2010, 2010.

Walker, J. M., Philip, S., Martin, R. V., and Seinfeld, J. H.: Simulation of nitrate, sulfate, and ammonium aerosols over the United States, Atmospheric Chemistry and Physics, 12, 11 213–11 227, doi:10.5194/acp-12-11213-2012, 2012.

Wang, M. and Penner, J. E.: Aerosol indirect forcing in a global model with particle nucleation, Atmospheric Chemistry and Physics, 9, 239–260, doi:10.5194/acp-9-239-2009, 2009.

Wang, S. C. and Flagan, R. C.: Scanning Electrical Mobility Spectrometer, Aerosol Science and Technology, 13, 230–240, doi:10.1080/02786829008959441, 1990.

Westervelt, D. M., Pierce, J. R., Riipinen, I., Trivitayanurak, W., Hamed, a., Kulmala, M., Laaksonen, a., Decesari, S., and Adams, P. J.: Formation and growth of nucleated particles into cloud condensation nuclei: modelmeasurement comparison, Atmospheric Chemistry and Physics, 13, 7645–7663, doi:10.5194/acp-13-7645-2013, 2013.

Westervelt, D. M., Pierce, J. R., and Adams, P. J.: Analysis of feedbacks between nucleation rate, survival probability and cloud condensation nuclei formation, Atmospheric Chemistry and Physics, 14, 5577–5597, doi:10.5194/acp-14-5577-2014, 2014.

Whitby, K. T.: Physical characteristics of sulfur aerosols, Atmospheric Environment, 12, 135–159, 1978.

Yu, F.: Ion-mediated nucleation in the atmosphere: Key controlling parameters, implications, and look-up table, Journal of Geophysical Research, 115, D03 206, doi:10.1029/2009JD012630, 2010a.

Yu, F.: Diurnal and seasonal variations of ultrafine particle formation in anthropogenic SO2 plumes., Environmental science & technology, 44, 2011–2015, doi:10.1021/es903228a, 2010b.

Yu, F. and Luo, G.: Simulation of particle size distribution with a global aerosol model: contribution of nucleation to aerosol and CCN number concentrations, Atmospheric Chemistry and Physics Discussions, 9, 10 597–10 645, doi:10.5194/acpd-9-10597-2009, 2009.

Zaveri, R. a., Berkowitz, C. M., Brechtel, F. J., Gilles, M. K., Hubbe, J. M., Jayne, J. T., Kleinman, L. I., Laskin, A., Madronich, S., Onasch, T. B., Pekour, M. S., Springston, S. R., Thornton, J. a., Tivanski, A. V., and Worsnop, D. R.: Nighttime chemical evolution of aerosol and trace gases in a power plant plume: Implications for secondary organic nitrate and organosulfate aerosol formation, NO_3 radical chemistry, and N_2O_5 heterogeneous hydrolysis, Journal of Geophysical Research, 115, D12 304, doi:10.1029/2009JD013250, 2010.

Zhou, W., Cohan, D. S., Pinder, R. W., Neuman, J. a., Holloway, J. S., Peischl, J., Ryerson, T. B., Nowak, J. B., Flocke, F., and Zheng, W. G.: Observation and modeling of the evolution of Texas power plant plumes, Atmospheric Chemistry and Physics, 12, 455–468, doi:10.5194/acp-12-455-2012, 2012.